MECHANIK

FORSCHUNGSBERICHT

Ultrasonic Generators for Energy Harvesting Applications: Self-Excitation and Mechanical Frequency Transformation

Eduard Heffel

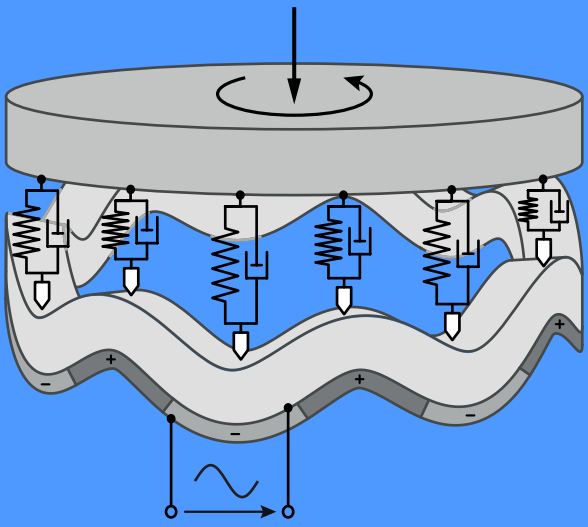

$$\Omega_S \approx \omega_0 \neq f(\Omega_R)$$

TECHNISCHE UNIVERSITÄT DARMSTADT

Band 32

Ultrasonic Generators for Energy Harvesting Applications: Self-Excitation and Mechanical Frequency Transformation

Vom Fachbereich Maschinenbau
an der Technischen Universität Darmstadt
zur
Erlangung des Grades eines Doktor-Ingenieurs (Dr.-Ing.)
genehmigte

Dissertation

vorgelegt von

Eduard Heffel, M.Sc.

aus Kamyschin

Berichterstatter:	Prof. Dr. Peter Hagedorn
Mitberichterstatter:	Prof. Dr.-Ing. Bernhard Schweizer
Tag der Einreichung:	05. November 2013
Tag der mündlichen Prüfung:	20. Dezember 2013

Darmstadt 2013

D 17

Heffel, Eduard

Ultrasonic Generators for Energy Harvesting Applications: Self-Excitation and Mechanical Frequency Transformation

Forschungsberichte des Instituts für Mechanik der Technischen Universität Darmstadt
Band 32

Herausgeber:

Studienbereich Mechanik
Technische Universität Darmstadt
Hochschulstr. 1
D-64289 Darmstadt
Germany

ISBN 978-3-935868-32-7

Für meine geliebte Frau Tea

ეძღვნება ჩემს საყვარელ მეუღლეს თეას

Vorwort

Die vorliegende Arbeit beschäftigt sich mit einem neuartigen Generatorkonzept zur Energierückgewinnung aus mechanischen Schwingungen und entstand während meiner mehrjährigen Tätigkeit als wissenschaftlicher Mitarbeiter in der Arbeitsgruppe Dynamik und Schwingungen an der Technischen Universität Darmstadt, die von Herrn Prof. Peter Hagedorn geleitet wird. Die Arbeitsgruppe war vom Beginn meiner Promotion an bis Juli 2012 an das Fachgebiet Systemzuverlässigkeit und Maschinenakustik von Herrn Prof. Holger Hanselka angegliedert und seitdem beim Fachgebiet Numerische Berechnungsverfahren im Maschinenbau von Herrn Prof. Michael Schäfer.

An dieser Stelle bedanke ich mich ganz herzlich bei allen, die zum Gelingen dieser Arbeit beigetragen haben. Dies gilt im besonderen Maße für meinen Doktorvater Herrn Prof. Peter Hagedorn, der mich bereits seit dem ersten Semester für die Mechanik begeistern konnte. Durch seine stete Förderung und wissenschaftliche Betreuung konnte ich mich sehr stark weiterentwickeln. Er ließ mir dabei immer genug Freiheiten, um mich in neue Themengebiete einzuarbeiten und eigene Ideen umzusetzen. Mein Dank gilt auch Herrn Prof. Bernhard Schweizer für die bereitwillige Übernahme des Koreferats, die detaillierten Gespräche und die entgegengebrachte Begeisterung für mein Forschungsthema.

Einen bedeutenden Anteil am Gelingen dieser Arbeit hat mein ehemaliger Kollege Gottfried Spelsberg-Korspeter, dem ich für seine zahlreichen fachlichen Anregungen und seine unermüdliche Diskussionsbereitschaft sehr dankbar bin. Mit ihm zusammen sind einige wichtige theoretische Grundlagen für die vorliegende Arbeit entstanden. Auch bin ich ihm für die Unterstützung bei der Durchführung der Experimente sehr dankbar.

Ich möchte mich bei meinen derzeitigen und ehemaligen Kollegen Andreas Wagner, Manuel Eckstein, Henning Spiegelberg, Matthias Heymanns, Steffen

Wiendl und Andres Arrieta-Diaz für die sehr gute Zusammenarbeit und die überaus angenehme Zeit in der Arbeitsgruppe bedanken. Auch gilt mein Dank Maria Rauck und Renate Schreiber für ihre große Hilfsbereitschaft.

Zum Gelingen dieser Arbeit haben auch Marcel Mahner, Matthias Lalk, Thomas Breunung und Alexander Brune beigetragen, die ich im Rahmen einer Abschlußarbeit bzw. einer Tätigkeit als Hilfswissenschaftler betreut habe.

Ich möchte mich zuletzt bei meinen Eltern für ihre Unterstützung bedanken und auch insbesondere bei meiner Frau Tea, die mir die notwendige Kraft und einen starken Rückhalt während der gesamten Zeit gegeben hat.

Darmstadt, im Januar 2014 Eduard Heffel

Abstract

The main objective in the field of vibration-based energy harvesting is to convert the kinetic energy from an ambient energy source into an useable electrical form in the most efficient way. The intention is to provide power for low-powered electronic devices, such as intelligent sensors for structural health monitoring, in order to make an external power source or periodic battery replacement redundant and thus lower the costs. Applications of this technology can be found in the automotive and aerospace industry as well as in civil and mechanical engineering. One of the main challenges in the area of vibration-based energy harvesting is to design an energy harvesting device generating a significant amount of electrical power across varying vibration inputs. Due to the design, most energy harvesters are subject to forced excitation and have therefore the drawback that the performance strongly depends on the uncertain excitation parameters. Furthermore, to achieve a high power density of the piezoceramics used for the energy conversion, it is required to generate a high-frequency operation of the piezoceramics from a low-frequency vibration source. Such frequency transformation is, for example, exploited in ultrasonic motors, but has never been examined in the inverse direction for ultrasonic generators. In this thesis, a new concept of piezoelectric generators is studied in detail with respect to its applicability for energy harvesting systems. To this end, electromechanical models of two different ultrasonic motors are derived in order to study their convertibility of the operating direction. Based on the analytical models, the influence of the main parameters on the dynamic behavior as well as the characteristic steady-state operation are determined. Experiments are carried out to validate this concept.

Zusammenfassung

Die Hauptaufgabe im Bereich des schwingungsbasierten Energy-Harvesting ist die möglichst effiziente Umwandlung von kinetischer Energie aus Schwingungen und Bewegungen einer Struktur in nutzbare elektrische Form. Diese wird beispielweise zur Speisung leistungsarmer Elektronik verwendet, um die Kosten für eine externe Energieversorgung, zusätzliche Verkabelung und Batteriewechsel zu reduzieren. Solche energieautarken Systeme finden Anwendung im Bereich des Structural-Health-Monitoring, im Automobil- oder Flugzeugbau, aber auch im Bauwesen oder im Maschinenbau. Eine Herausforderung im Gebiet des schwingungsbasierten Energy-Harvesting ist es, den Energy-Harvester so auszulegen, dass dieser bei verschieden Eingangssignalen einen annehmbaren Wirkungsgrad aufweist. Da die meisten untersuchten Generatorprinzipien konstruktiv bedingt auf einem zwangserregten System basieren, haben sie den Nachteil, dass die Systemdynamik stark von dem in der Regel unbekannten Anregungssignal abhängt. Des Weiteren ist es für eine hohe Leistungsdichte der zur Energieumwandlung verwendeten Piezokeramiken notwendig, aus einer niederfrequenten Anregung heraus die Piezokeramik möglichst hochfrequent zu betreiben. Zwar wird solch eine Frequenzwandlung bereits bei Ultraschallmotoren ausgenutzt, dennoch sind keine Anwendungen für den Generatorbetrieb bekannt. In dieser Arbeit wird ein neues Konzept von piezoelektrischen Generatoren für die Anwendung im Energy-Harvesting untersucht. Zu diesem Zweck werden elektromechanische Modelle für zwei verschiedene Ultraschallmotoren hergeleitet und auf ihre Umkehrung des Funktionsprinzips hin untersucht. Anhand der analytischen Modelle kann sowohl der Einfluss der wichtigsten Parameter auf die Systemdynamik, als auch die Charakteristiken im Generatorbetrieb abgeschätzt werden. Der Nachweis für die Realisierbarkeit dieses Konzepts wird experimentell erbracht.

Contents

1 Introduction

1.1 Vibration-based energy harvesting

With the increasing complexity of technical structures, more sensors and actuators are used. The increased infrastructure density leads to higher needs in cabling for energy and data transmission and thus increases cost. Therefore, a decentralized power supply for certain devices is required. However, battery-driven devices require high maintenance, which is unwanted in many cases. Energy harvesting promises a way for self-powered devices and the possibility of reducing production costs due to reduced need of cable conduit and due to reduced service costs. In the research field of energy harvesting, one can distinguish between applications for different types of the ambient energy source, which can be radiant, thermal, mechanical, magnetic or biochemical. In general, the harvested energy is converted into the electrical form, in order to power a storage device or the electric load directly.

This thesis deals with special energy harvesting devices using a mechanical energy source, which fall into the field of vibration-based or kinetic energy harvesting. The main task in this field is to power small electronic devices, such as intelligent sensors, by using the kinetic energy from their environment, such as structural vibrations or motions. In general, the dynamical properties of the ambient energy source, such as frequency and amplitude, are not known in detail. Therefore, it is important to achieve a broadband applicability of the energy harvesting device, which means an efficient energy conversion for different amplitudes and frequencies of the excitation signal. In order to face this problem, many techniques are proposed in the literature, for example resonance-tuning, multi-modal or nonlinear techniques [4, 8, 25, 26, 40]. Basically, the derived mathematical models lead to nonhomogeneous differential equations and therefore to the analysis of forced-vibrations. Figure 1.1 shows

the most common topology studied in the vibration-based energy harvesting community, which is a vibrating cantilever beam forced by a vertical motion of the clamping. The piezoelectric layer (P) is deformed through the beam vibrations and leads to electric voltage between the electrodes. Systems with

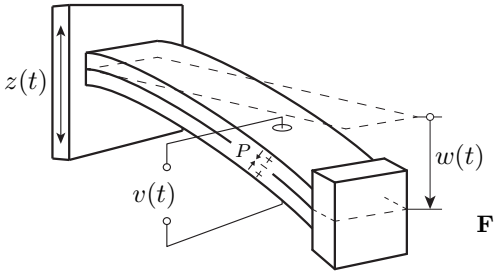

Figure 1.1: Piezoelectric cantilever beam with base excitation.

forced excitation have the disadvantage that the resulting vibrations of the structure strongly depend on the unknown excitation frequency and amplitude. The excitation frequency, which is generally in the range up to 200 Hz, significantly affects the design space of the natural frequency of the energy harvesting system. Since the energy converted per cycle in a piezoelectric element from mechanical to electrical is small, it would be convenient to operate the transducer at high frequency. One possibility to transform a low-frequency excitation to a high-frequency excitation is the use of a frequency up-conversion, described in [10, 39, 55]. In systems with a frequency up-conversion the energy harvesting device is subject to impulses, leading to homogeneous oscillations of the structure in its natural frequency. The disadvantage of such systems is the complexity of the required design realizing the excitation through impulses.

Another possibility to overcome the dependence on the excitation parameters is the use of a self-excitation mechanism. For this type of a system, the excitation does not lead to forced vibrations but, under specific circumstances, to a destabilization of the system's trivial solution, which can result in limit cycle oscillations dominated by the natural frequencies of the structure. An overview on energy harvesting systems using flow-induced self-excitation resulting from fluid-structure interaction is given by Erturk and

Inman in [8]. A further possibility is to use friction-induced self-excited vibrations for energy harvesting applications, which yet were not considered in the literature. The suppression of unwanted friction-induced vibrations is widely studied in the literature, for example for automotive brakes in [20, 27, 60] or for paper calenders in [6, 53, 62]. Friction induced vibrations can however be useful, for example in musical instruments or even in energy harvesting applications.

1.2 Motivation

As the convertible energy in a piezoelectric element is limited by the charge that can be produced during one cycle of operation, it is evident that a high power density requires a high frequency excitation of the piezoelectric element. While this principle is being used in piezoelectric motors and transformers, a literature review does not show an indication that the same principle has been studied systematically for piezoelectric generators. Piezoelectric motors using a high mechanical frequency transformation, namely from high to low frequency, are ultrasonic motors, shown in Fig. 1.2. The working principle of

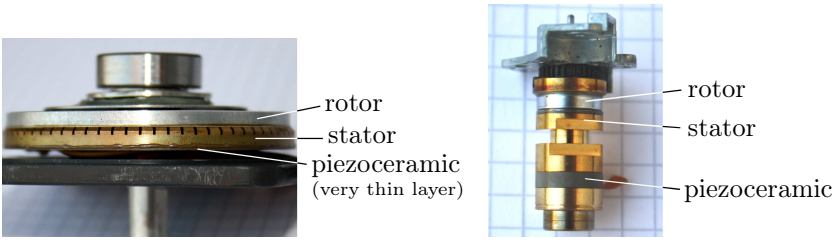

(a) Shinsei plate-type ultrasonic motor USR-60.

(b) Canon bar-type ultrasonic motor U400.

Figure 1.2: Different types of ultrasonic motors.

the different ultrasonic motors is similar. Due to a high-frequency excitation (e.g. in the 100 kHz range) of the piezoceramic structure, a traveling wave on the stator is generated, leading to a low-frequency rotation of the rotor (about $1-20$ Hz) through contact forces. Ultrasonic motors are used for example in

lens drives in autofocus cameras and for applications requiring precision rotations. The commonly available ultrasonic motors can have very different designs and dimensions ($\varnothing\, 1-6\,\mathrm{cm}$). For example, a traveling wave ultrasonic motor using the so-called piezoelectric d_{31}-effect is studied by Sattel in [45] (Fig. 1.2a). An ultrasonic motor, using the piezoelectric d_{33}-effect, is the wobbling disk ultrasonic motor studied by Gutschmidt in [11] (Fig. 1.2b). Another design for an ultrasonic motor, which uses the piezoelectric d_{15}-effect, is studied by Schönecker in [48]. One challenge in the analysis of the resulting friction-induced vibrations is the complex contact mechanism between stator and rotor. For an ultrasonic traveling wave motor the stator-rotor contact was studied in detail in [46, 47].

One of the main goals of this work is to assess the feasibility of inverting the actuation of common ultrasonic motors. Using the ultrasonic motor as a generator implies the convertibility of the operating direction, which has to be studied in detail. While in motor mode the stator motion is directly determined by a specified excitation of the piezoceramic and the applied load, in the generator mode it is not obvious how any stationary motion or which kind of stationary motion can be generated. Since the excitation of the ultrasonic generators is done by the rotor, an appropriate design for the transformation of structural vibrations into an angular motion is required. For an inertially fixed generator different designs can be realized, shown in Fig. 1.3. For a

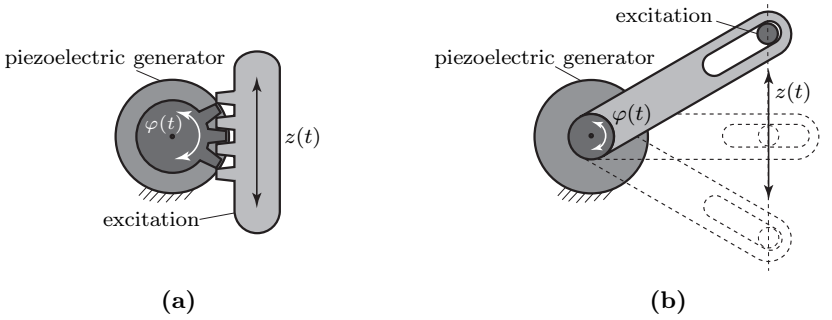

Figure 1.3: Different designs for kinematic transformation of vibrations into angular motion of the rotor.

structure-fixed generator it is necessary to apply a modification of the design, realizing a relative motion between the stator and the rotor. Such relative motion is realized for example in self-winding wrist watches, which are the first real-life application[1] of the concept of energy harvesting, long before this term was coined.

1.3 Outline of the thesis

In this thesis two ultrasonic motors, namely the wobbling disk and the traveling wave ultrasonic motor, shown in Fig. 1.2, are studied with respect to their applicability for energy harvesting systems. This implies two main objectives for the realization of the concept of piezoelectric generators exploiting a high frequency transformation, from low frequency excitation ($<200\,\mathrm{Hz}$) to high frequency energy conversion through the piezoelectric element ($>10\,\mathrm{kHz}$). The first one is the initiation of limit-cycle oscillations, which is to be realized through a self-excitation mechanism based on non-conservative forces resulting from the frictional contact between the rotor and the stator. The second one is the optimization of the stable limit cycle in terms of maximizing the electrical power output at the electric load.

This thesis is organized as follows. Chapter 2 deals with the mechanical and electromechanical energy conversion relevant for energy harvesting applications. Mainly the characteristics of the mechanical energy conversion based on self-excited vibrations are discussed using a minimal model of a non-conservative system exploiting friction-induced vibrations. In chapter 3, a simple electromechanical model for the wobbling disk generator is derived and analyzed with respect to the initiation of self-excited vibrations and to the characteristics of the steady-state operation. Chapter 4 consists of the modeling and the detailed analysis of the traveling wave generator, showing, compared to the wobbling disk generator, many different modes in the generator operation. In chapter 5 different dynamic properties of the ultrasonic generators are considered, such as stability behavior of different types of so-

[1] According to the report from the French Science Academy in 1778, the first self-winding watch was designed by Hubert Sarton from Belgium.

lutions as well as the basins of attraction of stable solutions. To this end, different approaches are discussed. In order to proof the feasibility of the proposed generator concept, experimental investigations were carried out, the results of which are discussed in detail in chapter 6. A summary of the main results and motivation for future work is given in chapter 7.

2 Mechanical and electromechanical energy conversion

This chapter deals with different energy conversion mechanisms, which play a main role in the design and optimization of energy harvesting applications. In the first section, two mechanisms for conversion of mechanical energy into a different type of mechanical energy are compared. The dynamics of most of the energy harvesters studied in the literature is described by forced vibrations. In contrast to that, the ultrasonic generators studied in this thesis are subject to self-excited vibrations. A simple model of a non-conservative systems exploiting self-excitation mechanism is used, in order to highlight the main differences compared to force-excited systems. In the second section, the three known types of conversion of mechanical into electrical energy are discussed, namely capacitive, inductive and piezoelectric energy conversion.

2.1 Mechanical transfer characteristics

Depending on the mechanism transferring energy into a system, different dynamic behavior occurs. Often, the energy transfer can be modeled as forced vibrations of the mechanical structure. But also cases exist, where non-conservative forces lead to circulatory terms in the equations of motion, without any contribution to the right-hand side[1]. The latter one is referred to as a self-excited system. The differences between these two excitation mechanisms are discussed in the following.

[1] The right-hand side of the equations of motion consists of terms independent from state variables of the system.

2.1.1 Forced vibrations

Most of the vibration-based energy harvesting systems proposed in the literature are subject to forced vibrations [4, 8, 25, 38, 40]. The dynamics of the system is described by ordinary differential equations, where the excitation is modeled as an inhomogeneous part at the right-hand side. The main characteristics of these systems is that the system response strongly depends on the excitation frequency and amplitude. In linear system theory, these characteristics can be described by *transfer functions* [29, 30, 56]. In case of a system consisting of linear oscillators, the largest amplitude is expected for the excitation frequency near one of the resonance frequencies. A small deviation from this frequency leads to a significant drop of generated power and therefore to a loss of efficiency. Since the excitation parameters are not known in detail, the mechanical system has to be designed in such a way that the region of large amplitudes is broadened. Therefore, different techniques, such as resonance-tuning, multi-modal or nonlinear techniques, are proposed in the literature [40, 55]. A further aspect on forced excited systems is that the design space of the natural frequency of the mechanical system is restricted by the frequency range of the excitation signal (in general up to 200 Hz [44]). This leads to a drawback for systems using piezoceramic transducers, which require high frequency energy conversion to achieve high power density.

2.1.2 Self-excited vibrations

The ultrasonic generators studied in this thesis are subject to friction-induced self-excited vibrations. For energy harvesting applications the stable equilibrium state of the generators is to be self-excited leading to limit-cycle oscillations. These limit-cycle oscillations lead to a steady energy conversion through the piezocermic. The main characteristics of self-excited vibrations are discussed by using a simple example of a non-conservative system. Compared to forced vibrations, where the system responds directly to the applied forcing terms, for self-excited systems the response depends on the stability of the trivial solution. If the trivial solution is unstable, self-excited vibrations can occur. Otherwise, the system remains in the stable equilibrium state.

Consequently, the analysis of self-excited vibrations is divided into two parts. First, the influence of the system parameters on the initiation of self-excited vibrations is analyzed. Afterwards, the characteristics of the resulting limit-cycle oscillations are determined.

Initiation of self-excitation

The main aspects of self-excited vibrations are highlighted using a simple academic example of a non-conservative circulatory mechanical system. The minimal model consists of a point mass, which is in contact with a frictional belt, analyzed by BROMMUNDT in [5] and by HOFFMANN et al. in [21]. The simplified mechanical model is shown in Fig. 2.1a. The point mass is pressed against a moving belt, which is assumed to be massless and is moving with the positive velocity $v > 0$. The frictional contact between the point mass and the belt is modeled by using COULOMB's law of friction (friction coefficient μ). The free-body diagram for the point mass is shown in Fig. 2.1b.

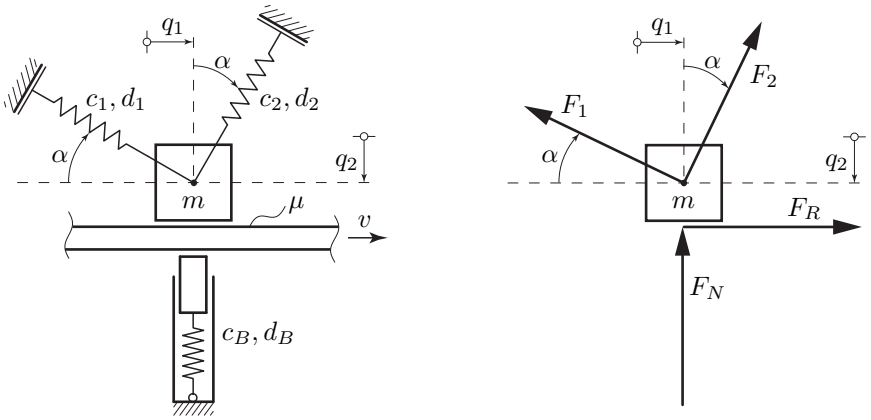

(a) Simplified mechanical model. **(b)** Free-body diagram.

Figure 2.1: Point mass in contact with a frictional belt (dampers are not shown explicitly).

Applying NEWTON's law yields

$$m\,\ddot{q}_1 = F_R - F_1\cos\alpha + F_2\sin\alpha, \quad m\,\ddot{q}_2 = -F_N - F_1\sin\alpha - F_2\cos\alpha. \tag{2.1}$$

The forces F_1 and F_2 consist of nonlinear restoring and linear damping terms

$$F_1 = c_1(\Delta s_1 + \eta\Delta s_1^3) + d_1\Delta\dot{s}_1, \quad F_2 = c_2(\Delta s_2 + \eta\Delta s_2^3) + d_2\,\Delta\dot{s}_2\,, \tag{2.2}$$

where c_i and d_i are the stiffness and damping coefficients. The coefficient of the cubic restoring term is given by η. The displacements Δs_i can be expressed as functions of the generalized coordinates q_i,

$$\Delta s_1 = -q_1\,\sin\alpha + q_2\,\cos\alpha, \qquad \Delta s_2 = q_1\,\cos\alpha + q_2\,\sin\alpha\,. \tag{2.3}$$

The normal force F_N is

$$F_N = c_B\,q_2 + d_B\,\dot{q}_2\,, \tag{2.4}$$

where c_B and d_B are the stiffness and damping coefficient of the bedding. According to COULOMB's law of friction the friction force F_R is

$$F_R = -\mu\,|F_N|\,\operatorname{sign} v_{\mathrm{rel}}\,. \tag{2.5}$$

Assuming that the normal force F_N is always positive, this means that the point mass is always in contact with the belt, and that the relative velocity $v_{\mathrm{rel}} = \dot{q}_1 - v < 0$, the expression for the friction force F_R simplifies to

$$F_R = \mu\,(c_B\,q_2 + d_B\,\dot{q}_2)\,. \tag{2.6}$$

The static displacement of the point mass resulting from the constant part of the normal and the friction force is not of interest, and therefore is not discussed at this point. Inserting the expressions for the forces (2.2) - (2.6) into the equations of motion (2.1) leads to

$$\mathbf{M}\,\ddot{\mathbf{q}} + \mathbf{B}\,\dot{\mathbf{q}} + \mathbf{C}\,\mathbf{q} = \mathbf{f}\,, \qquad \text{with} \qquad \mathbf{q} = [q_1, q_2]^{\mathrm{T}}\,. \tag{2.7}$$

The matrices $\mathbf{M}, \mathbf{B}, \mathbf{C}$ are given by

$$\begin{aligned} \mathbf{M} &= \begin{bmatrix} m & 0 \\ 0 & m \end{bmatrix}, \quad \mathbf{B} = \begin{bmatrix} d + \Delta d\cos 2\alpha & \Delta d\sin 2\alpha - \mu d_B \\ \Delta d\sin 2\alpha & d - \Delta d\cos 2\alpha + d_B \end{bmatrix}, \\ \mathbf{C} &= \begin{bmatrix} c + \Delta c\cos 2\alpha & \Delta c\sin 2\alpha - \mu c_B \\ \Delta c\sin 2\alpha & c - \Delta c\cos 2\alpha + c_B \end{bmatrix}, \end{aligned} \tag{2.8}$$

where the used abbreviations are

$$d=\frac{d_1+d_2}{2}\,,\quad \Delta d=\frac{d_1-d_2}{2}\,,\quad c=\frac{c_1+c_2}{2}\,,\quad \Delta c=\frac{c_1-c_2}{2}\,. \tag{2.9}$$

The vector on the right-hand side ($\mathbf{f}$) consists of the nonlinear terms

$$\mathbf{f}=\eta\begin{bmatrix}-c_1\Delta s_1^3\cos\alpha+c_2\Delta s_2^3\sin\alpha\\ -c_1\Delta s_1^3\sin\alpha-c_2\Delta s_2^3\cos\alpha\end{bmatrix}. \tag{2.10}$$

By setting $\eta=0$ the equations of motion (2.7) become linear. In order to get a better insight into the dynamical properties of the system, it is useful to split up the velocity and displacement-proportional matrices $\mathbf{B}$ and $\mathbf{C}$ into their symmetric and skew-symmetric parts. For an arbitrary matrix $\mathbf{A}$ the symmetric and skew-symmetric parts $\mathbf{A}_{\mathrm{sym}}$ and $\mathbf{A}_{\mathrm{skew}}$ can be calculated by

$$\mathbf{A}_{\mathrm{sym}}=\frac{1}{2}\left(\mathbf{A}+\mathbf{A}^{\mathrm{T}}\right)\,,\qquad \mathbf{A}_{\mathrm{skew}}=\frac{1}{2}\left(\mathbf{A}-\mathbf{A}^{\mathrm{T}}\right)\,. \tag{2.11}$$

Thereby, the equations of motion (2.7) are rewritten as

$$\mathbf{M}\,\ddot{\mathbf{q}}+(\mathbf{D}+\mathbf{G})\,\dot{\mathbf{q}}+(\mathbf{K}+\mathbf{N})\,\mathbf{q}=\mathbf{f}\,, \tag{2.12}$$

where

$$\mathbf{M}=\mathbf{M}^{\mathrm{T}}\,,\quad \mathbf{D}=\mathbf{D}^{\mathrm{T}}\,,\quad \mathbf{G}=-\mathbf{G}^{\mathrm{T}}\,,\quad \mathbf{K}=\mathbf{K}^{\mathrm{T}}\,,\quad \mathbf{N}=-\mathbf{N}^{\mathrm{T}}\,. \tag{2.13}$$

The symmetric matrices $\mathbf{M},\mathbf{D}$ and $\mathbf{K}$ are the mass, damping and stiffness matrix of the system. The skew-symmetric matrices $\mathbf{G}$ and $\mathbf{N}$ are the gyroscopic and the circulatory matrix of the system. Splitting up the velocity and displacement-proportional matrices $\mathbf{B}$ and $\mathbf{C}$ in Eq. (2.8) into their symmetric and skew-symmetric parts leads to

$$\begin{aligned}\mathbf{D}&=\begin{bmatrix}d+\Delta d\cos 2\alpha & \Delta d\sin 2\alpha-\frac{1}{2}\mu d_B\\ \Delta d\sin 2\alpha-\frac{1}{2}\mu d_B & d-\Delta d\cos 2\alpha+d_B\end{bmatrix},\ \mathbf{G}=\begin{bmatrix}0 & -\frac{1}{2}\mu d_B\\ \frac{1}{2}\mu d_B & 0\end{bmatrix},\\ \mathbf{K}&=\begin{bmatrix}c+\Delta c\cos 2\alpha & \Delta c\sin 2\alpha-\frac{1}{2}\mu c_B\\ \Delta c\sin 2\alpha-\frac{1}{2}\mu c_B & c-\Delta c\cos 2\alpha+c_B\end{bmatrix},\ \mathbf{N}=\begin{bmatrix}0 & -\frac{1}{2}\mu c_B\\ \frac{1}{2}\mu c_B & 0\end{bmatrix}.\end{aligned} \tag{2.14}$$

From this point of view, one can clearly see that in this system the gyroscopic and circulatory effect only occur due to the frictional contact ($\mu>0$). For

this system two types of instability phenomena may occur, namely divergence and the flutter-type instability. The latter one leads to self-excited oscillations, which are desired from the point of view of energy harvesting. The stability of the trivial solution of Eq. (2.12) is analyzed based on the linearized equations of motion, which are obtained by setting $\eta = 0$ or $\mathbf{f} = \mathbf{0}$, respectively. The stability boundary can be calculated in many different ways, for example with the ROUTH scheme, see [32, 37]. Assuming, due to simplicity, that $d_1 = d_2$ and $d_B = 0$ leads to the following damping and gyroscopic matrix

$$\mathbf{D} = \begin{bmatrix} d & 0 \\ 0 & d \end{bmatrix}, \quad \mathbf{G} = \mathbf{0}. \tag{2.15}$$

Therefore the expressions for the stability boundary can be written in a simpler form. The divergence instability occurs if

$$k_{11}k_{22} + n_{12}^2 - k_{12}^2 < 0, \tag{2.16}$$

and the flutter instability if

$$d^2\frac{k}{m} + \Delta k^2 + k_{12}^2 - n_{12}^2 < 0\,, \quad k = \frac{k_{11}+k_{22}}{2}\,,\ \Delta k = \frac{k_{11}-k_{22}}{2}\,. \tag{2.17}$$

The elements of the stiffness matrix $\mathbf{K}$ and of the circulatory matrix $\mathbf{N}$ are k_{ij} and n_{ij}. Figure 2.2 shows the stability map of the system (2.7) for the

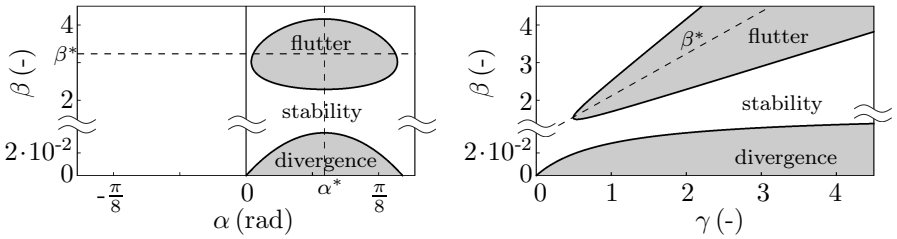

(a) Stability boundaries in the β-α-plane ($\gamma = 2$).

(b) Stability boundaries in the β-γ-plane ($\alpha = \alpha^* = 0.23\,\text{rad}$).

Figure 2.2: Stability map of the point mass in frictional contact (optimal parameters: α^*, β^*).

Table 2.1: Parameters of the minimal model for self-excitation.

$m = 1\,\mathrm{kg}$	$c_2 = 1\,\mathrm{N/m}$	$c_1 = \beta\, c_2$	$c_B = \gamma\, c_2$	$d = 0.1\,\mathrm{Ns/m}$	$\mu = 0.5$

parameter set given in Tab. 2.1. The region of the flutter-type instability appears in a certain region of β and γ, respectively. The divergence instability occurs only for relatively small β, which is equivalent to a large difference between the stiffness coefficients ($c_1 \ll c_2$). For energy harvesting applications exploiting self-excitation mechanism, the trivial solution needs to be destabilized in the sense of a flutter-type instability. In comparison to the divergence instability, the flutter-type instability requires a systems with at least two degrees of freedom. The difference between these two instability phenomena

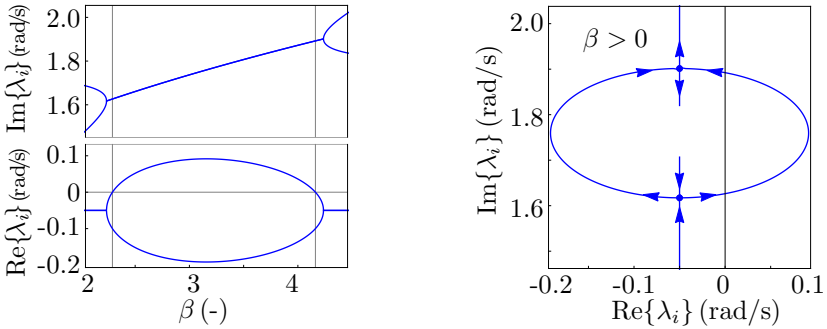

(a) Imaginary and real part of λ_i.

(b) Root locus of λ_i.

Figure 2.3: Bifurcation of the eigenvalues λ_i over β (flutter-type instability of a circulatory system with damping).

can be highlighted by analyzing the bifurcation behavior of the eigenvalues of the linearized system, shown in Fig. 2.3 and 2.4. Since the considered system is damped ($d > 0$), the bifurcation point does not correspond to the stability boundary of the system. In case of flutter-type instability, two eigenvalue

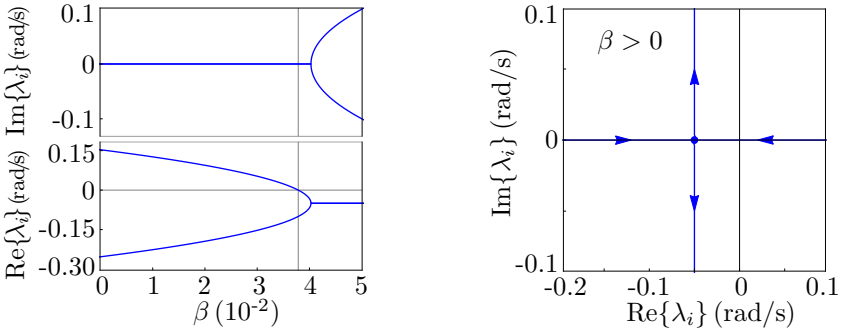

(a) Imaginary and real part of λ_i.

(b) Root locus of λ_i.

Figure 2.4: Bifurcation of the eigenvalues λ_i over β (divergence instability of a damped system).

pairs coalesce and one eigenvalue pair cross the imaginary axis (Fig. 2.3b). In general, a flutter-type instability or self-excitation occurs when at least one eigenvalue pair cross the imaginary axis with a non-zero imaginary part. In case of the divergency instability, one eigenvalue crosses the imaginary axis with a zero imaginary part, see Fig. 2.4b. This indicates that one equilibrium state becomes unstable. The system, in general, moves to a different stable equilibrium and does not go into a limit cycle. For energy harvesting systems exploiting self-excitation mechanism, the trivial solution is to be destabilized in the sense of a flutter-type instability.

One objective in the design of an energy harvesting system is to optimize the system parameters in such a way that the desired instability region is maximized. Since in real-life the system is subject to uncertainties, for example in the model or in the system and excitation parameters, a relatively small instability region can be practically non-existent. Therefore, an optimization of the system regarding the maximization of the instability region is required, in order to achieve a more robust configuration. This optimization is a very important step in the design process since on the one hand, different kinds of perturbations can occur, and on the other hand, the mechanical model

and the system parameters are subject to uncertainties. A robust design is obtained by minimizing the absolute difference between the imaginary parts of the two critical eigenvalue pairs,

$$\min \Delta \mathrm{Im}\{\lambda_i\} = \min |\omega_1 - \omega_2|. \tag{2.18}$$

It may be more convenient to consider

$$\min \Delta \mathrm{Im}^2\{\lambda_i\} = \min |\omega_1^2 - \omega_2^2|. \tag{2.19}$$

Using the special structure for the damping and gyroscopic matrix (2.15), the eigenvalues of the linearized system (2.12) simplify to

$$\lambda_{1,2,3,4} = -\frac{d}{2m} \pm \sqrt{\frac{1}{m}\left(\frac{d^2}{4m} - k \pm \sqrt{k_{12}^2 + \Delta k^2 - n_{12}^2}\right)}, \tag{2.20}$$

where k and Δk are the abbreviations used in Eq. (2.17) and the k_{ij} and n_{ij} are the elements of the stiffness and circulatory matrix $\mathbf{K}$ and $\mathbf{N}$. Generally, the eigenvalues λ_i appear in complex conjugate form

$$\begin{aligned} \lambda_{1,2} &= -\delta_1 \pm \mathrm{i}\,\omega_1\,, \\ \lambda_{3,4} &= -\delta_2 \pm \mathrm{i}\,\omega_2\,, \end{aligned} \tag{2.21}$$

where the real and imaginary parts δ_i and ω_i can be calculated from Eq. (2.20). One can distinguish between the following two cases, where the imaginary parts can be equal or not,

$$\omega_{1,2}^2 = \begin{cases} a_\omega \pm b_\omega & , \text{for } b_\omega^2 > 0\,, \\ \frac{1}{2}\left(a_\omega + \sqrt{a_\omega^2 - b_\omega^2}\right) & , \text{for } b_\omega^2 < 0\,, \end{cases} \tag{2.22}$$

$$a_\omega = \frac{k}{m} - \frac{d^2}{4m^2}, \qquad b_\omega^2 = \frac{k_{12}^2 + \Delta k^2 - n_{12}^2}{2m^2}\,. \tag{2.23}$$

The optimization problem (2.19) is only non-trivial if the expressions for the separated imaginary parts is used ($\omega_1 \neq \omega_2$). Inserting the expressions for the imaginary parts for $b_\omega^2 > 0$ into the optimization problem (2.19) yields

$$\min |\omega_1^2 - \omega_2^2| = \min |2\sqrt{k_{12}^2 + \Delta k^2 - n_{12}^2}| \sim \min |k_{12}^2 + \Delta k^2 - n_{12}^2|. \tag{2.24}$$

Thus, for the cost function J of the optimization problem follows

$$\begin{aligned} \min J &= \min |k_{12}^2 + \Delta k^2 - n_{12}^2| \\ &= \min |\frac{c_2^2}{4} \left[\gamma^2 + (\beta-1)^2 - 2\,\gamma\,(\beta-1)(\cos 2\alpha - \mu \sin 2\alpha)\right]|, \end{aligned} \tag{2.25}$$

where the parameters from Tab. 2.1 are used. Assuming that the parameters c_2, γ and μ are fixed, leads to an optimization problem in the variables α and β. The optimal values can be calculated by extreme value analysis of J. Thereby, the optimal values α^* and β^* minimizing J are

$$\begin{aligned} \alpha^* &= \frac{\arctan \mu}{2}\,, \\ \beta^* &= 1 + \gamma\,\sqrt{1+\mu^2}\,. \end{aligned} \tag{2.26}$$

These optimal values are plotted in the stability map, shown in Fig. 2.2. Obviously, the optimal parameters lead to a robust system design with respect to occurrence of flutter-type instability. The goal of the optimization can be formulated as designing a more symmetric configuration. This stands in contrast to the suppression of self-excited oscillations, where the optimization problem aims on creating a more asymmetric configuration by separating the eigenfrequencies[2] [50, 61].

Steady-state characteristics

The destabilization of the trivial solution, in the sense of a flutter-type instability, leads to limit-cycle oscillations. The nonlinearity in the minimal model, shown in Fig. 2.1a, originate from cubic restoring terms defined in Eq. (2.2). The resulting steady-state characteristics for $\eta = 1$ shows different kind of bifurcations, see Fig. 2.5a. The corresponding orbit of the point mass is displayed in Fig. 2.6. The limit-cycle frequency appears to be slightly higher than the natural frequency of the linearized system, see Fig. 2.5b. The fact that the limit-cycle frequency almost corresponds to the natural frequency of the linearized systems is typical for systems with self-excitation mechanism, here.

[2]The eigenfrequency is also referred to as natural frequency or imaginary part of the eigenvalue.

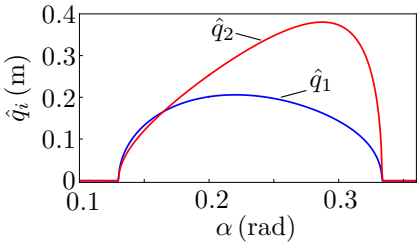

(a) Bifurcation diagram of the limit-cycle amplitude $\hat{q}_i$ for $\beta = 4$ and $\gamma = 2$.

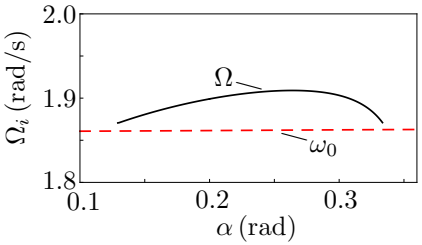

(b) Limit-cycle frequency Ω compared to the eigenfrequency $\omega_0 = |\mathrm{Im}\{\lambda_i\}|$.

Figure 2.5: Characteristics of the limit-cycle oscillations.

Compared to systems with forced vibrations, the steady-state characteristics are almost independent of excitation parameters. Moreover, the oscillation frequency can be adjusted freely by designing the natural frequency of the mechanical system.

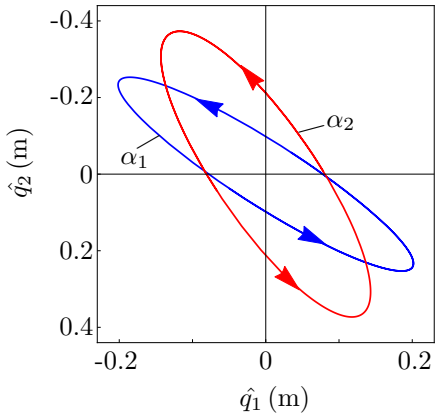

Figure 2.6: Limit-cycle orbit of the point mass in the q_1-q_2-plane for $\alpha = \alpha_i$, ($\alpha_1 = 0.2$ rad, $\alpha_2 = 0.3$ rad).

2.2 Electromechanical energy conversion

In the field of vibration-based energy harvesting, the three main mechanisms for the conversion of mechanical into electrical energy are the capacitive (electrostatic), inductive (electromagnetic) and the piezoelectric energy conversion. A comparison of these conversion mechanisms is given by KAZMIERSKI and BEEBY in [25]. The capacitive transduction has, compared to the other two mechanisms, the disadvantage that an external energy source, providing an electric field, is required. In energy harvesting applications an external energy source is unwanted since it leads to a reduction of the efficiency. The systems using inductive energy conversion have the disadvantage that reducing the dimensions of the harvesting system to a lower scale significantly decreases the performance. In contrast to that, the piezoelectric transducers can be miniaturized without any loss of performance. Piezoelectric transducers have, compared to the other two mechanisms, a relatively high power density and can also be used in strong magnetic environment. A further advantage is that no disturbing magnetic fields affect the basic system, which is the case for inductive transducers. Of course, the choice of an appropriate energy transducer depends on the specific application.

Since in this work the piezoelectric transducer is used for the conversion of electric into mechanical energy, a short overview over the relevant constitutive equations is given.

A detailed introduction into the fundamentals of piezoelectricity can be found in [22, 33]. Some basic applications for energy harvesting systems are described by ERTURK and INMAN in [8]. Different aspects of the linear and nonlinear behavior of piezoelectric structures are described by VON WAGNER in [59] and by NGUYEN in [36].

In what follows, only the linear constitutive equations of a piezoelectric continuum

$$\begin{bmatrix} \boldsymbol{\epsilon} \\ \mathbf{D} \end{bmatrix} = \begin{bmatrix} \mathbf{s}^E & \mathbf{d}^{\mathrm{T}} \\ \mathbf{d} & \boldsymbol{\varepsilon}^\sigma \end{bmatrix} \begin{bmatrix} \boldsymbol{\sigma} \\ \mathbf{E} \end{bmatrix} \tag{2.27}$$

is used, where $\boldsymbol{\epsilon}$ and $\boldsymbol{\sigma}$ are the mechanical strain and stress tensors. The electric field and electric flux density tensors are $\mathbf{E}$ and $\mathbf{D}$. The material constants

are the compliance tensor $\mathbf{s}^E$ (evaluated for a constant electric field), the permittivity tensor $\boldsymbol{\varepsilon}^\sigma$ (evaluated for a constant stress field) and the piezoelectric constants tensor $\mathbf{d}$. In order to determine the electric field distribution within the structure depending on the electromechanical boundary conditions, the MAXWELL's equations are used. Often MAXWELL's equations are simplified assuming electrostatic behavior.

3 Wobbling disk generator

This chapter deals with the mathematical modeling and analysis of the wobbling disk generator. The equations of motion are derived based on a simplified model in order to determine the main influences of the system parameters on the dynamic behavior of the generator. The initiation of self-excited vibrations as well as the resulting steady-state characteristics are studied with respect to their applicability for energy harvesting systems.

3.1 Modeling

The simplified model of a wobbling disk generator, shown in Fig. 3.1, consists of three main parts, namely the rotor, stator and a piezoceramic structure. The external excitation is realized through the rotation of the rotor, which for example can be generated by excitation designs shown in Fig. 1.3. The rotor is pressed against the stator, which is connected to the piezoceramic through an elastic shaft. The electric power generation can be measured at the electric load (R) connected to the electrodes of the piezoceramic structure.

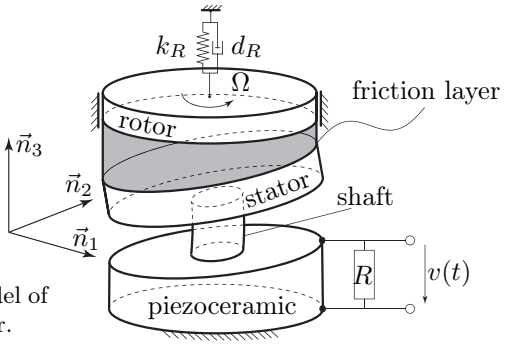

Figure 3.1: Simplified model of a wobbling disk generator.

The rotor and the stator are considered as rigid bodies, interacting through a visco-elastic friction layer. The rotor can rotate about the $\vec{n}_3$-axis and also translate along the $\vec{n}_3$-axis, whereas the stator has three rotational degrees of freedom. The visco-elastic friction layer is modeled by distributed spring-damper elements, which can be fixed to the rotor or to the stator surface, see Fig. 3.2. The interaction between the friction layer and the contact surface

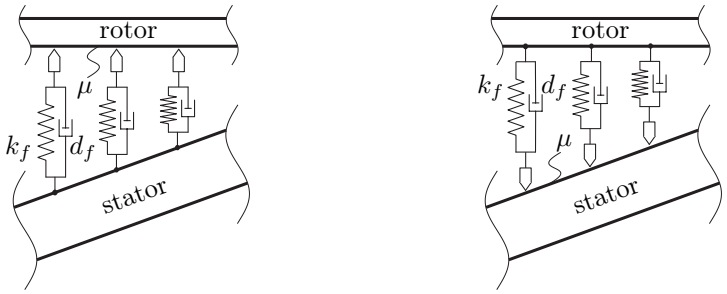

(a) Stator-fixed friction layer. **(b)** Rotor-fixed friction layer.

Figure 3.2: Different simplified mechanical models of the friction layer with pointwise visco-elastic properties.

is assumed to be pointwise and we use Coulomb's law of friction for the relation between the normal and tangential forces, despite being aware of a much more complicated contact behavior. Nevertheless, a simplified model with a constant friction coefficient is sufficient to show the main effects. The shaft connecting the stator with the piezoceramic is reduced to a massless spring-damper element. The upper surface of the piezoceramic is assumed to be rigid and is also described by rotational degrees of freedom. The surface of the piezoceramic is divided into four sections, two for each electrode; details are given later in section 3.1.3. A resistive load is connected to both electrode outputs. Maximizing the electric power output at these resistive loads is one of the main objectives of this work.

Regarding the modeling of the stator-rotor interaction, similar mechanical models exist in the literature, which also describe friction-induced vibrations of the stator modeled as wobbling disk. A minimal model for disk brake squeal

is derived by VON WAGNER et al. in [60]. The wobbling disk, which in this case represents the brake disk, is rotating and is in contact with an inertially fixed friction pin. Another minimal model, describing oscillations of friction clutches, is given by FIDLIN in [9]. Here, the wobbling disk also rotates and is in frictional contact with a rotation base. The frictional contact is distributed over the whole circumference of the disk.

3.1.1 Derivation of the equations of motion

For the derivation of the equations of motion the principle of virtual velocities, according to KANE and LEVINSON, is used. This principle is based on partial velocities, explained in detail in [24]. The notation introduced therein, is used in the following. Applying the principle of virtual velocities leads to the equations of motion for the stator

$$\left[\vec{M}_f + \vec{M}_S - \frac{{}^{\mathcal{N}}\mathrm{d}}{\mathrm{dt}}\left(\boldsymbol{\Theta}^{S/S_o}\,{}^{\mathcal{N}}\vec{\omega}^{S}\right)\right] \cdot {}^{\mathcal{N}}\vec{\omega}_i^{S} = 0, \qquad i = 1,2,3. \tag{3.1}$$

The equations of motion for the piezoceramic read

$$\left[\vec{M}_P - \vec{M}_S - \frac{{}^{\mathcal{N}}\mathrm{d}}{\mathrm{dt}}\left(\boldsymbol{\Theta}^{P/P_o}\,{}^{\mathcal{N}}\vec{\omega}^{P}\right)\right] \cdot {}^{\mathcal{N}}\vec{\omega}_j^{P} = 0, \qquad j = 1,2, \tag{3.2}$$

where $\vec{M}_f$ and $\vec{M}_S$ are torques resulting from the friction layer and from the visco-elastic connection of the shaft. The torque $\vec{M}_P$ results from the piezoelectric effect. The inertia tensor of the stator with respect to its center of mass is $\boldsymbol{\Theta}^{S/S_o}$ and the angular velocity is ${}^{\mathcal{N}}\vec{\omega}^{S}$. Analogously, the inertia tensor of the piezoceramic and the angular velocity are $\boldsymbol{\Theta}^{P/P_o}$ and ${}^{\mathcal{N}}\vec{\omega}^{P}$. In general, the angular velocity can be expressed as a linear combination of the generalized velocities u_{S_i}

$${}^{\mathcal{N}}\vec{\omega}^{S} = {}^{\mathcal{N}}\vec{\omega}_i^{S} u_{S_i}, \qquad i = 1,2,3\,, \tag{3.3}$$

where ${}^{\mathcal{N}}\vec{\omega}_i^{S}$ are the partial angular velocities. For a homogeneous disk (radius r, height h, mass m_S) the inertia tensor of the stator is

$$\boldsymbol{\Theta}^{S/S_o} = \begin{bmatrix} \Theta_S & 0 & 0 \\ 0 & \Theta_S & 0 \\ 0 & 0 & \Theta_3 \end{bmatrix}, \quad \Theta_S = m_S\,\frac{h^2 + 3r^2}{12},\ \Theta_3 = m_S\,\frac{r^2}{2}. \tag{3.4}$$

Carrying out the time derivative with respect to the inertial frame $\mathcal{N}$ in Eq. (3.1) yields

$$\left[\vec{M}_f + \vec{M}_S - \left(\mathbf{\Theta}^{S/S_o}\, {}^{\mathcal{N}}\vec{\alpha}^S + {}^{\mathcal{N}}\vec{\omega}^S \times \mathbf{\Theta}^{S/S_o}\, {}^{\mathcal{N}}\vec{\omega}^S\right)\right] \cdot {}^{\mathcal{N}}\vec{\omega}_i^S = 0,\ i = 1, 2, 3, \quad (3.5)$$

where ${}^{\mathcal{N}}\vec{\alpha}^S$ is the angular acceleration of the stator

$${}^{\mathcal{N}}\vec{\alpha}^S = \frac{{}^{\mathcal{N}}d}{dt}\left({}^{\mathcal{N}}\vec{\omega}^S\right). \quad (3.6)$$

Generalized coordinates and velocities

For different dynamic properties it makes sense to choose different generalized coordinates and generalized velocities. On the one hand, the analysis of the equations of motion can be significantly simplified, but on the other hand, in case of multi-body dynamics, different singular states can occur. In the analysis of the wobbling disk generator the two main tasks are the initiation of self-excitation and the optimization of the steady-state operation. For the former, the analysis is performed by linearizing the equations of motion around the trivial state. For this purpose, it is not possible to use the EULER angles, due to a singularity at the trivial state. A better choice for the description of the angular orientation of the stator are the CARDAN angles[1], which are used as generalized coordinates q_{S_i}. Using the CARDAN-123 description, the rotation matrix of the stator with respect to the inertial frame $\mathcal{N}$ results from three simple rotations

$$\begin{bmatrix}\vec{n}_1 & \vec{n}_2 & \vec{n}_3\end{bmatrix}^{\mathrm{T}} = {}^{\mathcal{N}}\mathbf{R}^{\mathcal{A}}\, {}^{\mathcal{A}}\mathbf{R}^{\mathcal{B}}\, {}^{\mathcal{B}}\mathbf{R}^{S} \begin{bmatrix}\vec{e}_{S_1} & \vec{e}_{S_2} & \vec{e}_{S_3}\end{bmatrix}^{\mathrm{T}} = {}^{\mathcal{N}}\mathbf{R}^{S} \begin{bmatrix}\vec{e}_{S_1} & \vec{e}_{S_2} & \vec{e}_{S_3}\end{bmatrix}^{\mathrm{T}}, \quad (3.7)$$

$${}^{\mathcal{N}}\mathbf{R}^{S} = \begin{bmatrix}1 & 0 & 0\\ 0 & c_1 & -s_1\\ 0 & s_1 & c_1\end{bmatrix} \begin{bmatrix}c_2 & 0 & s_2\\ 0 & 1 & 0\\ -s_2 & 0 & c_2\end{bmatrix} \begin{bmatrix}c_3 & -s_3 & 0\\ s_3 & c_3 & 0\\ 0 & 0 & 1\end{bmatrix}, \quad (3.8)$$

$${}^{\mathcal{N}}\mathbf{R}^{S} = \begin{bmatrix} c_2c_3 & -c_2s_3 & s_2\\ c_1s_3 + c_3s_1s_2 & c_1c_3 - s_1s_2s_3 & -c_2s_1\\ s_1s_3 - c_1c_3s_2 & c_3s_1 + c_1s_2s_3 & c_1c_2\end{bmatrix}, \quad (3.9)$$

[1] In literature CARDAN angles are also referred to as TAIT-BRYAN or *roll-pitch-yaw* angles.

where the symbols s_i and c_i denote $\sin q_{S_i}$ and $\cos q_{S_i}$ $(i = 1, 2, 3)$, respectively. A graphical representation of the CARDAN-123 rotation, which is equivalent to the rotation matrix (3.9) is given in [11, 24, 63]. The orientation vectors of the reference frames $\mathcal{A}$ and $\mathcal{B}$ in Eq. (3.7) are used in further calculations to keep the expressions simple. These orientation vectors can be expressed in the index notation as

$$\vec{a}_i = {}^{\mathcal{A}}r_{ij}^{\mathcal{N}}\,\vec{n}_j, \quad \vec{b}_i = {}^{\mathcal{B}}r_{ij}^{\mathcal{A}}\,\vec{a}_j, \tag{3.10}$$

where the ${}^{\mathcal{A}}r_{ij}^{\mathcal{N}}$ are the elements of the rotation matrix[2] ${}^{\mathcal{A}}\mathbf{R}^{\mathcal{N}}$. Using trivial kinematic differential equations for the generalized velocities

$$u_{S_i} = \dot{q}_{S_i}, \qquad i = 1, 2, 3, \tag{3.11}$$

leads to the partial angular velocities ${}^{\mathcal{N}}\vec{\omega}_i^S$

$$\begin{bmatrix} {}^{\mathcal{N}}\vec{\omega}_1^S & {}^{\mathcal{N}}\vec{\omega}_2^S & {}^{\mathcal{N}}\vec{\omega}_3^S \end{bmatrix} = \begin{bmatrix} \vec{n}_1 & \vec{a}_2 & \vec{b}_3 \end{bmatrix}. \tag{3.12}$$

Similarly, CARDAN angles q_{P_j} are used as generalized coordinates to describe the angular displacement of the upper surface of the piezoceramic, which is treated as rigid and massless. In comparison to the stator motion, the motion of the upper surface of the piezoceramic is described by only two degrees of freedom, where the yaw motion is neglected. Therefore, a CARDAN-12 rotation, which consists of two simple rotations, is applied on the piezo surface

$$\begin{bmatrix} \vec{n}_1 & \vec{n}_2 & \vec{n}_3 \end{bmatrix}^{\mathrm{T}} = {}^{\mathcal{N}}\mathbf{R}^{\mathcal{D}}\,{}^{\mathcal{D}}\mathbf{R}^{P} \begin{bmatrix} \vec{e}_{P_1} & \vec{e}_{P_2} & \vec{e}_{P_3} \end{bmatrix}^{\mathrm{T}} = {}^{\mathcal{N}}\mathbf{R}^{P} \begin{bmatrix} \vec{e}_{P_1} & \vec{e}_{P_2} & \vec{e}_{P_3} \end{bmatrix}^{\mathrm{T}}, \tag{3.13}$$

$${}^{\mathcal{N}}\mathbf{R}^{P} = \begin{bmatrix} 1 & 0 & 0 \\ 0 & c_1 & -s_1 \\ 0 & s_1 & c_1 \end{bmatrix} \begin{bmatrix} c_2 & 0 & s_2 \\ 0 & 1 & 0 \\ -s_2 & 0 & c_2 \end{bmatrix} = \begin{bmatrix} c_2 & 0 & s_2 \\ s_1 s_2 & c_1 & -c_2 s_1 \\ -c_1 s_2 & s_1 & c_1 c_2 \end{bmatrix}, \tag{3.14}$$

where the symbols s_j and c_j denote $\sin q_{P_j}$ and $\cos q_{P_j}$ $(j = 1, 2)$, respectively. In index notation the orientation vector of the reference frame $\mathcal{D}$ read

$$\vec{d}_i = {}^{\mathcal{D}}r_{ij}^{\mathcal{N}}\,\vec{n}_j. \tag{3.15}$$

[2] Remark: For orthogonal rotation matrices holds $({}^{\mathcal{A}}\mathbf{R}^{\mathcal{B}})^{-1} = ({}^{\mathcal{A}}\mathbf{R}^{\mathcal{B}})^{\mathrm{T}} = {}^{\mathcal{B}}\mathbf{R}^{\mathcal{A}}$.

Choosing trivial generalized velocities $u_{P_j} = \dot{q}_{P_j}$ $(j = 1, 2)$ leads to the following expression for the angular velocity

$$^{\mathcal{N}}\vec{\omega}^{P} = {}^{\mathcal{N}}\vec{\omega}_j^{P}\, u_{P_j}, \quad j = 1, 2, \qquad \text{with } \left[{}^{\mathcal{N}}\vec{\omega}_1^{P} \quad {}^{\mathcal{N}}\vec{\omega}_2^{P}\right] = \left[\vec{n}_1 \quad \vec{d}_2\right]. \quad (3.16)$$

The ${}^{\mathcal{N}}\vec{\omega}_j^{P}$ are the partial angular velocities of the upper surface of the piezoceramic.

Visco-elastic bedding torque

Besides the contact with the friction layer on the surface the stator is also bedded on a shaft on the lower surface (Fig. 3.1). The shaft mechanically connects the stator with the piezoceramic and is assumed to be massless with only restoring and damping properties. The resulting bedding torque $\vec{M}_S$ acting on the stator and the piezoceramic is

$$\vec{M}_S = -\sum_{i=1}^{3} \vec{M}_{S_i} + \sum_{j=1}^{2} \vec{M}_{P_j}, \qquad \text{with} \quad (3.17)$$

$$\vec{M}_{S_i} = \left(c_i\theta_i + d_i\dot{\theta}_i\right)\vec{v}_{S_i}, \qquad \vec{M}_{P_j} = \left(c_j\xi_j + d_j\dot{\xi}_j\right)\vec{v}_{P_j}, \quad (3.18)$$

where the stiffness and damping coefficients are $c_1 = c_2 = k_S, c_3 = k_t$ and $d_1 = d_2 = d_S, d_3 = d_t$. The angles θ_i and ξ_j are shown in Fig. 3.3. From geometry follows for the angles θ_i

$$\sin\theta_1 = \vec{e}_{S_1} \cdot \vec{n}_3, \quad \sin\theta_2 = \vec{e}_{S_2} \cdot \vec{n}_3, \quad \sin\theta_3 = \vec{e}_{S_1} \cdot \vec{n}_2, \quad (3.19)$$

and for the vectors $\vec{v}_{S_i}$

$$\vec{v}_{S_1} = \vec{e}_{S_1} \times \vec{n}_3, \quad \vec{v}_{S_2} = \vec{e}_{S_2} \times \vec{n}_3, \quad \vec{v}_{S_3} = \vec{e}_{S_1} \times \vec{n}_2. \quad (3.20)$$

Similarly follows for the angles ξ_j and the vectors $\vec{v}_{P_j}$

$$\sin\xi_1 = \vec{e}_{P_1} \cdot \vec{n}_3, \quad \sin\xi_2 = \vec{e}_{P_2} \cdot \vec{n}_3, \quad \vec{v}_{P_1} = \vec{e}_{P_1} \times \vec{n}_3, \quad \vec{v}_{P_2} = \vec{e}_{P_2} \times \vec{n}_3. \quad (3.21)$$

This description of the bedding torque $\vec{M}_S$ has the advantage that it is completely independent from the choice of the generalized coordinates and velocities. This is of importance in the first steps of the modeling process, where

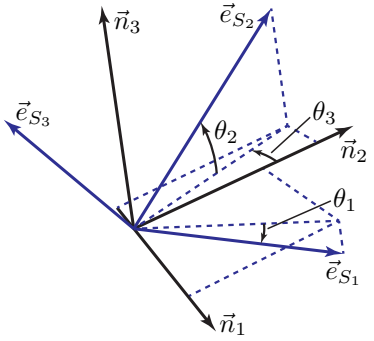

(a) Displacement of the lower stator surface.

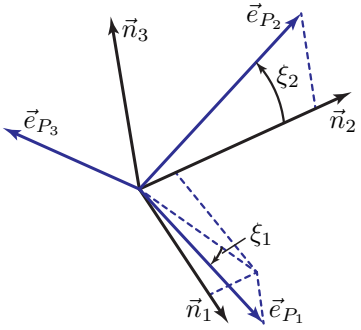

(b) Displacement of the upper surface of the piezoceramic.

Figure 3.3: Geometrical description of the connected surfaces of the stator and the piezoceramic structure.

it is not clear which generalized coordinates and velocities are the most appropriate ones. In a first step of the analysis the dynamics of the stator are analyzed separately from the piezoceramic. This can easily be done by setting $\vec{M}_{P_i} = \vec{0}$.

3.1.2 Frictional contact layer

In order to calculate the torque resulting from the friction layer, it is essential to state the kinematics of the friction layer as a function of the generalized coordinates and velocities. Depending on the assumption of the attachment of the friction layer[3], which can be a stator or rotor-fixed configuration, shown in Fig. 3.2, different kinematic relations are obtained. In the following, the modeling of the stator-fixed friction layer is not shown, but the main differences compared to the rotor-fixed configuration are discussed in section 3.1.4.

It is assumed that the friction layer is concentrated on the circumference of the rotor and consists of distributed linear spring-damper elements. Figure 3.4 shows a single spring-damper element in contact with the stator. The position

[3]It is assumed that both attachment designs, namely stator or rotor-fixed friction layer, can be realized by manufacturing.

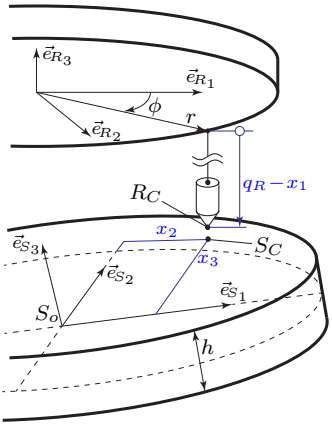

Figure 3.4:
Detailed kinematics of a single contact element for a rotor-fixed friction layer configuration.

vector of a single point of the contact line is given in the rotor-fixed reference frame by

$$ {}^{\mathcal{N}_o}\vec{p}^{\,R_C} = r\cos\phi\,\vec{e}_{R_1} + r\sin\phi\,\vec{e}_{R_2} + x_1\,\vec{e}_{R_3}. \tag{3.22} $$

The corresponding position vector of the contact point related to the stator is defined as

$$ {}^{\mathcal{N}_o}\vec{p}^{\,S_C} = x_2\,\vec{e}_{S_1} + x_3\,\vec{e}_{S_2} + \frac{h}{2}\vec{e}_{S_3}. \tag{3.23} $$

The unknown variables x_1, x_2 and x_3 from Eqs. (3.22) and (3.23) can be determined from the relation that ${}^{\mathcal{N}_o}\vec{p}^{\,R_C}$ and ${}^{\mathcal{N}_o}\vec{p}^{\,S_C}$ have to be equal. The absolute velocities of the contact points R_C and S_C can be calculated from

$$ {}^{R_C}\vec{v}^{\mathcal{N}} = \frac{{}^{\mathcal{N}}d}{dt}\left({}^{\mathcal{N}_o}\vec{p}^{\,R_C}\right), \qquad {}^{S_C}\vec{v}^{\mathcal{N}} = {}^{\mathcal{N}}\vec{\omega}^{S} \times {}^{\mathcal{N}_o}\vec{p}^{\,S_C}. \tag{3.24} $$

Figure 3.5a shows the free-body diagram of a contact element of the friction layer. The force in the contact pin acts in $\vec{e}_{R_3}$-direction and is given by

$$ \vec{f}_{\mathrm{Pin}} = \left[n_0 + k_f(x_1 - \frac{h}{2}) + d_f\dot{x}_1\right]\vec{e}_{R_3}, \quad n_0 = -k_f\,q_R - d_f\,\dot{q}_R. \tag{3.25} $$

The stiffness and damping coefficient of the spring-damper element are k_f and d_f. The pre-stress is n_0 and q_R is the generalized coordinate describing the

translatory motion of the rotor. The direction of the normal force is defined by the orientation of the stator surface,

$$\vec{f}_n = f_n \, \vec{e}_{S_3}. \tag{3.26}$$

Applying COULOMB's law of friction yields

$$\vec{f}_r = \mu \, |f_n| \, \frac{\Delta\vec{v}}{|\Delta\vec{v}|}, \qquad \text{with} \quad \Delta\vec{v} := {}^{\mathcal{N}}\vec{v}^{\,S_C} - {}^{\mathcal{N}}\vec{v}^{\,R_C}. \tag{3.27}$$

The friction coefficient is μ and the relative velocity between the two contact points R_C and S_C is given by $\Delta\vec{v}$. The contact forces $\vec{f}_n$ and $\vec{f}_r$ have to satisfy together with the force in the contact pin $\vec{f}_{\mathrm{Pin}}$ the force balance equation in the $\vec{e}_{R_3}$-direction (Fig. 3.5a)

$$\left(\vec{f}_n + \vec{f}_r - \vec{f}_{\mathrm{Pin}}\right) \cdot \vec{e}_{R_3} = 0. \tag{3.28}$$

The contact forces $\vec{f}_n$ and $\vec{f}_r$ can be determined by using the solution for the

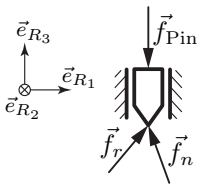

(a) Free-body diagram of a single contact point on the friction layer.

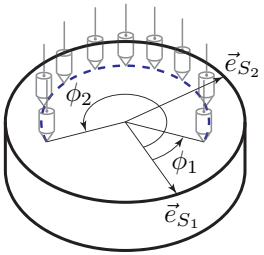

(b) Contact zone of the friction layer on the stator surface.

Figure 3.5: Forces at the friction layer and the distribution of the contact zone.

absolute value of the normal force f_n, obtained from Eq. (3.28). Integrating the resulting torque due to the contact forces ($\vec{m}_f$) over the whole contact line bounded by ϕ_1 and ϕ_2 yields

$$\vec{M}_f = \int_{\phi_1}^{\phi_2} \vec{m}_f \, \mathrm{d}\phi, \qquad \vec{m}_f = -{}^{\mathcal{N}_o}\vec{p}^{\,S_C} \times \left(\vec{f}_n + \vec{f}_r\right). \tag{3.29}$$

In general, the contact line in Fig. 3.5b is not fixed and the boundaries ϕ_1 and ϕ_2 depend nonlinearly on the generalized coordinates and velocities. Thus, using the general expression (3.29) requires numerical methods to solve the differential equation of the wobbling disk generator (3.1). Another possibility of handling Eq. (3.29) is to state assumptions concerning the distribution of the contact zone. In the case of initiation of self excitation, only the linearized equations of motion around the trivial solution are required. In this case, the complete circumference is in contact ($\phi_1 = 0, \phi_2 = 2\pi$). Through this assumption strongly simplified analytical expressions can be obtained. However, it has to be assured that the assumption is not violated, which means that no separation occurs ($f_n > 0$).

3.1.3 Piezoelectric effect

Due to the relatively small deflections, the inertia of the piezoceramic is neglected. This means that the dynamics of the piezo surface is described by two half-degrees of freedom[4]. This simplifies the equations of motion (3.2) to

$$\left[\vec{M}_P - \vec{M}_S\right] \cdot {}^{\mathcal{N}}\vec{\omega}_j^P = 0, \qquad j = 1, 2. \tag{3.30}$$

The torque $\vec{M}_P$, which results from the piezoelectric effect can be calculated through the integral of the cross product of the lever arm $\vec{r}$ and the stress $\vec{\sigma}$ over the surface A

$$\vec{M}_P = \int_{\mathrm{A}} (\vec{r} \times \vec{\sigma}) \, \mathrm{dA}. \tag{3.31}$$

Because of the design of the wobbling disk generator the so-called piezoelectric d_{33}-effect is predominating. This means that the applied stress and the resulting electric potential difference act in the same direction (here $\vec{n}_3$, see Fig. 3.1). Therefore, the integral for the torque $\vec{M}_P$ can be simplified to

$$\vec{M}_P = \int_{\mathrm{A}} (\vec{r} \times \sigma_{33} \, \vec{n}_3) \, \mathrm{dA}, \tag{3.32}$$

[4] A mechanical system with a half-degree of freedom is described by differential equation of first order, see [12].

where only stress in $\vec{n}_3$-direction is taken into account. The linear constitutive equations for the d_{33}-effect are

$$\begin{bmatrix} \sigma_{33} \\ D_3 \end{bmatrix} = \begin{bmatrix} E_P & -\gamma \\ \gamma & \nu \end{bmatrix} \begin{bmatrix} \epsilon_{33} \\ E_3 \end{bmatrix}, \quad \gamma = d_{33}\, E_P, \quad \nu = \varepsilon_{33} - d_{33}^2 E_P. \tag{3.33}$$

The strain, the stress, the electric field and the electric flux density in $\vec{n}_3$-direction are ϵ_{33}, σ_{33}, E_3 and D_3. The material parameters are YOUNG's modulus[5] E_P, the piezoelectric constant d_{33} and the permittivity ε_{33}. Adding a dissipative term proportional to the strain ratio (damping coefficient E_P^d), a modified expression for the stress is obtained

$$\sigma_{33} = E_P\, \epsilon_{33} + E_P^d\, \dot{\epsilon}_{33} - \gamma E_3. \tag{3.34}$$

The strain and the electric field are defined as

$$\epsilon_{33} = \frac{\delta u_P(z,t)}{\delta z}, \qquad E_3 = -\frac{\delta \Phi(z,t)}{\delta z}, \tag{3.35}$$

where u_P is the local displacement, Φ the electric potential and z the coordinate in $\vec{n}_3$-direction. The electromechanical boundary conditions, which have to be fulfilled for the piezoceramic with the height h_P are

$$u_P(0,t) = 0,\ u_P(h_P,t) = w_P(t), \quad \Phi(0,t) = 0,\ \Phi(h_P,t) = v(t). \tag{3.36}$$

The displacement of the upper surface of the piezoceramic is described by $w_P(t)$ and the electric voltage applied at the electrode surface is $v(t)$. Solving the boundary value problem[6] yields

$$\epsilon_{33} = \frac{w_P(t)}{h_P}, \qquad E_3 = -\frac{v(t)}{h_P}. \tag{3.37}$$

Using this solution, the expression for the stress (3.34) reduces to

$$\sigma_{33} = \frac{E_P}{h_P}\, w_P(t) + \frac{E_P^d}{h_P}\, \dot{w}_P(t) + \frac{\gamma}{h_P}\, v(t). \tag{3.38}$$

[5] In the literature the compliance $s_{33}^E = 1/E$ is often used instead of YOUNG's modulus E.

[6] A detailed electromechanical modeling of the piezoceramic is given by GUTSCHMIDT in [11], where the objective was to analyze the motor characteristics of the CANON bar-type ultrasonic motor.

Figure 3.6a shows the simplified deflection w_P of the upper surface of the piezoceramic. The position vector of a point on this surface can be expressed in the surface-fixed reference frame using the polar coordinates ϑ and ψ

$$\vec{r} = \vartheta\,(\cos\psi\,\vec{e}_{P_1} + \sin\psi\,\vec{e}_{P_2}). \tag{3.39}$$

Thus, for the vertical displacement $w_P(t)$ and its time derivative follows

$$w_P(t) = \vec{r}\cdot\vec{n}_3 = \vartheta\,\left[\cos\psi\,(\vec{e}_{P_1}\cdot\vec{n}_3) + \sin\psi\,(\vec{e}_{P_2}\cdot\vec{n}_3)\right], \tag{3.40}$$

$$\dot{w}_P(t) = \frac{d^{\mathcal{N}}\vec{r}}{dt}\cdot\vec{n}_3 = \vartheta\big[\cos\psi({}^{\mathcal{N}}\vec{\omega}^P\times\vec{e}_{P_1})\cdot\vec{n}_3 + \sin\psi({}^{\mathcal{N}}\vec{\omega}^P\times\vec{e}_{P_2})\cdot\vec{n}_3\big]\,. \tag{3.41}$$

The simplified electrode configuration of the piezoceramic surface, which is

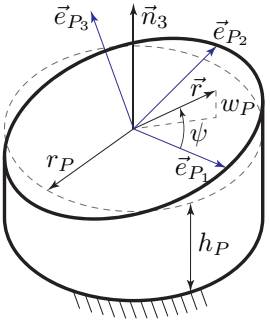

(a) Displacement of the piezoceramic surface.

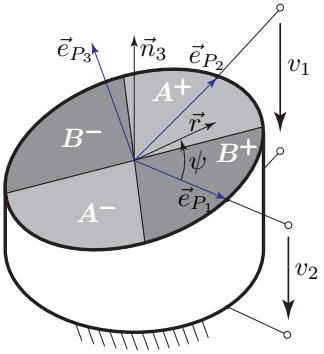

(b) Electrode configuration of the piezoceramic surface.

Figure 3.6: Forces at the friction layer and the distribution of the contact zone.

shown in Fig. 3.6b, consists of four unipotential segments A^+, A^-, B^+ and B^-. The superscript denotes the polarization direction of each segment. The segments A^+ and A^- are connected to one electrode and B^+ and B^- to another one, respectively. Under consideration of the given electrode configuration and the polarization direction the expression for the torque $\vec{M}_P$ (3.32) reduces to

$$\vec{M}_P = 2\int_0^{r_P}\left[\int_{-\frac{\pi}{4}}^{\frac{\pi}{4}}\sigma_{33}\Big|_{v=v_2}(\vec{r}\times\vec{n}_3)\,\mathrm{d}\psi + \int_{\frac{\pi}{4}}^{\frac{3\pi}{4}}\sigma_{33}\Big|_{v=v_1}(\vec{r}\times\vec{n}_3)\mathrm{d}\psi\right]\vartheta\,\mathrm{d}\vartheta. \tag{3.42}$$

Electric circuit equations

The piezoceramic has, besides the mechanical, also electrical degrees of freedom, which are represented by the potential difference at each electrode. The electric circuit for each electrode is illustrated in Fig. 3.7. The piezoceramic

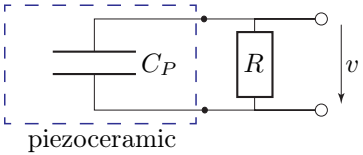

Figure 3.7: Simplified electric circuit for a single electrode.

is simplified to a capacitor with the capacity C_P. The electric power output is measured at the resistance R, which is attached at each electrode. By applying Gauss' law for the electric current at the electrode follows

$$\frac{\mathrm{d}}{\mathrm{dt}}\left(\int_{\mathrm{A}} D_3 \,\mathrm{dA}\right) = \frac{v}{R}, \tag{3.43}$$

where A is the surface of the electrode shown in Fig. 3.6b and D_3 is the dielectrical flux density of the piezoceramic. From the linear constitutive equations (3.33) D_3 is given as a function of the strain ϵ_{33} and the electric field E_3 in the $\vec{n}_3$-direction

$$D_3 = \gamma\,\epsilon_{33} + \nu\,E_3. \tag{3.44}$$

Using the solutions for the strain and the electric field (3.37) yields

$$D_3 = \frac{\gamma}{h_P}\,w_P - \frac{\nu}{h_P} v. \tag{3.45}$$

Inserting this solution for D_3 into the electric circuit equation (3.43) and taking the configuration for the electrodes A and B, Fig. 3.6b, into account yields

$$A: \qquad 2\int_0^{r_P}\int_{\frac{\pi}{4}}^{\frac{3\pi}{4}} \left(\frac{\gamma}{h_P}\,\dot{w}_P - \frac{\nu}{h_P}\dot{v}_1\right)\vartheta \mathrm{d}\psi\,\mathrm{d}\vartheta = \frac{v_1}{R}, \tag{3.46}$$

$$B: \qquad 2\int_0^{r_P}\int_{-\frac{\pi}{4}}^{\frac{\pi}{4}} \left(\frac{\gamma}{h_P}\,\dot{w}_P - \frac{\nu}{h_P}\dot{v}_2\right)\vartheta \mathrm{d}\psi\,\mathrm{d}\vartheta = \frac{v_2}{R}. \tag{3.47}$$

Rectification of the electric output signals

Every energy harvesting system requires a management system for the electric output signals, which provides power in an appropriate form for the storage system or the consuming device directly. Basically, in energy harvesting applications with a vibration-based energy source, the electric voltage output alternates with a specific frequency and needs to be rectified before further usage. A common rectifier, which provides a full-wave rectification, is the so-called GRAETZ bridge rectifier, shown in Fig. 3.8. Exemplarily, the voltage

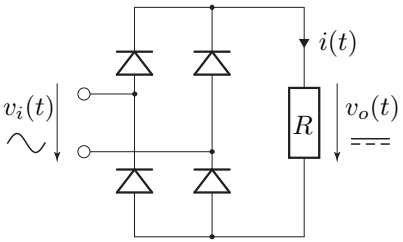

Figure 3.8: Rectification of on alternating electric voltage with a GRAETZ bridge rectifier.

transfer characteristic of the GRAETZ bridge rectifier is shown in Fig. 3.9. The input voltage $v_i(t)$, displayed in Fig. 3.9a, is a harmonic signal with the amplitude $\hat{v}$ and the period T. Through the rectification the input voltage is transformed into the output voltage $v_o(t)$, which has the time signal shown

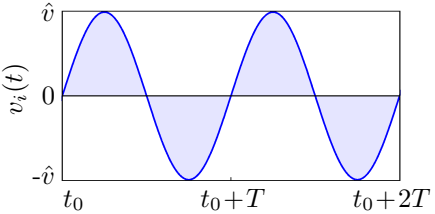

(a) Voltage at the input of the bridge rectifier.

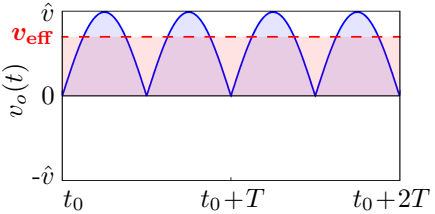

(b) Voltage at the output of the bridge rectifier; dashed line: v_{eff}.

Figure 3.9: Voltage transfer characteristics of a GRAETZ bridge rectifier.

in Fig. 3.9b. The effective electric power output at the resistance R reads

$$P_{\text{eff}} = \frac{1}{T}\int_{t_0}^{t_0+T} v_o(t)\, i(t)\,\mathrm{d}t = \frac{1}{T}\int_{t_0}^{t_0+T} \frac{v_o(t)^2}{R}\mathrm{d}t. \tag{3.48}$$

The effective power output can be expressed using the effective voltage v_{eff} as

$$P_{\text{eff}} = \frac{v_{\text{eff}}^2}{R}, \qquad \text{with} \quad v_{\text{eff}} = \sqrt{\frac{1}{T}\int_{t_0}^{t_0+T} v_o^2(t)\,\mathrm{d}t}\,. \tag{3.49}$$

For the special case of a harmonic input voltage the relation between the voltage amplitude $\hat{v}$ and the effective voltage v_{eff} is

$$v_{\text{eff}} = \frac{\sqrt{2}}{2}\,\hat{v} \qquad \Rightarrow \qquad P_{\text{eff}} = \frac{1}{2}\frac{\hat{v}^2}{R}\,. \tag{3.50}$$

3.1.4 Linearized equations of motion

In this section, the linearized equations of motion of the wobbling disk generator are analyzed with respect to the initiation of self-excited oscillations. In a first step, the stator-rotor system is discussed separately from the piezoceramic structure, in order to highlight the main effects of the friction layer. Afterwards, the mechanical coupling of the piezocermic on the stator-rotor system is taken into account and the electric-circuit equations are analyzed with respect to the electric power output.

Linearized equations of motion of the stator-rotor system

The trivial solution of the stator-rotor system is defined as the equilibrium position of the system after pressing the rotor against the stator. Through the linearization of the equations of motion (3.1) around this trivial solution, the degrees of freedom of the stator-rotor system decouple. Only the CARDAN angles q_{S_1} and q_{S_2} are coupled. The corresponding linearized equations of motion are of the form

$$\mathbf{M}\,\ddot{\mathbf{q}}_S + (\mathbf{D}+\mathbf{G})\,\dot{\mathbf{q}}_S + (\mathbf{K}+\mathbf{N})\,\mathbf{q}_S = \mathbf{0}, \qquad \mathbf{q}_S = [q_{S_1}, q_{S_2}]^{\mathrm{T}}, \tag{3.51}$$

$$\mathbf{M}=\begin{bmatrix} m & 0 \\ 0 & m \end{bmatrix}, \mathbf{D}=\begin{bmatrix} d & 0 \\ 0 & d \end{bmatrix}, \mathbf{G}=\begin{bmatrix} 0 & -g \\ g & 0 \end{bmatrix}, \mathbf{K}=\begin{bmatrix} k_1 & b \\ b & k_2 \end{bmatrix}, \mathbf{N}=\begin{bmatrix} 0 & -n \\ n & 0 \end{bmatrix}. \tag{3.52}$$

The matrices $\mathbf{M}, \mathbf{D}$ and $\mathbf{K}$ are the mass, damping and stiffness matrix with the properties

$$\mathbf{M} = \mathbf{M}^{\mathrm{T}},\ \mathbf{D} = \mathbf{D}^{\mathrm{T}},\ \mathbf{K} = \mathbf{K}^{\mathrm{T}} \quad \text{(symmetric, positive definite)}. \tag{3.53}$$

The gyroscopic and circulatory matrix $\mathbf{G}$ and $\mathbf{N}$ have the properties

$$\mathbf{G} = -\mathbf{G}^{\mathrm{T}},\ \mathbf{N} = -\mathbf{N}^{\mathrm{T}} \quad \text{(skew-symmetric)}. \tag{3.54}$$

It has to be pointed out that the equations of motion (3.51) are homogeneous and no forcing terms, which may result from external excitation, are present at the right-hand side. The terms in the gyroscopic matrix $\mathbf{G}$ do not contribute to the energy level of the system, but may affect the stability behavior. The energy input in the system is done by non-conservative forces through the circulatory terms in the matrix $\mathbf{N}$. The origin of this non-conservative forces lies in the friction layer between the rotor and the stator. In case of linear systems with forced excitation the steady-state solution is basically of the type of the right-hand side, which is obtained by calculating the particular solution of the inhomogeneous problem. In contrast to that, for a self-excited system, a different approach has to be used to obtain the steady-state solution. First, the linearized equations of motion are analyzed with respect to the stability behavior of the trivial solution. Once the trivial solution is destabilized, stable limit-cycle oscillations may occur. The dynamic properties of the limit cycle depends on the nonlinear terms in the equations of motion. Therefore an additional analysis of the nonlinear system is required, in order to determine the steady-state characteristic required for an energy harvesting application.

For a rotor and stator-fixed friction layer the entries of the matrices (3.52) are given in Tab. 3.1. The entry in the mass matrix (m) is equal to the moment of inertia of the stator Θ_S. The stiffness parameters k_1 and k_2 consists of the stiffness coefficient of the shaft k_S, the stiffening part due to the pre-stress n_0 and the stiffness coefficient of the friction layer k_f. Moreover, the parameter α is introduced, which allows the perturbation of the symmetry of the stiffness properties of the shaft. Through the linearization the expression for the distributed pre-stress (3.25) simplifies. Inserting the constant displacement of

the rotor due to the pre-stress force yields

$$n_0 = -k_f\, q_R^* = \frac{k_f}{k_R + 2\,\pi\, k_f}\, N_0, \tag{3.55}$$

where N_0 is the pre-load on the rotor. The entry of the damping matrix (d) consists of the following damping mechanisms: material damping of the shaft (d_S), material damping of the friction layer (d_f) and damping due to COULOMB friction. Besides the additional damping effect, the friction layer also leads to circulatory and gyroscopic terms n and g. The latter one is negligible due to the relatively small damping coefficient of the friction layer ($d_f \ll 1$). Furthermore, the contribution of the friction layer to the stiffness properties through b is of minor importance, compared to other stiffness parameters, and therefore is neglected in the further analysis. The differences of the parameters of the stator-fixed to the rotor-fixed configuration (Tab. 3.1) are due to the pre-stress n_0 in the parameters k_1, k_2 and n. However, these differences are of a much lower magnitude compared to the contribution of

Table 3.1: Entries of the matrices (3.52) for different friction layer configuration.

symbol	rotor-fixed layer	stator-fixed layer
m	$\Theta_S = m_S \left(\frac{h^2+3r^2}{12}\right)$	$\Theta_S = m_S \left(\frac{h^2+3r^2}{12}\right)$
d	$d_S + \pi r^2 d_f + \mu\,\pi \frac{h^2}{4} \frac{n_0}{r\sqrt{\Omega^2}}$	$d_S + \pi r^2 d_f + \mu\,\pi \frac{h^2}{4} \frac{n_0}{r\sqrt{\Omega^2}}$
g	$\mu\,\pi \frac{h}{2} r\, d_f \operatorname{sign}\Omega$	$\mu\,\pi \frac{h}{2} r\, d_f \operatorname{sign}\Omega$
k_1	$k_S + \pi h n_0 + \pi r^2 k_f$	$k_S - \pi h n_0 + \pi r^2 k_f$
k_2	$\alpha\, k_S + \pi h n_0 + \pi r^2 k_f$	$\alpha\, k_S - \pi h n_0 + \pi r^2 k_f$
b	$-\mu\,\pi\, r\, n_0 \operatorname{sign}\Omega$	$-\mu\,\pi\, r\, n_0 \operatorname{sign}\Omega$
n	$\mu\,\pi \frac{h}{2} r\, k_f \operatorname{sign}\Omega$	$\mu\,\pi \frac{h}{2} \left(r\, k_f - \frac{h}{2r} n_0\right) \operatorname{sign}\Omega$

the stiffness of the friction layer ($n_0 \ll hk_f$) and therefore only have a negligible effect on the dynamic behavior. This is also confirmed by numerical simulation of the equations of motion. Thus, it can be concluded that only the properties of the friction layer and not its attachment configuration affects the dynamics of the stator-rotor system. The parameter set for the rotor-fixed friction layer is used in the further analysis.

Electromechanical coupling

In the following, the mechanical connection of the piezoceramic structure to the stator, which is realized through the shaft, is taken into account. The linearized equations of motion for the generalized coordinates $\mathbf{q}_S = [q_{S_1}, q_{S_2}]^{\mathrm{T}}$ of the stator, which also include the deformation of the piezoceramic are

$$\mathbf{M}\,\ddot{\mathbf{q}}_S + (\mathbf{D}+\mathbf{G})\,\dot{\mathbf{q}}_S + (\mathbf{K}+\mathbf{N})\,\mathbf{q}_S = \mathbf{D}_S\,\dot{\mathbf{q}}_P + \mathbf{K}_S\,\mathbf{q}_P. \tag{3.56}$$

The matrices $\mathbf{M}, \mathbf{D}, \mathbf{G}, \mathbf{K}$ and $\mathbf{N}$ correspond to the matrices of the linearized equations of motion of the decoupled system (3.51). The mechanical generalized coordinates of the piezoceramic are $\mathbf{q}_P = [q_{P_1}, q_{P_2}]^{\mathrm{T}}$, describing the deflection of the upper surface and the electrical ones are $\mathbf{v} = [v_1, v_2]^{\mathrm{T}}$, which describe the electric potential at the electrodes. Linearization of the equations of motion of the upper surface of the piezoceramic abound the trivial solution yields

$$\mathbf{D}_P\,\dot{\mathbf{q}}_P + \mathbf{K}_P\,\mathbf{q}_P + \mathbf{\Gamma}\,\mathbf{v} = \mathbf{D}_S\,\dot{\mathbf{q}}_S + \mathbf{K}_S\,\mathbf{q}_S. \tag{3.57}$$

The damping, stiffness and piezoelectric coupling matrix of the piezoceramic are $\mathbf{D}_P, \mathbf{K}_P$ and $\mathbf{\Gamma}$, which are all diagonal

$$\mathbf{D}_P = \begin{bmatrix} d_P + d_S & 0 \\ 0 & d_P + d_S \end{bmatrix},\ \mathbf{K}_P = \begin{bmatrix} k_P + k_S & 0 \\ 0 & k_P + \alpha k_S \end{bmatrix},\ \mathbf{\Gamma} = \begin{bmatrix} \Gamma_P & 0 \\ 0 & \Gamma_P \end{bmatrix}. \tag{3.58}$$

The abbreviations for the damping, stiffness and piezoelectric coupling coefficient of the piezoceramic read

$$d_P = \pi \frac{r_P^4}{4} \frac{E_P^d}{h_P}, \quad k_P = \pi \frac{r_P^4}{4} \frac{E_P}{h_P}, \quad \Gamma_P = \frac{2\sqrt{2}}{3}\, r_P^3\, \frac{\gamma}{h_P}. \tag{3.59}$$

The mechanical coupling matrices in Eqs. (3.56) and (3.57) are also diagonal and represent the restoring and damping properties of the shaft

$$\mathbf{D}_S = \begin{bmatrix} d_S & 0 \\ 0 & d_S \end{bmatrix}, \quad \mathbf{K}_S = \begin{bmatrix} k_S & 0 \\ 0 & \alpha\, k_S \end{bmatrix}. \tag{3.60}$$

Linearizing the electric circuit equations yields

$$\begin{bmatrix} C_P & 0 \\ 0 & C_P \end{bmatrix} \dot{\mathbf{v}} + \begin{bmatrix} 1/R_1 & 0 \\ 0 & 1/R_2 \end{bmatrix} \mathbf{v} - \begin{bmatrix} \Gamma_P & 0 \\ 0 & \Gamma_P \end{bmatrix} \dot{\mathbf{q}}_P = \mathbf{0}, \tag{3.61}$$

where the electric resistance at each electrode is R_i and the capacity of the piezoceramic is given by $C_P = \frac{\pi}{2}\, r_P^2\, \nu / h_P$.

The electric circuit equations (3.61), the equations of motion of the stator (3.56) and the piezoceramic (3.57) can be put together to a system describing the complete electromechanical behavior. Since this is a straight-forward procedure it is not shown here. Splitting the system matrices into their symmetric and asymmetric parts gives information about the influence of the parameters on the dynamic behavior of the system. Through the mechanical connection of the piezoceramic to the stator, the mass, damping and stiffness matrices were extended by the corresponding properties of the piezoceramic structure and the electric circuit, respectively. Furthermore, the gyroscopic matrix was extended by the contribution, resulting from the piezoelectric coupling through Γ_P. However, besides the previously mentioned circulatory terms, resulting from the friction layer, no other non-conservative effects are present in the extended system. This also means that only the generalized coordinates q_{S_1} and q_{S_2} can be destabilized by the circulatory terms leading to self-excited oscillations of the stator. Thus, the transient behavior of this coordinates predominates the general dynamic behavior of the whole system. For this reason, the linearized equations of motion can be used to calculate transfer functions based on the steady-state solution of the stator. Using these transfer functions, the transmission characteristics between the different coordinates can be analyzed. To this end, harmonic functions of the form

$$q_{S_j}^*(t) = \underline{\hat{q}}_{S_j}\, e^{\mathrm{i}\,\Omega_w t}, \qquad q_{P_j}^*(t) = \underline{\hat{q}}_{P_j}\, e^{\mathrm{i}\,\Omega_w t}, \qquad v_j^*(t) = \underline{\hat{v}}_j\, e^{\mathrm{i}\,\Omega_w t}, \tag{3.62}$$

are used for the steady-state solution. Inserting these expressions into the linearized equations of motion (3.57) and (3.61) yields

$$\frac{\hat{\underline{v}}_j}{\hat{\underline{q}}_{P_j}} = \underline{V}_P = \frac{\Omega_w R_j \, \Gamma_P}{\Omega_w R_j \, C_P - \mathrm{i}}, \tag{3.63}$$

$$\frac{\hat{\underline{q}}_{P_j}}{\hat{\underline{q}}_{S_j}} = \underline{V}_S = \frac{k_S + \mathrm{i}\,\Omega_w d_S}{k_P + k_S + \mathrm{i}\,\Omega_w (d_P + d_S) + \Gamma_P \, \underline{V}_P}. \tag{3.64}$$

For the sake of clarity, the stiffness properties of the shaft (3.60) are assumed to be symmetric ($\alpha = 1$). The complex transfer functions $\underline{V}_P$ and $\underline{V}_S$ describe the transmission characteristics between the mechanical coordinate of the piezoceramic q_{P_j}, the corresponding electric state v_j and the coordinate of the stator q_{S_j}. Using these transfer functions for the effective power output P_{eff} at each resistance R_j gives

$$P_{\text{eff}} = \frac{1}{2} \frac{|\hat{\underline{v}}_j|^2}{R_j} = \frac{|\underline{V}_P \, \underline{V}_S \, \hat{\underline{q}}_{S_j}|^2}{2R_j}. \tag{3.65}$$

Neglecting the influence of the damping coefficients d_S and d_P the expression for the effective power output (3.65) simplifies to

$$P_{\text{eff}} = \frac{1}{2} \frac{R_j \left(k_S \, \Omega_w \Gamma_P\right)^2}{\left[(k_P + k_S) C_P + \Gamma_P^2\right]^2 \Omega_w^2 R_j^2 + (k_P + k_S)^2} \, |\hat{\underline{q}}_{S_j}|^2. \tag{3.66}$$

In the case, where the amplitude of the stator motion $|\hat{\underline{q}}_{S_j}|$ is nearly independent[7] from the dynamics of the piezoceramic, the optimum resistance, which maximizes the effective power output reads

$$1/R_j^* = \left(C_P + \frac{\Gamma_P^2}{k_S + k_P} \right) \Omega_w. \tag{3.67}$$

Since the properties of the shaft and the piezoceramic were assumed to be symmetric, the optimum values for the resistance at each electrode are equal

[7] This is the case, where the dynamic behavior of the stator-rotor system is almost unaffected by the dynamics of the piezoceramic and can be analyzed separately. Then, the wobbling motion of the stator leads to forced vibrations of the piezoceramic structure. How strong or weak this feedback effect is, depends on the mechanical properties of the connecting shaft.

($R_1^* = R_2^* = R_j^*$). Inserting R_j^* into the expression for the effective power (3.66) leads to the maximum

$$P_{\text{eff}}^{\max} = \frac{\Omega_w \left(k_S \, \Gamma_P\right)^2}{4(k_P + k_S) \, [(k_P + k_S)C_P + \Gamma_P^2]} \, |\hat{\underline{q}}_{S_i}|^2. \tag{3.68}$$

The maximum power output increases linearly with the frequency Ω_w and quadratically with the amplitude $|\hat{\underline{q}}_{S_i}|$ of the wobbling motion of the stator. But it has to be kept in mind that this relation is only fulfilled for negligible feedback effect of the piezoceramic structure on the stator vibrations.

3.2 Initiation of self-excited vibrations

In this section, the initiation of self-excited vibrations is analyzed on the one hand, based on the derived equations of motion for the simplified model and on the other hand, based on a finite element model of the stator-rotor system.

3.2.1 Stability behavior of the trivial solution

In order to determine, whether self-excited vibrations are initiated, the system (3.51) has to be studied with respect to the stability behavior of the trivial solution. If the trivial solution becomes unstable, in the sense of a flutter-type instability, then self-excited oscillations can occur. The difference between the flutter-type instability and other instability phenomena, such as a divergence-type instability, was discussed in section 2.1.2, by using a simple example of a system with self-excitation. The analysis method to determine the stability behavior of the trivial solution depends on whether the differential equations are autonomous[8] or not. In the case, where the pre-stress force N_0 and the rotation speed of the rotor Ω are constant, the differential equations describing the dynamics of the stator (3.51) are autonomous. For such a system the stability behavior can be determined by analyzing the real parts of the eigenvalues of the characteristic equation

$$\det\left(\lambda^2 \, \mathbf{M} + \lambda(\mathbf{D} + \mathbf{G}) + \mathbf{K} + \mathbf{N}\right) = 0. \tag{3.69}$$

[8] A system of ordinary differential equations is autonomous if it does not depend explicitly on time. Such systems are also referred to as time-invariant.

In general, the eigenvalues of this system appear in conjugate complex form, where the imaginary parts are equivalent to the oscillation frequencies and the real parts to the exponential growth of the solution of the linearized system. In order to highlight a characteristic bifurcation of the eigenvalues, the imaginary and real parts of the eigenvalues are illustrated in Fig. 3.10. The parameters for the wobbling disk generaor with a rotor-fixed friction layer, given in Tab. 3.2, are used with an additional perturbation of the stiffness properties of the shaft ($\alpha = 0.9$). Choosing the friction coefficient μ as the bifurcation parameter, allows to display different influences of the friction layer, starting from a frictionless system for $\mu = 0$. Due to the perturbation

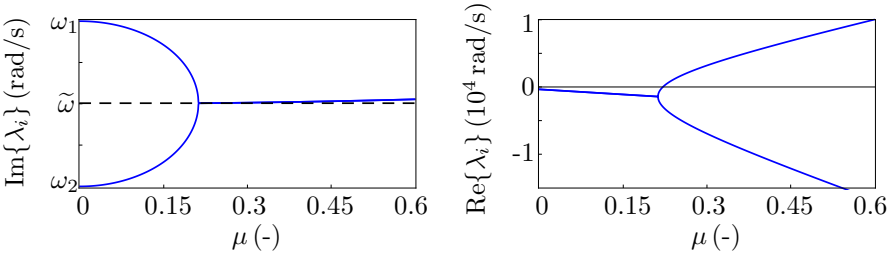

(a) Imaginary part of the eigenvalues over μ; dashed line: natural frequency $\widetilde{\omega}$.

(b) Real part of the eigenvalues over μ.

Figure 3.10: Bifurcation diagram of the eigenvalues of the wobbling disk generator: Variation of the friction coefficient μ for $\alpha = 0.9$.

through α the eigenfrequencies[9] are unequal ($\omega_1 \neq \omega_2$) and approach each other for an increasing μ, see Fig. 3.10a. This is mainly caused by an increasing influence of the circulatory terms due to friction. Moreover, it can be observed that for a specific μ the eigenfrequencies coincide and afterwards stay almost constant independently from a further increase of μ. In the literature, this phenomenon is also referred to as *lock-in* or *mode-coupling* phenomenon, see [21]. In Fig. 3.10b the corresponding real parts of the eigenvalues are

[9] Figure 3.10a shows only the positive imaginary parts of the eigenvalues. The corresponding negative imaginary parts show the same bifurcation behavior and would give no further information.

plotted over μ. For a relatively small μ, the additional damping effect due to friction leads to slightly lower real parts and has therefore a *stabilizing* effect. Nevertheless, this effect vanishes by a further increase of μ, since the destabilizing circulatory terms become more dominant. After the bifurcation point, one real part increases and becomes positive. This also means that the system becomes unstable or self-excited, respectively.

Since the gyroscopic term in Eq. (3.51) is neglected, the expressions for the eigenvalues of the characteristic equation (3.69) strongly simplify. The general solution for the imaginary parts of the eigenvalues for a (2×2)-system of the type (3.52) is given in Eq. (2.22). Using this expression for the eigenfrequencies ω_1 and ω_2 (Fig. 3.10a for $\mu = 0$), follows

$$\omega_j^2 = \frac{k_j}{m} - \frac{d^2}{4m^2}, \qquad j = 1, 2. \tag{3.70}$$

These are the eigenfrequencies of the completely decoupled system, where the only difference between k_1 and k_2 results from the perturbation through α. For the case, where the eigenfrequencies coincide ($\omega_1 = \omega_2$), the corresponding double eigenfrequency reads

$$\omega^2 = \frac{1}{2}\left(a_\omega + \sqrt{a_\omega^2 - b_\omega^2}\right) \approx \widetilde{\omega}^2 = a_\omega = \frac{k}{m} - \frac{d^2}{4m^2}. \tag{3.71}$$

Since in this case $a_\omega^2 \gg b_\omega^2$, the estimate for the double eigenfrequency $\omega \approx \widetilde{\omega}$ can be used instead. This estimate is plotted in Fig. 3.10a together with the imaginary parts of the eigenvalues and matches very well the exact double eigenfrequency. Basically, in the case of self-excited vibrations this double eigenfrequency can have a significant influence on the resulting limit-cycle oscillations and therefore an estimate for this frequency can be very useful, as shown in section 3.3.

The linearized system (3.51) is unstable if at least one $\mathrm{Re}\{\lambda_i\} > 0$. Using the ROUTH scheme or the HURWITZ stability criterion, respectively, the condition for a flutter-type instability can be stated as

$$d^2\, m \left(b^2 + \Delta k^2\right) + \left(d^2 + g^2\right)\left(d^2 k + d\, g\, n - m\, n^2\right) < 0. \tag{3.72}$$

Here, the abbreviations $k = (k_1 + k_2)/2$ and $\Delta k = (k_1 - k_2)/2$ are used. Since the gyroscopic effect caused by the friction layer can be neglected ($d_f \ll 1$),

the instability condition simplifies to

$$d^2\,\omega_0^2 + (b^2 - n^2 + \Delta k^2) < 0, \qquad \omega_0^2 = \frac{k}{m}. \tag{3.73}$$

Inserting the parameters for the rotor-fixed configuration (Tab. 3.1) yields

$$\left(d_S + \pi r^2 d_f + \frac{\mu\,\pi h^2 n_0}{4r\sqrt{\Omega^2}}\right)^2 \omega_0^2 + (\mu\pi r\, n_0)^2 - \left(\mu\pi \frac{h}{2} r\, k_f\right)^2 + \left(\frac{1-\alpha}{2} k_S\right)^2 < 0, \tag{3.74}$$

$$\omega_0^2 = \frac{\frac{1+\alpha}{2} k_S + \pi h n_0 + \pi r^2 k_f}{\Theta_S}. \tag{3.75}$$

By setting the left-hand side of the inequality equal to zero, the expression for the so-called bifurcation point is obtained. The bifurcation point describes the boundary in the parameter space between regions of different types of solutions of a system of differential equations. A detailed analysis of the steady-state solutions of the wobbling disk generator is given in section 3.3.

Approximation of the stability boundary

In the following, the boundary of the region, where flutter-type instability can occur, is studied in detail. The aim is to give approximations of this boundary, based on the instability condition (3.74). To this end, the stabilizing effect of the material damping is neglected ($d_S = d_f = 0$). Assuming symmetric stiffness properties of the shaft ($\alpha = 1$) yields

$$n_0^{\max} = \frac{\frac{h}{2} k_f}{\sqrt{1+\eta^2}}, \qquad \text{with} \quad \eta^2 = \frac{h^4}{16 r^4} \frac{\omega_0^2}{\Omega^2}. \tag{3.76}$$

This critical value gives the boundary up to which pre-stress ($n_0 < n_0^{\max}$) self-excited vibrations can occur. For larger pre-stress the damping effect due to Coulomb's friction stabilizes the system. A further simplification of the expression for the maximum pre-stress (3.76) is obtained by comparing the frequencies ω_0 and Ω . Since the natural frequency is much higher than the rotation speed of the rotor ($\omega_0 \gg \Omega$) the expression simplifies to

$$n_0^{\max} \approx \frac{r^2 k_f\,|\Omega|}{\frac{h}{2}\omega_0}. \tag{3.77}$$

Analogously, the critical values for the rotation speed Ω and the natural frequency of the wobbling disk ω_0 can be given as functions of the other system parameters,

$$\Omega^{\min} \approx \frac{\frac{h}{2}n_0}{r^2 k_f}\omega_0, \qquad \omega_0^{\max} \approx \frac{r^2 k_f}{\frac{h}{2}n_0}|\Omega|. \tag{3.78}$$

These expressions represent the lower boundary for the rotation speed of the rotor ($\Omega > \Omega^{\min}$) and the upper boundary for the natural frequency of the stator ($\omega_0 < \omega_0^{\max}$). Similarly, the boundary for the maximum allowed perturbation of the symmetry properties of the shaft, through the parameter α, can be calculated. Neglecting all damping mechanisms by setting $d_S = d_f = 0, n_0 = 0$ yields

$$\Delta\alpha^{\max} = |\alpha - 1|^{\max} = \mu\pi hr\frac{k_f}{k_S}. \tag{3.79}$$

This critical value for $\Delta\alpha$ can be increased by a higher friction coefficient or a higher ratio between the stiffness coefficient of the friction layer and the shaft. Although all damping mechanisms were neglected, the system is still stable for $\Delta\alpha > \Delta\alpha^{\max}$. This stabilizing effect through an appropriate configuration of the mechanical structure is well-known in the literature, for example in the field of 'suppression of self-excited vibrations', analyzed by Spelsberg-Korspeter in [49, 51]. For an energy harvesting application it is important to assure that the perturbation of the stiffness properties does not exceed this critical value. If the perturbation $\Delta\alpha$ is known, the expression (3.79) can be used to give a conservative approximation for the friction coefficient, which is needed to initiate self-excited vibrations,

$$\mu^{\min} = \frac{|\Delta\alpha|\, k_S}{\pi r h\, k_f}. \tag{3.80}$$

In the following, stability maps for different system and excitation parameters of the wobbling disk generator are shown, using the parameter set given in Tab. 3.2 (damping considered). The region, where flutter-type instability can occur, is described by the inequality (3.74) and is denoted in the graph as *unstable*. Analogously, in the region denoted as *stable,* no self-excited

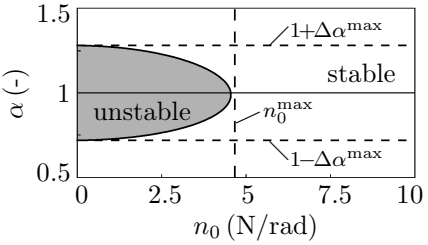

(a) Stability boundary in the n_0-α-plane; dashed lines: critical values, ($\Omega = 10\,\mathrm{rad/s}$).

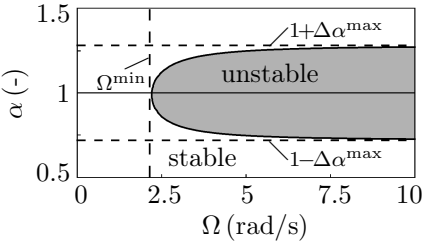

(b) Stability boundary in the Ω-α-plane; dashed lines: critical values, ($n_0 = 0.1\,\mathrm{N/rad}$).

Figure 3.11: Stability map of the wobbling disk generator: Perturbation of the stiffness properties of the wobbling disk over the excitation parameter n_0 and Ω.

vibrations occur. Figure 3.11 shows the stability map over α and the input paramters n_0 and Ω together with the derived conservative approximation of the stability boundary (3.77) - (3.79). The instability region in Fig. 3.11a exists only up to a maximum pre-stress $n_0 < n_0^{\max}$, where the damping effect due to COULOMB's friction is less significant. From Fig. 3.11b it is obvious that a minimum rotation speed required to initiate self excitation. Moreover, it can be observed that for symmetric stiffness properties of the shaft ($\alpha = 1$) the instability region is maximum. Introducing asymmetry ($\alpha \neq 1$) reduces the instability region and can make it completely disappear for $\Delta\alpha > \Delta\alpha^{\max}$. Such asymmetries have to be avoided in generators for energy harvesting applications. In applications like brake disks, where self-excited vibrations have to be suppressed, such asymmetries are introduced systematically to ensure global stability [50, 61]. In Fig. 3.12 the stability map is plotted over the friction coefficient and the input parameters n_0 and Ω. The estimate $\mu^{\min}$ gives the lower boundary for the friction coefficient μ. However, if the friction coefficient is large enough so that self-excitation can occur, an increase of μ does not give any significant advantage. In addition to the previously given stability maps, Fig. 3.13 shows how the natural frequency of the stator f_S affects the stability boundary. This natural frequency corresponds to the system, where all effects due to the contact are neglected, such as pre-stress or

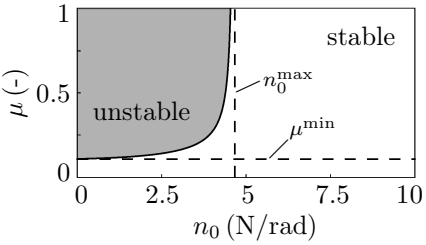

(a) Stability boundary in the n_0-μ-plane; dashed lines: critical values, ($\Omega = 10\,\mathrm{rad/s}$).

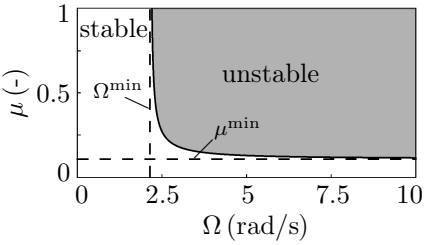

(b) Stability boundary in the Ω-μ-plane; dashed lines: critical values, ($n_0 = 0.1\,\mathrm{N/rad}$).

Figure 3.12: Stability map of the wobbling disk generator: Perturbation of the friction coefficient over the excitation parameter n_0 and Ω ($\alpha = 1.05$).

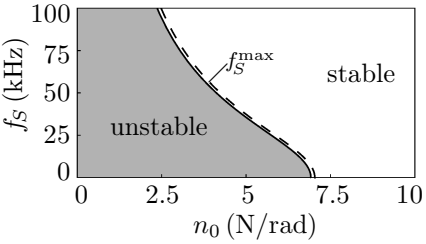

(a) Stability boundary in the n_0-f_S-plane; dashed line: $f_S^{\max}$.

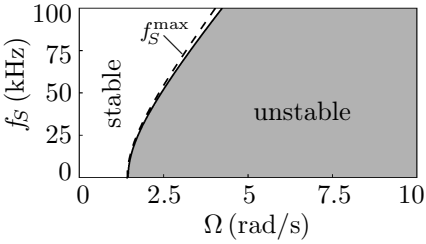

(b) Stability boundary in the Ω-f_S-plane; dashed line: $f_S^{\max}$.

Figure 3.13: Stability map of the wobbling disk generator: natural frequency f_0 of the wobbling disk over the excitation parameter n_0 and Ω.

friction. Therefore, f_S depends only on the geometry and material properties of the stator and the shaft,

$$f_S = \frac{1}{2\pi}\frac{1+\alpha}{2}\frac{k_S}{\Theta_S}. \tag{3.81}$$

The Eqs. (3.75) and (3.78) lead to the conservative upper boundary $f_S^{\max}$, which is in good agreement with the exact stability boundary, shown in Fig. 3.13. Through an increase of the natural frequency of the stator, the instability region decreases and makes it more difficult to initiate self-excitation.

Nevertheless, this drawback is less significant in the lower ultrasonic range of f_S. Although the derived approximations of the stability boundary (3.77)-

Table 3.2: Parameters of the wobbling disk generator.

	parameter	symbol	value	unit
rotor	mass	m_R	$1 \cdot 10^{-3}$	kg
	radius	r_R	$5 \cdot 10^{-3}$	m
	stiffness coefficient	k_R	100	N/m
	damping coefficient	d_R	10^{-4}	Ns/m
	pre-stress force	n_0	0.1	N/rad
	rotation speed	Ω_w	10	rad/s
friction-layer	friction coefficient	μ	0.4	–
	stiffness coefficient	k_f	$1.6 \cdot 10^7$	N/mrad
	damping coefficient	d_f	10^{-6}	Ns/mrad
stator	mass	m_S	$2 \cdot 10^{-3}$	kg
	height	h	$3 \cdot 10^{-3}$	m
	radius	r	$5 \cdot 10^{-3}$	m
shaft	torsional stiffness	k_t	10^4	Nm/rad
	damping coefficient	d_t	$4 \cdot 10^{-2}$	Nms/rad
	bending stiffness	k_S	$2.2 \cdot 10^3$	Nm/rad
	damping coefficient	d_S	10^{-4}	Nms/rad
piezoceramic	radius	r_P	$5 \cdot 10^{-3}$	m
	height	h_P	$2 \cdot 10^{-3}$	m
	YOUNG's modulus	E_P	$5.26 \cdot 10^{10}$	N/m^2
	damping coefficient	E_P^d	90	Ns/m^2
	piezoelectric constant	d_{33}	$4.5 \cdot 10^{-10}$	m/V
	permittivity	ε_{33}	$1.137 \cdot 10^{-8}$	F/m
	coupling factor	$\gamma = d_{33}\, E_P$	23.68	N/Vm
	effective permittivity	$\nu = \varepsilon_{33} - d_{33}^2 E_P$	$7.2 \cdot 10^{-10}$	F/m

(3.80) are somewhat rough, they give an insight into which parameters have the main influence, providing useful design criteria for energy harvesting applications exploiting self-excitation mechanism.

Parameter optimization

In section 2.1.2, the region of flutter-type instability is maximized by minimizing the absolute difference between the two critical imaginary parts of the eigenvalues of the linearized system. Using the general expression for the imaginary parts (2.22) the optimization problem reads

$$\min J = \min\left(\omega_2^2 - \omega_1^2\right) = \min\left(b^2 + \Delta k^2 - n^2\right). \tag{3.82}$$

Inserting the expressions for the rotor-fixed friction layer (Tab. 3.1) yields

$$\min J = \min\left[n_0^2 + \left(\frac{(1-\alpha)k_S}{2\mu\pi r}\right)^2 - \left(\frac{h}{2}k_f\right)^2\right]. \tag{3.83}$$

Obviously, the cost function J reaches its minimum with respect to α for symmetric stiffness properties ($\alpha = 1$), which was already observed in Fig. 3.11.

Piezoelectric coupling

In the following, the influence of the piezoceramic on the stability behavior of the stator, which was neglected in the previous discussion, is analyzed. Therefore, the coupled linear equations of motion of the stator (3.56) and of the piezoceramic (3.57) are considered together with the electric circuit equations of the electrodes (3.61). In Fig. 3.14 the imaginary and real parts of the eigenvalues of the decoupled system are compared to the ones of the coupled system. Only the critical eigenvalues of the stator are displayed, since the piezoceramic and the electric circuit cannot be destabilized. Basically, two main effects concerning the dynamics of the stator, which result from the connection to the piezoceramic, have to be pointed out. The first one is the lower overall stiffness of the stator, resulting from the changed boundary conditions of the shaft. Instead of being inertially fixed, the lower end of the shaft

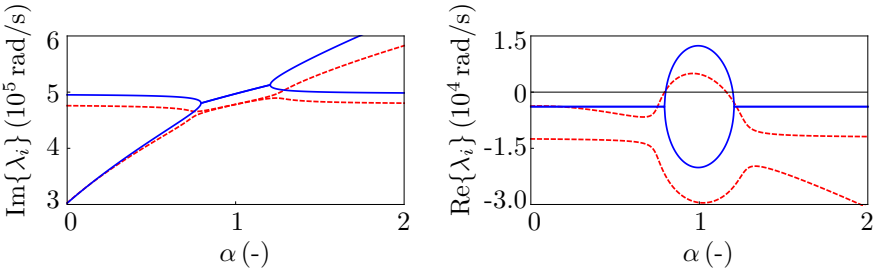

(a) Imaginary part of the critical eigenvalues.

(b) Real part of the critical eigenvalues.

Figure 3.14: Bifurcation diagram of the critical eigenvalues of the wobbling disk generator: Comparison of the cases with decoupled (solid line) and coupled (dashed line) piezoceramic.

is connected to an elastic piezoceramic structure. Thereby, the eigenfrequencies of the system, represented by the imaginary parts of the eigenvalues, are lower (Fig. 3.14a). The second effect is the increase of the overall damping of the structure, which is mainly caused by the electric resistances R_j connected to the electrodes, leading to lower instability regions. This effect is shown in Fig. 3.14b, where the real parts as well as the region with $\mathrm{Re}\{\lambda_i\} > 0$ decrease. How strong the piezoceramic affects the dynamics of the stator depends on the mechanical properties of the connecting shaft.

3.2.2 Finite element analysis

In this section, the wobbling disk generator is studied with respect to the initiation of self-excited vibrations by using the finite element method (FEM). In comparison to analytical analysis methods, the FEM has the advantage that it can handle structures of a much higher complexity. Nevertheless, the disadvantage of FEM is that on the one hand, the numerical simulation can be very time consuming and on the other hand, the influence of characteristic system parameters is difficult to deduce.

Finite element model

The finite element model of the wobbling disk generator (inverted CANON bar-type ultrasonic motor U400), shown in Fig. 1.2b, was built up using the commercial software ABAQUS. Figure 3.15 shows a finite element model of the stator with geometrical asymmetries (simplified mesh for vizualization).

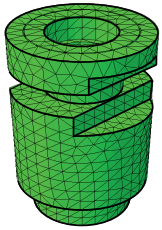

Figure 3.15: Finite element model of a wobbling disk generator (stator).

The model, shown in Fig. 3.15, is inertially fixed at the bottom. The rotor (not shown) is pressed against the stator and has a constant rotation speed Ω around the vertical axis. In addition, the friction effect in the contact zone between the stator and the rotor is taken into account. For the calculation $4{\cdot}10^4$ DOF and tetrahedral elements are used.

Stability analysis using ABAQUS

The objective is to analyze the stability behavior of the stator-rotor system, in order to verify the analytical results from the previous section. To this end, the so-called *Complex Eigenvalue Analysis* (CEA) is used. The procedure is based on solving the eigenvalue problem of the form

$$\left(\lambda^2\mathbf{M} + \lambda(\mathbf{D}_s + \mathbf{D}_f) + \mathbf{K} + \mathbf{N}\right)\mathbf{v} = \mathbf{0}, \tag{3.84}$$

where λ are the eigenvalues and $\mathbf{v}$ are the corresponding eigenvectors of the system. The matrices $\mathbf{M}$ and $\mathbf{K}$ are the mass and stiffness matrix of the structure, which depend on geometry and material properties of the structure. The system damping is considered in the analysis through $\mathbf{D}_s$, which is usually modeled as RAYLEIGH damping,

$$\mathbf{D}_s = \alpha\,\mathbf{M} + \beta\,\mathbf{K}, \tag{3.85}$$

where α and β are the mass and stiffness-proportional damping coefficients. The damping matrix $\mathbf{D}_f$ results from linearization of non-conservative terms around the steady state, which originate from the friction contact. In addition, these non-conservative terms also lead to the circulatory matrix $\mathbf{N}$. It should be pointed out, that the CEA is only appropriate for autonomous systems, which means that the coefficients of the matrices should be constant in time. This is the case for the wobbling disk generator, since the contact zone is distributed over the whole circumference.

For example, in the analysis of automotive disk brakes with an asymmetric disk, the system matrices have non-negligible periodic terms and therefore the CEA is not suitable for the stability analysis [52]. The gyroscopic matrix is not considered due to a marginal effect on the behavior of the system.

Table 3.3: Material parameters of the finite element model.

parameter	symbol	value	unit
mass density	ρ	8500	$\mathrm{kg/m^3}$
YOUNG's modulus	E	$0.9{\cdot}10^{11}$	$\mathrm{N/m^2}$
POISSON's ratio	ν	0.37	–
mass-proportional damping	α	0	1/s
siffness-proportional damping	β	10^{-6}	s
friction coefficient	μ	0.4	–

The parameter set used for the stability analysis is summarized in Tab. 3.3. The results obtained through CEA are displayed in Fig. 3.16, where different critical parameters, such as the rotation speed of the rotor $f_R = \Omega/2\pi$, the pre-stress through s_0 and the friction coefficient μ were varied. In the graphs, only the real part of the critical eigenvalue is plotted. The stability boundary in Fig. 3.16a, represented by $\mathrm{Re}\{\lambda_i\} > 0$, moves to smaller μ by increasing f_R. This behavior is equivalent to the results obtained for the analytical model, shown in Fig. 3.12b. The stabilizing effect through an increase of the pre-stress is shown in Fig. 3.16b, which agrees with the derived approximation of the

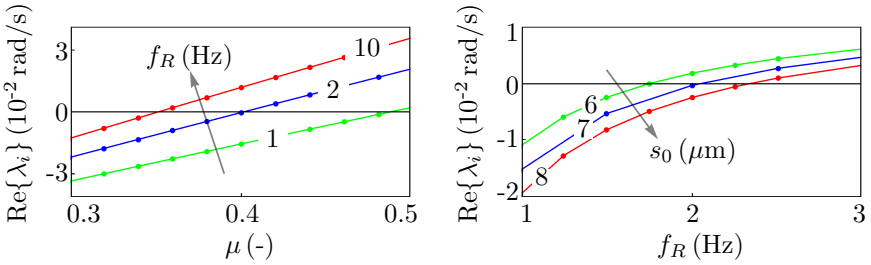

(a) Real part of the eigenvalues for different rotation speed f_R.

(b) Real part of the eigenvalues for different pre-stress s_0.

Figure 3.16: Results from the CEA (Complex Eigenvalue Analysis, ABAQUS) for the wobbling disk generator: Real part of the critical eigenvalue.

stability boundary for Ω in Eq. (3.78). The corresponding mode shape, which becomes unstable, is shown in Fig. 3.17a and 3.17b. A combination of the two orthogonal mode shapes $(1,0)_\mathrm{s}$ and $(1,0)_\mathrm{c}$ represent the wobbling-type motion of the stator. Of course, the finite element model consists of much more degrees of freedom, describing other mode shapes of the structure, for example the $(2,0)$-mode, shown in Fig. 3.17c and 3.17d. Through the geometry of the stator all the other mode shapes are shifted to higher natural frequencies. However, only the unstable behavior of the $(1,0)$-mode can be observed. This observation justifies the modeling approach considering only the wobbling motion of the stator.

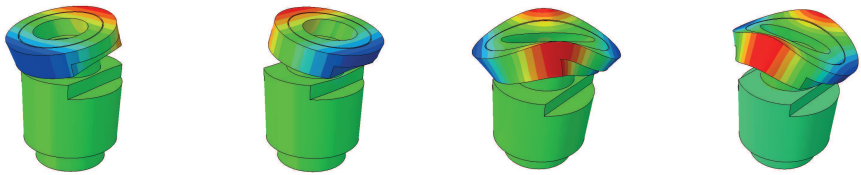

(a) $(1,0)_\mathrm{s}$-mode **(b)** $(1,0)_\mathrm{c}$-mode **(c)** $(2,0)_\mathrm{s}$-mode **(d)** $(2,0)_\mathrm{c}$-mode

Figure 3.17: Numerical modal analysis of the stator part: $(1,0)$-mode (23.0 kHz and 23.8 kHz) and $(2,0)$-mode (57.9 kHz and 59.7 kHz).

In Fig. 3.18 the stress distribution in the piezoceramic is shown for the $(1,0)$ and $(2,0)$-modes. The knowledge of this stress distribution is essential for the design of the electrode configuration. For the wobbling disk generator, in which the $(1,0)$-mode gets self-excited, the optimum electrode configuration is illustrated in Fig. 3.6b.

(a) $(1,0)$-mode shape of the stator. **(b)** $(2,0)$-mode shape of the stator.

Figure 3.18: Stress distribution of the piezoceramic for different mode shapes.

3.3 Bifurcation and steady-state operation

In this section, the steady-state behavior of the wobbling disk generator is analyzed based on analytical as well as numerical methods. In contrast to the previous section, where the initiation of self-excited vibrations was analyzed by the stability analysis of the linearized system, here, the nonlinear equations of motion are required. By the analysis of these nonlinear equations of motion, the type of the bifurcation as well as the characteristics of the resulting limit-cycle oscillations can be determined. In the first steps, the piezoceramic structure is neglected, allowing a better understanding of the steady-state behavior of the stator. Afterwards, the influence of the piezoceramic on the steady-state operation is discussed, as well as the characteristic performance regarding the electric power output of the wobbling disk generator.

In the case of steady-state motion, the assumption of sliding in the whole contact zone can be violated. Clearly, this assumption is valid for the system linearized around the trivial solution, as it was the case in the analysis of the initiation of self-excited vibrations in section 3.2. In the steady-state operation, the following contact phenomena have to be considered: On the

one hand, partial separations in the contact zone can occur and on the other hand, besides the sliding zones also stiction zones are possible. The aim of this section is not to derive a general steady-state characteristics of the wobbling disk generator by taking all these phenomena into account, but to give a good estimate of the steady-state operation by using appropriate assumptions. To this end, two different assumptions for the steady-state motion are considered, namely sliding in the whole contact zone and adhesive contact kinematics. A more detailed modeling of the stator-rotor contact of ultrasonic motors can be found in [45, 47, 48].

3.3.1 Representation of the wobbling motion

First of all, the characteristic motion of the stator, which dominates the steady-state behavior of the generator, is considered. This motion results from a combination of the two bending modes about the $\vec{n}_1$ and $\vec{n}_2$-axis (Fig. 3.1) and is represented in the following in different reference frames and for different generalized coordinates. The wobbling motion of a rigid body (amplitude $\hat{q}$, wobbling frequency Ω_w) is represented in the inertial reference frame $\mathcal{N}$ by the angular velocity

$$ {}^{\mathcal{N}}\vec{\omega}^{S} = \omega_1 \, \vec{n}_1 + \omega_2 \, \vec{n}_2 + \omega_3 \, \vec{n}_3, \tag{3.86} $$

with the components

$$ \omega_1 = \hat{q} \, \Omega_w \cos \Omega_w t, \qquad \omega_2 = \hat{q} \, \Omega_w \sin \Omega_w t, \qquad \omega_3 = 0. \tag{3.87} $$

The kinematic relations between the EULER angles q_{E_i} (used in section 3.3.3) and the components of the angular velocity in the inertial frame $\mathcal{N}$ are

$$ \dot{q}_{E_1} = \omega_3 - \frac{\sin q_{E_1} \, \omega_1 + \cos q_{E_1} \, \omega_2}{\tan q_{E_2}}, \tag{3.88} $$

$$ \dot{q}_{E_2} = \sin q_{E_1} \, \omega_2 + \cos q_{E_1} \, \omega_1, \tag{3.89} $$

$$ \dot{q}_{E_3} = \frac{\sin q_{E_1} \, \omega_1 - \cos q_{E_1} \, \omega_2}{\sin q_{E_2}}. \tag{3.90} $$

Inserting the expression for the wobbling motion (3.87) into the kinematic relations (3.88)-(3.90) yields

$$\dot{q}_{E_1} = \Omega_w, \qquad \dot{q}_{E_2} = 0, \qquad \dot{q}_{E_3} = -\frac{\Omega_w}{\cos q_{E_2}}. \tag{3.91}$$

Thus, the exact solution for the EULER angles reads

$$q_{E_1} = \Omega_w t, \qquad q_{E_2} = \hat{q}, \qquad q_{E_3} = \beta - \frac{\Omega_w t}{\cos \hat{q}}, \tag{3.92}$$

where the angles q_{E_1} and q_{E_3} increase linearly with time and the nutation angle q_{E_2}, represented by $\hat{q}$, is constant.

The kinematic relations between the CARDAN angles q_{C_i} (used in section 3.3.2) and the components of the angular velocity in the inertial frame $\mathcal{N}$ are

$$\dot{q}_{C_1} = \omega_1 + \tan q_{C_2} \left(\sin q_{C_1}\omega_2 - \cos q_{C_1}\omega_3\right), \tag{3.93}$$

$$\dot{q}_{C_3} = \frac{\cos q_{C_1}\omega_3 - \sin q_{C_1}\omega_2}{\cos q_{C_2}}, \tag{3.94}$$

$$\dot{q}_{C_2} = \cos q_{C_1}\omega_2 + \sin q_{C_1}\omega_3. \tag{3.95}$$

Inserting the expression for the wobbling motion (3.87) into the kinematic relations (3.93)-(3.95) leads to a set of time-variant differential equations, which solution can not be given explicitly, as was the case for the EULER angles (3.91). However, assuming that the amplitude of the wobbling motion $\hat{q}$ is small, an approximation can be given by linearization around the trivial solution

$$\dot{q}_{C_1} \approx \omega_1, \qquad \dot{q}_{C_2} \approx \omega_2, \qquad \dot{q}_{C_3} \approx \omega_3. \tag{3.96}$$

Subsequently, the approximations for the CARDAN angles are

$$q_{C_1} \approx \hat{q} \sin \Omega_w t, \qquad q_{C_2} \approx -\hat{q} \cos \Omega_w t, \qquad q_{C_3} \approx 0. \tag{3.97}$$

The expressions (3.92) and (3.97) can be used to identify whether the resulting steady-state solution, which is expressed by EULER or CARDAN angles respectively, is a wobbling motion or not.

3.3.2 Sliding in the contact zone

In the following, the steady-state behavior of the wobbling disk is analyzed using the nonlinear equations of motion of the stator (3.1). First of all, the effect of the piezoceramic is neglected by setting $\vec{M}_{P_i} = \vec{0}$. A further assumption is that the contact line corresponds to the whole circumference. Using the parameter set given in Tab. 3.2 and CARDAN angles as generalized coordinates, the numerical solution of the nonlinear equations of motion, shown in Fig. 3.19, is obtained. The input parameters n_0 and Ω are chosen in such

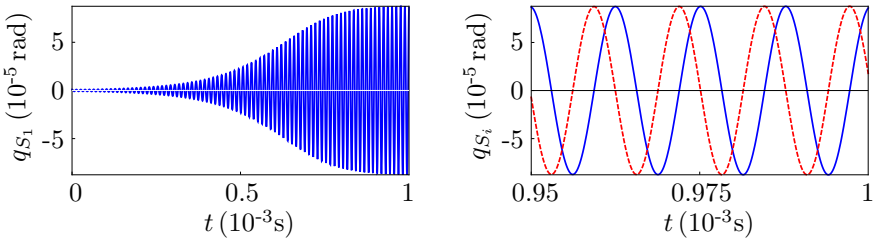

(a) CARDAN angle $q_{S_1}(t)$: stable limit-cycle oscillations.

(b) CARDAN angles; solid line: $q_{S_1}(t)$, dashed line: $q_{S_2}(t)$.

Figure 3.19: Numerical solution of the nonlinear equations of motion (3.1): initiation of self-excited oscillations ($\alpha = 1$, $n_0 = 0.1$ N/rad, $\Omega = 10$ rad/s).

a way that self-excited oscillations occur. Figure 3.19a shows the transient behavior of q_{S_1}. It can be observed how the trivial solution becomes unstable, leading to stable limit-cycle oscillations for the steady state. The steady-state solution for the CARDAN angles q_{S_1} and q_{S_2} have substantially the form of time-shifted harmonic functions with a relatively small amplitude and a high frequency (Fig. 3.19b).

A suitable analytical approach to analyze the limit-cycle characteristics is the harmonic balance method, described for example in [13, 35]. The procedure of this method is to insert a FOURIER series *ansatz* for the coordinates into the equations of motion. Collecting the coefficients of harmonic functions with same basis frequency leads to a set of algebraic equations. Solving this set of equations for the unknown parameters gives an approximation for the limit-

cycle characteristics. The numerical simulation of the nonlinear equations of motion indicates that a promising *ansatz* for the generalized coordinates is

$$q^*_{S_1} = \hat{q}\,\cos\Omega_w t, \qquad q^*_{S_2} = \hat{q}\,(\beta_s\,\sin\Omega_w t + \beta_c\,\cos\Omega_w t), \tag{3.98}$$

where $\hat{q}$ is the amplitude and $\Omega_w = 2\pi f_w$ is the frequency of the wobbling motion. Inserting into the equations of motion of the stator (3.1) and neglecting the coordinate q_{S_3}, four algebraic equations for the unknown parameters $\hat{q}$, Ω_w, β_c and β_s are obtained. Using symmetric stiffness properties for the shaft ($\alpha = 1$) yields

$$\beta_s = -1, \qquad \beta_c = 0. \tag{3.99}$$

The solution for $\hat{q}$ and f_w is displayed in Fig. 3.20 in a range for the rotation speed Ω, where a bifurcation of the solution occurs. In the region, where the

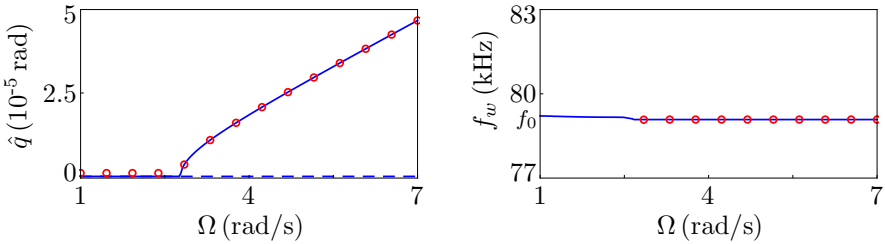

(a) Limit-cycle amplitude $\hat{q}$. **(b)** Limit-cycle frequency f_w.

Figure 3.20: Limit-cycle characteristics obtained from *harmonic balance* method (solid line) compared to numerical simulation (circles) ($n_0 = 1$ N/rad).

trivial solution is unstable, denoted by a dashed line in Fig. 3.20a, also a stable periodic solution with the amplitude $\hat{q}$ exists. The frequency of this periodic solution is plotted in Fig. 3.20b over the rotation speed of the rotor. While the amplitude $\hat{q}$ increases linearly in the region of self-excitation, the wobbling frequency f_w remains constant. A validation of these analytic results is done by comparing the limit-cycle characteristics to numerical simulation of the equations of motion (circles in Fig. 3.20). It can be observed that the analytical results obtained from the *ansatz* (3.98) are in good agreement with

numerical simulation. A further observation is that the wobbling frequency corresponds very precisely to the natural frequency of the linearized system, given in Eq. (3.75), ($f_w \approx f_0 = \omega_0/2\pi$). This property is very important for vibration-based energy harvesting applications since the operation frequency is decoupled from the excitation frequency and thereby allows a broad-band applicability. Moreover, the natural frequency can be set by design independently from any excitation parameters, in order to maximize the efficiency[10].

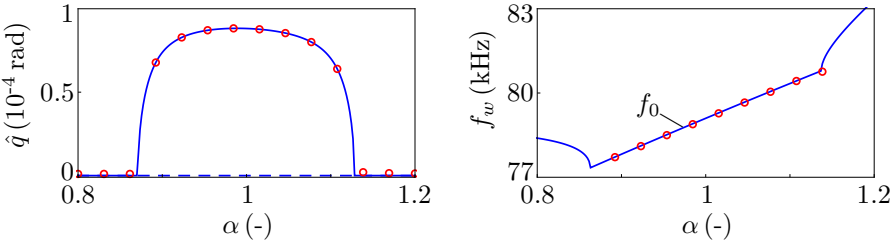

(a) Limit-cycle amplitude $\hat{q}$. **(b)** Limit-cycle frequency f_w.

Figure 3.21: Limit-cycle characteristics obtained from *harmonic balance* (solid line) compared to numerical simulation (circles) ($n_0 = 0.1$ N/rad, $\Omega = 10$ rad/s).

Another property of the resulting limit cycle is the robustness of the amplitude $\hat{q}$ against perturbations of the stiffness symmetry of the shaft, shown in Fig. 3.21. Introducing asymmetry by setting $\alpha \neq 1$, the amplitude $\hat{q}$, shown in Fig. 3.21a, scarcely decreases, even for relatively large perturbations of about $\alpha = 1 \pm 0.2$. The wobbling frequency, plotted in Fig. 3.21b, changes accordingly to the stiffness properties of the shaft through a variation of α. Similarly to the results given in Fig. 3.20, the analytical results for the limit-cycle characteristics in Fig. 3.21 are in excellent agreement with the numerical simulation. Furthermore, the wobbling frequency f_w corresponds to the frequency of the linearized system f_0 as it was the case for a symmetric configuration.

[10] Here, the efficiency is defined as the ratio between the electrical power output and the mechanical power input.

Piezoelectric coupling and power transmission characteristic

The effect of the piezoceramic, which was neglected in the previous analysis, is considered in this section. Besides the influence of the electric resistances at the electrode output R_j, also the effect of the stiffness coefficient of the shaft k_S is discussed in the following. In the analysis, a symmetric configuration of the shaft ($\alpha = 1$), as well as equal resistances at each electrode ($R_j = R$) are assumed.

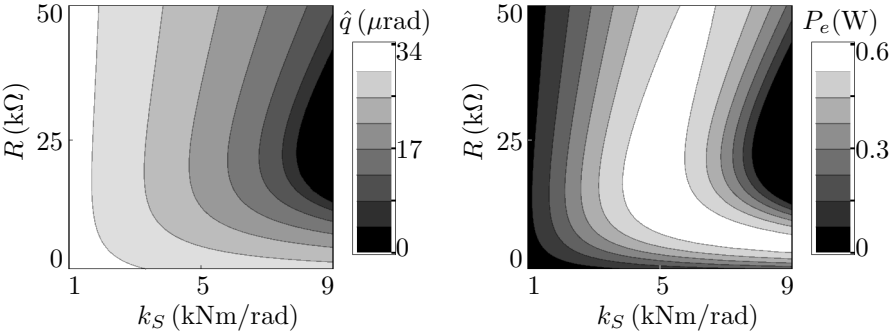

(a) Limit-cycle amplitude $\hat{q}$. **(b)** Electrical power output P_e.

Figure 3.22: Characteristic map for the wobbling disk generator with piezoceramic attached: Variation of k_S and R (sliding in the contact zone).

In Fig. 3.22 the amplitude of the wobbling motion $\hat{q}$ and the electric power output P_e for each electric load are varied over the resistance R and the stiffness k_S. An increase of k_S leads to a decrease of the amplitude $\hat{q}$ up to a complete disappearance limit-cycle oscillations (Fig. 3.22a). Regarding the electric power output, an optimum configuration of R and k_S exists, for which P_e reaches its maximum. This maximum is denoted as a white region in Fig. 3.22b. For a given shaft stiffness k_S the optimum resistance R^*, which leads to the maximum power output $P_e^{\max}$, can be computed. In Fig. 3.23a the maximum power output is compared to the estimate (3.68), where the feedback effect of the piezoceramic is not considered. Through a larger stiffness of the shaft the feedback effect from the piezoceramic to the

stator becomes stronger and has to be taken into account. However, a further increase of the stiffness leads to saturation of the maximum power output without any additional increase. The corresponding optimum resistance R^* is compared in Fig. 3.23b to its estimate (3.67). Similarly to the comparison of the estimated to the exact maximum power output, the estimation of R^* is in good agreement for relatively small k_S. For larger k_S, the deviation increases significantly and the assumption of negligible feedback effect is not justified anymore.

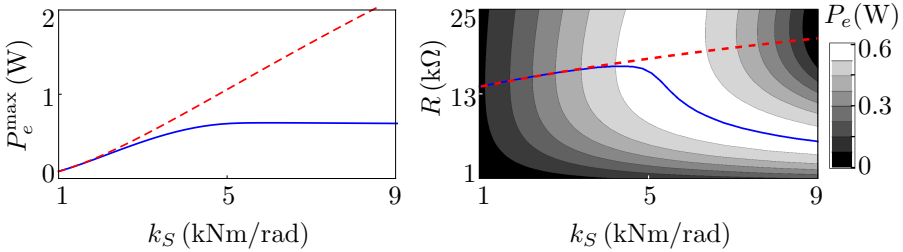

(a) Maximal electric power output. **(b)** Optimal electric resistance R^*.

Figure 3.23: Comparison of the optimal resistance R^* and maximal power output P_e^* with (solid line) and without (dashed line) feedback effect.

From the result given in Fig. 3.23, the following conclusions can be drawn: On the one hand, the estimates for the maximum power output and the corresponding optimal resistance are inadequate for larger k_S, but on the other hand, larger k_S leads to no further increase of the maximum power output. Moreover, regarding the initiation of self-excited vibrations, an increase of k_S also reduces the instability region, see section 3.2. Consequently, the stiffness of the shaft has to be optimized in the region before saturation. Thereby, the electric power output as well as the initiation of self-excited oscillations have to be considered. Since, in the region before saturation the feedback effect is negligible, the simplified derivation of critical parameters describing the stability boundary (3.77)-(3.80) as well as the simplified relation for the optimum resistance (3.67) provide good approximations. The influence of the stiffness of the friction layer k_f on the optimum resistance and the maximum

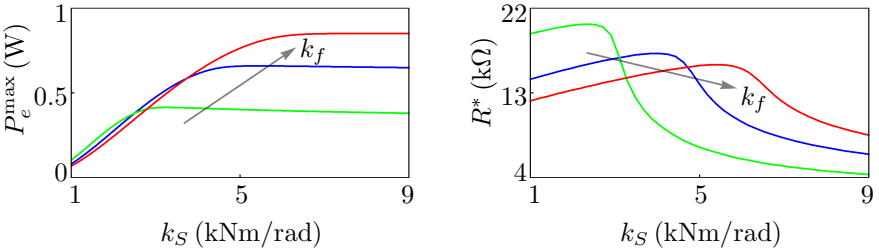

(a) Maximum power output $P_e^{\max}$. **(b)** Optimum resistance R^*.

Figure 3.24: Maximum power output and optimum electric resistance: Variation of the stiffness of the friction layer k_f.

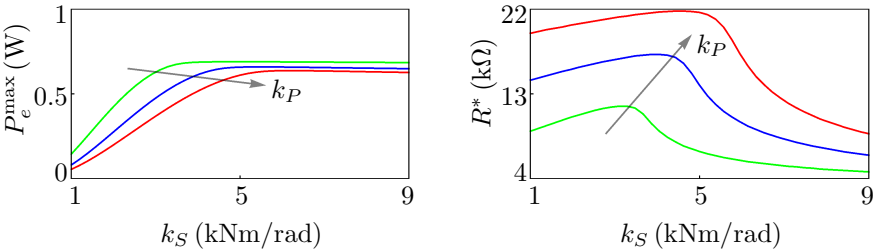

(a) Maximum power output $P_e^{\max}$. **(b)** Optimum resistance R^*.

Figure 3.25: Maximum power output and optimum electric resistance: Variation of the stiffness of the piezoceramic k_P.

power output is illustrated in Fig. 3.24. While for relatively small k_S, where the feedback effect is negligible, R^* decreases, the maximum power output remains unaffected. However, if k_f is increased the maximum power output goes into saturation for larger k_S and therefore reaches higher values. In the case of variation of the piezoceramic stiffness k_P, shown in Fig. 3.25, R^* increases with k_P, but $P_e^{\max}$ decreases. Regarding the electric power output, the stiffness of the piezoceramic should be as small as possible.

Influence of the dynamics of the rotor

The equation of motion for the rotor in the $\vec{e}_{R_3}$-direction reads

$$m_R\,\ddot{q}_R + d_R\,\dot{q}_R + k_R\,q_R = F_{\mathrm{Pin}} - N_0, \quad F_{\mathrm{Pin}} = \int_{\phi_1}^{\phi_2} \vec{f}_{Pin} \cdot \vec{e}_{R_3}\,\mathrm{d}\phi. \tag{3.100}$$

The mass of the rotor is m_R and the stiffness and damping coefficient are k_R and d_R. The forces on the right-hand side of the equation are the constant pre-stress force N_0 and the force resulting from the friction layer F_{Pin}. Using CARDAN angles as generalized coordinates to describe the motion of the stator, the expression for the distributed pin force reads

$$\vec{f}_{\mathrm{Pin}} \cdot \vec{e}_{R_3} = f_0 - f_c\,\cos\phi - f_s\,\sin\phi, \quad \text{with} \tag{3.101}$$

$$f_0 = k_f\left[\frac{h}{2}\left(\frac{1}{c_1 c_2} - 1\right) - q_R\right] + d_f\left[\frac{h}{2}\frac{\dot{q}_{S_1} t_1 + \dot{q}_{S_2} t_2}{c_1 c_2} - \dot{q}_R\right] \tag{3.102}$$

$$f_c = r\left(k_f\,t_1 + d_f\,\frac{\dot{q}_{S_1}}{c_1^2}\right), \quad f_s = \frac{r}{c_1}\left[k_f\,t_2 + d_f\left(\frac{\dot{q}_{S_2}}{c_2^2} + \dot{q}_{S_1} s_1 t_2\right)\right], \tag{3.103}$$

where the symbols s_i, c_i and t_i denote $\sin q_{S_i}, \cos q_{S_i}$ and $\tan q_{S_i}$ $(i = 1, 2, 3)$, respectively. If the contact zone corresponds to the full circumference of 2π, the terms f_c and f_s vanish after integration and the force resulting from the friction layer reduces to

$$F_{\mathrm{Pin}} = 2\pi\,f_0. \tag{3.104}$$

Carrying out the TAYLOR series up to the 2nd order for F_{Pin} yields

$$\begin{aligned} F_{\mathrm{Pin}} = -2\pi\,(k_f\,q_R + d_f\,\dot{q}_R) + \pi\frac{h}{2}k_f(q_{S_1}^2 + q_{S_2}^2) \\ + \pi h d_f(q_{S_1}\dot{q}_{S_1} + q_{S_2}\dot{q}_{S_2}) + \mathcal{O}(q_i^4). \end{aligned} \tag{3.105}$$

Inserting this expression together with the *ansatz* for the wobbling motion (3.98) into the equation of motion (3.100) leads to the constant steady-state displacement

$$q_R^* = \frac{-F_0}{k_R + 2\pi k_f} + \frac{\pi\frac{h}{2}k_f\,\hat{q}^2}{k_R + 2\pi k_f} + \mathcal{O}(q_i^4). \tag{3.106}$$

On the one hand, the rotor moves in the direction of the stator due to the pre-stress force F_0, but on the other hand it moves in the opposite direction due to the wobbling motion of the stator. Since the influence of the wobbling motion amplitude is quadratic, the latter effect can be neglected and the assumption of a constant displacement is justified.

Influence of the torsional degree of freedom of the stator

The equation of motion for the CARDAN angle q_{S_3}, representing the torsional motion[11] of the stator, read

$$\begin{aligned}\Theta_3\ddot{q}_{S_3} + d_t\dot{q}_{S_3} + k_t q_{S_3} = &- k_S q_{S_1} q_{S_2} - d_S q_{S_2}\dot{q}_{S_1} \\ &- \Theta_3(q_{S_2}\ddot{q}_{S_1} + \dot{q}_{S_1}\dot{q}_{S_2}) + \vec{M}_f \cdot {}^{\mathcal{N}}\vec{\omega}_3^S.\end{aligned} \tag{3.107}$$

Inserting the *ansatz* for the wobbling motion (3.97) and carrying out the TAYLOR series up to the 2nd order over the trivial solution yields for the constant steady-state displacement

$$q_{S_3}^* = \mu r\left(\frac{2\pi n_0}{k_t} + \hat{q}^2\pi\frac{hk_f + n_0}{k_t}\right)\frac{\Omega}{\sqrt{\Omega}} + \mathcal{O}(\hat{q}_i^4). \tag{3.108}$$

The magnitude of the displacement increases with the pre-stress n_0 and the amplitude of the wobbling motion $\hat{q}$. Depending on the direction of the rotation speed Ω, the displacement changes the direction. Basically, the torsional degree of freedom has a negligible effect only.

The main assumption for the previously discussed steady-state operation was sliding in the complete contact zone. Since in some cases this assumption is violated, for example due to separation, another contact kinematics is analyzed in the following, namely the assumption of an adhesive contact.

3.3.3 Adhesive contact

The equations of motion for the stator are rewritten as

$$\left[\vec{M}_S - \frac{{}^{\mathcal{N}}\mathrm{d}}{\mathrm{dt}}\left(\boldsymbol{\Theta}^{S/S_o}\,{}^{\mathcal{N}}\vec{\omega}^S\right)\right]\cdot{}^{\mathcal{N}}\vec{\omega}_i^S - \vec{F}_C \cdot {}^{\mathcal{N}}\vec{v}_i^{S_C} = 0, \qquad i = 1,2,3, \tag{3.109}$$

[11] In the linearized case it is equivalent to the rotational motion around the $\vec{n}_3$-axis.

and for the rotor as

$$\begin{aligned} m_R\,\ddot{q}_R + d_R\,\dot{q}_R + k_R\,q_R &= \vec{F}_C \cdot {}^{\mathcal{N}}\vec{v}_1^{R_C} - N_0, \\ \Theta_R\,\dot{\Omega} &= \vec{F}_C \cdot {}^{\mathcal{N}}\vec{v}_2^{R_C} + M_R. \end{aligned} \tag{3.110}$$

The internal contact force $\vec{F}_C$ is used instead of the torque resulting from the friction layer. The partial velocities of the contact point S_C are given by ${}^{\mathcal{N}}\vec{v}_i^{S_C}$. Using the EULER-313 description the rotation matrix of the stator with respect to the inertial frame $\mathcal{N}$ results from three simple rotations

$$\begin{bmatrix}\vec{n}_1 & \vec{n}_2 & \vec{n}_3\end{bmatrix}^{\mathrm{T}} = {}^{\mathcal{N}}\mathbf{R}^{\mathcal{A}}\,{}^{\mathcal{A}}\mathbf{R}^{\mathcal{B}}\,{}^{\mathcal{B}}\mathbf{R}^{S}\begin{bmatrix}\vec{e}_{S_1} & \vec{e}_{S_2} & \vec{e}_{S_3}\end{bmatrix}^{\mathrm{T}} = {}^{\mathcal{N}}\mathbf{R}^{S}\begin{bmatrix}\vec{e}_{S_1} & \vec{e}_{S_2} & \vec{e}_{S_3}\end{bmatrix}^{\mathrm{T}}, \tag{3.111}$$

$${}^{\mathcal{N}}\mathbf{R}^{S} = \begin{bmatrix} c_1 & -s_1 & 0 \\ s_1 & c_1 & 0 \\ 0 & 0 & 1 \end{bmatrix} \begin{bmatrix} 1 & 0 & 0 \\ 0 & c_2 & -s_2 \\ 0 & s_2 & c_2 \end{bmatrix} \begin{bmatrix} c_3 & -s_3 & 0 \\ s_3 & c_3 & 0 \\ 0 & 0 & 1 \end{bmatrix}, \tag{3.112}$$

$${}^{\mathcal{N}}\mathbf{R}^{S} = \begin{bmatrix} c_1c_3 - s_1c_2s_3 & -s_1c_2c_3 - c_1s_3 & s_1s_2 \\ s_1c_3 + c_1c_2s_3 & c_1c_2c_3 - s_1s_3 & -c_1s_2 \\ s_2s_3 & c_3s_2 & c_2 \end{bmatrix}, \tag{3.113}$$

where the symbols s_i and c_i denote $\sin q_{S_i}$ and $\cos q_{S_i}$ $(i = 1, 2, 3)$, respectively. A graphical representation of the EULER-123 rotation, which is equivalent to the rotation matrix (3.113) is given in [11, 24]. Using trivial kinematic differential equations $u_{S_i} = \dot{q}_{S_i}$ $(i = 1, 2, 3)$ leads, according to Eq. (3.3), to the partial angular velocities ${}^{\mathcal{N}}\vec{\omega}_i^{S}$

$$\begin{bmatrix}{}^{\mathcal{N}}\vec{\omega}_1^{S} & {}^{\mathcal{N}}\vec{\omega}_2^{S} & {}^{\mathcal{N}}\vec{\omega}_3^{S}\end{bmatrix} = \begin{bmatrix}\vec{n}_3 & \vec{a}_1 & \vec{b}_3\end{bmatrix}. \tag{3.114}$$

Using the direction vectors of the reference frame $\mathcal{B}$ the internal contact force $\vec{F}_C$ is expressed by

$$\vec{F}_C = F_N\,\vec{n}_3 + F_T\,\vec{b}_1. \tag{3.115}$$

Contact point kinematics

Using the Euler-313 representation the position vector of the contact point S_C is given by

$${}^{\mathcal{N}}\vec{p}^{\,S_C} = r_C\,\vec{a}_2 + h_C\,\vec{a}_3, \tag{3.116}$$

with the abbreviations

$$r_C = r\,\cos q_{S_2} - \frac{h}{2}\,\sin q_{S_2}, \qquad h_C = r\,\sin q_{S_2} + \frac{h}{2}\,\cos q_{S_2}. \tag{3.117}$$

The absolute velocity of the contact point S_C on the stator surface is

$${}^{\mathcal{N}}\vec{v}^{\,S_C} = {}^{\mathcal{N}}\vec{\omega}^{\,S} \times {}^{\mathcal{N}}\vec{p}^{\,S_C} := \sum_{i=1}^{3} u_{S_i}\,{}^{\mathcal{N}}\vec{v}_i^{\,S_C}, \tag{3.118}$$

and the absolute velocity of the corresponding contact point related to the rotor is

$${}^{\mathcal{N}}\vec{v}^{\,R_C} = {}^{\mathcal{N}}\vec{\omega}^{\,R} \times {}^{\mathcal{N}}\vec{p}^{\,S_C} + \dot{q}_R\,\vec{n}_3 := \dot{q}_R\,{}^{\mathcal{N}}\vec{v}_1^{\,R_C} + \Omega\,{}^{\mathcal{N}}\vec{v}_2^{\,R_C}, \tag{3.119}$$

where the angular velocity of the rotor is given by the rotation speed ${}^{\mathcal{N}}\vec{\omega}^{\,R} = \Omega\vec{n}_3$. Thus, for the partial velocities ${}^{\mathcal{N}}\vec{v}_i^{\,S_C}$ and ${}^{\mathcal{N}}\vec{v}_i^{\,R_C}$ follows

$$\left[{}^{\mathcal{N}}\vec{v}_1^{\,S_C} \quad {}^{\mathcal{N}}\vec{v}_2^{\,S_C} \quad {}^{\mathcal{N}}\vec{v}_3^{\,S_C}\right] = \left[-r_C\,\vec{b}_1 \quad r\,\vec{b}_3 - \tfrac{h}{2}\,\vec{b}_2 \quad -r\,\vec{b}_1\right], \tag{3.120}$$

$$\left[{}^{\mathcal{N}}\vec{v}_1^{\,R_C} \quad {}^{\mathcal{N}}\vec{v}_2^{\,R_C}\right] = \left[\vec{n}_3 \quad -r_C\,\vec{b}_1\right]. \tag{3.121}$$

The assumption of an adhesive contact implies the following non-holonomic constraints

$$\left({}^{\mathcal{N}}\vec{v}^{\,S_C} - {}^{\mathcal{N}}\vec{v}^{\,R_C}\right)\cdot\vec{n}_3 = 0, \qquad \left({}^{\mathcal{N}}\vec{v}^{\,S_C} - {}^{\mathcal{N}}\vec{v}^{\,R_C}\right)\cdot\vec{b}_1 = 0. \tag{3.122}$$

Thereby, the relative velocity between the contact points is set to zero, similarly to a stiction or rolling assumption, respectively. Inserting the expressions for the velocities of the contact points (3.118) and (3.119) into the given constraints (3.122) yields

$$r_C\,u_{S_2} - \dot{q}_R = 0, \qquad u_{S_1} + \frac{r}{r_C}\,u_{S_3} - \Omega = 0. \tag{3.123}$$

The visco-elastic bedding torque resulting from the deformation of the shaft ($\vec{M}_S$), which was given in a coordinates-free expression (3.17), is redefined as a function of the Euler angles

$$\vec{M}_S = -(k_S\,q_{S_2} + d_S\,u_{S_2})\vec{b}_1 - [k_t(q_{S_1} + q_{S_3}c_2) + d_t(u_{S_1} + u_{S_3}c_2)]\vec{n}_3. \tag{3.124}$$

In a first step, the deformation of the piezoelectric structure is neglected ($\vec{M}_{P_i} = \vec{0}$). By using the expressions for $\vec{M}_S$ and $\vec{F}_C$ the equations of motion for the stator (3.109) reduce to

$$\begin{aligned}
&\Theta_3\, c_2\, \dot{u}_{S_3} + \left(\Theta_S\, s_2^2 + \Theta_3\, c_2^2\right) \dot{u}_{S_1} + \left[2\, c_2(\Theta_S - \Theta_3) u_{S_1} - \Theta_3\, u_{S_3}\right] s_2 u_{S_2} \\
&\qquad + d_t\,(u_{S_1} + c_2\, u_{S_3}) + k_t\,(q_{S_1} + c_2\, q_{S_3}) = M_R, \\
&\Theta_S\, \dot{u}_{S_2} + s_2\,(\Theta_3\, u_{S_3} - c_2(\Theta_S - \Theta_3) u_{S_1})\, u_{S_1} \\
&\qquad + d_S\, u_{S_2} + k_S\, q_{S_2} = -r_C\, F_N, \\
&\Theta_3\, c_2\, \dot{u}_{S_1} + \Theta_3\, \dot{u}_{S_3} - s_2\, \Theta_3\, u_{S_1}\, u_{S_2} + d_S\, s_2^2\, u_{S_3} \\
&\qquad + d_t\, c_2\,(u_{S_1} + c_2\, u_{S_3}) + k_t\, c_2\,(q_{S_1} + c_2\, q_{S_3}) = \frac{r}{r_C}\, M_R,
\end{aligned} \tag{3.125}$$

and the equations of motion for the rotor (3.110) simplify to

$$\begin{aligned}
m_R\, \ddot{q}_R + d_R\, \dot{q}_R + k_R\, q_R &= F_N - N_0, \\
\Theta_R\, \dot{\Omega} &= -r_C\, F_T + M_R.
\end{aligned} \tag{3.126}$$

The internal contact forces F_N and F_T in the equations of motion are eliminated by using the kinematic constraints (3.123). Thereby, a system of ordinary differential equations with three independent coordinates is obtained.

Steady-state characteristics

The exact solution of the nonlinear equations of motion (3.125) corresponds to the wobbling motion in the Euler representation (3.91) and (3.92) ($q_{S_i}^* = q_{E_i}$). Inserting $q_{S_i}^*$ into the kinematic constraints (3.123) yields

$$\dot{q}_R^* = 0, \quad q_R^* = h_C^*, \quad \Omega = -\tan\hat{q}\, \frac{h_C^*}{r_C^*}\, \Omega_w, \tag{3.127}$$

with the abbreviations

$$r_C^* = r\cos\hat{q} - \frac{h}{2}\sin\hat{q}, \qquad h_C^* = r\sin\hat{q} + \frac{h}{2}\cos\hat{q}. \tag{3.128}$$

Analogously, by using Eq. (3.126) for the contact forces in the steady state follows

$$F_N^* = N_0 + k_R\, h_C^*, \qquad F_T^* = \frac{M_R}{r_C^*} \qquad (N_0 = 2\pi n_0 - k_R \frac{h}{2}), \tag{3.129}$$

which are constant over time for $\dot{\Omega} = 0$. Furthermore, the nonlinear equations of motion for the stator (3.125) simplify for the steady state to

$$k_t\,\beta\cos\hat{q} = M_R, \tag{3.130}$$

$$\Omega_w^2\,\cos\hat{q}\,\sin\hat{q}(\Theta_S + \Theta_3\,\tan^2\hat{q}) - k_S\,\hat{q} = r_C^*\,F_N^*, \tag{3.131}$$

$$-d_S\,\Omega_w\,r_C^*\,\tan\hat{q} = M_R\,h_C^*. \tag{3.132}$$

By solving this nonlinear algebraic set of equations for the unknown parameters β, $\hat{q}$ and Ω_w, the characteristics for the steady-state solution are obtained as functions of the system parameters and the external torque M_R. Using Eq. (3.131) for the wobbling frequency Ω_w follows

$$\Omega_w^2 = \frac{k_S\,\hat{q} + r_C^*\,F_N^*}{\cos\hat{q}\,\sin\hat{q}(\Theta_S + \Theta_3\,\tan^2\hat{q})}. \tag{3.133}$$

Since the nutation angle $\hat{q}$ is assumed to be small ($\hat{q} \approx 10^{-4}\,\text{rad}$, [11]), the wobbling frequency (3.133) can be linearized around $\hat{q} = 0$. Thereby, the expression simplifies to

$$\Omega_w^2 = \frac{2\pi\,r\,n_0}{\hat{q}\,\Theta_S} + \Omega_0^2 + \mathcal{O}(\hat{q}), \quad \text{with} \quad \Omega_0^2 = \frac{k_S + k_R\,r^2 - \pi h n_0}{\Theta_S}. \tag{3.134}$$

Similarly, for the relation between the rotation frequency Ω and the wobbling frequency Ω_w (3.127) follows after linearization

$$\Omega = -\frac{h}{2r}\,\hat{q}\,\Omega_w + \mathcal{O}(\hat{q}^2). \tag{3.135}$$

The steady-state characteristics (3.127)-(3.132) are evaluated for the parameter set given in Tab. 3.2 and compared to the approximations made by linearizing around $\hat{q} = 0$. In Fig. 3.26 the nutation angle $\hat{q}$ and the wobbling frequency Ω_w are plotted over the rotation speed of the rotor. The approximations denoted by dashed lines are in good agreement with the exact solution in a wide range of Ω. The frequency transformation shown in Fig. 3.26b is characterized by the region $\widetilde{\Omega}_\ell < \Omega < \widetilde{\Omega}_u$, where Ω_w is nearly independent of Ω. The estimates for the limits of this region are

$$\widetilde{\Omega}_\ell = \frac{\pi h n_0}{\Theta_S\,\Omega_0}, \qquad \widetilde{\Omega}_u = \Omega_0\frac{h}{2r}, \tag{3.136}$$

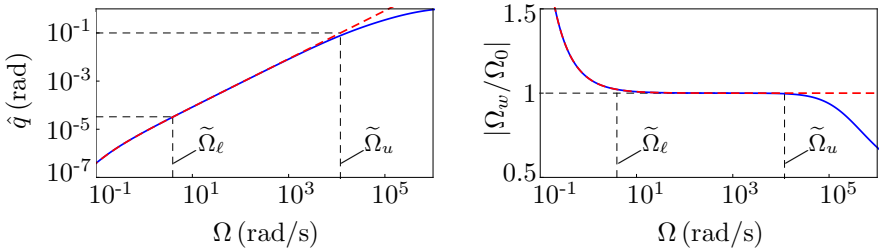

(a) Nutation angle $\hat{q}$ over Ω. **(b)** Wobbling frequency Ω_w over Ω.

Figure 3.26: Steady-state characteristics over the rotation frequency Ω: Comparison of exact (solid line) and linearized solution (dashed line).

and lead due to the high natural frequency ($\Omega_0/2\pi \approx 40\,\mathrm{kHz}$) to a wide operation range of about $0.3\,\mathrm{Hz} < \Omega/2\pi < 1\,\mathrm{kHz}$. In this region, the wobbling frequency Ω_w corresponds to the natural frequency Ω_0 (Eq. (3.134)) and the nutation angle $\hat{q}$ increases linearly with the rotation speed

$$\Omega_w \approx \Omega_0, \qquad \hat{q} \approx \frac{2r}{h}\,\frac{\Omega}{\Omega_0}. \tag{3.137}$$

This property of the wobbling frequency, namely the independence from the excitation, is of utmost importance for a broad-band energy harvesting application. Furthermore, the wobbling frequency depends only on the system parameter and therefore is defined by the design only. Such steady-state characteristic was already observed for the wobbling disk generator with the assumption of sliding in the contact zone, see Fig. 3.20.

Linearizing the Eqs. (3.132) and (3.129) around $\hat{q} = 0$, gives the following estimates for the torque M_R acting on the rotor and the contact-force ratio μ_0 as,

$$M_R = d_S\,\Omega_0\,\frac{2r}{h}\,\hat{q} + \mathcal{O}(\hat{q}^2), \quad \mu_0 := \frac{F_T^*}{F_N^*} = \frac{d_S\,\Omega_0\,\hat{q}}{\pi h n_0} + \mathcal{O}(\hat{q}^2). \tag{3.138}$$

In Fig. 3.27, the exact solutions for M_R and μ_0 are compared to the approximations obtained through linearization. Regarding the relevant excitation range, these approximations are in good agreement with the exact solutions.

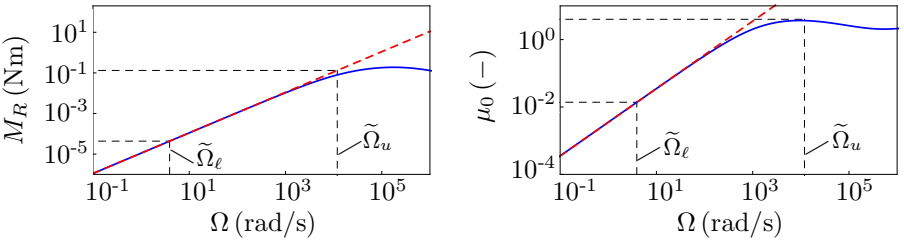

(a) Excitation torque M_R over Ω.

(b) Contact-force ratio μ_0 over Ω.

Figure 3.27: Steady-state characteristics over the rotation frequency Ω: Comparison of exact (solid line) and linearized solution (dashed line).

According to Eq. (3.138), the larger the wobbling frequency Ω_0 and the amplitude $\hat{q}$, the larger the torque M_R required in the steady state. In addition, a higher material damping of the shaft (d_S), which represents the only energy sink for the stator-rotor system without the piezoceramic, increases the required torque acting on the rotor. This energy dissipation in the steady state results from permanent deformation of the shaft due to the wobbling motion of the stator. The contact-force ratio μ_0, introduced in Eq. (3.138), allows the verification of the stiction assumption concerning the contact point (3.122). According to Coulomb's law of friction the stiction constraint is violated for

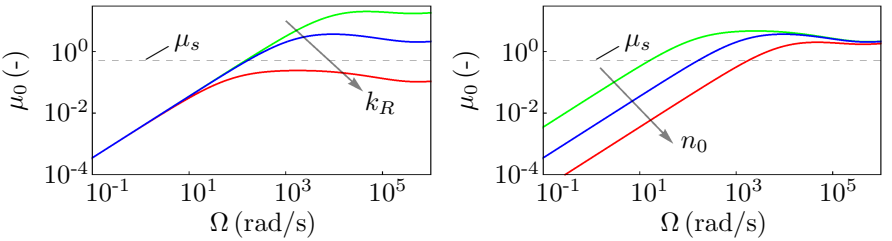

(a) Contact-force ratio μ_0 over Ω.

(b) Contact-force ratio μ_0 over Ω.

Figure 3.28: Variation of the rotor stiffness k_R and the pre-stress n_0; dashed line: limit of the kinematic assumption (stiction in the contact zone).

$F_T^*/F_N^* > \mu_s$, where μ_s is the static friction coefficient between the stator and the rotor. In Fig. 3.28 a static friction coefficient of $\mu_s = 0.5$ is displayed together with typical contact-force ratios, where the pre-stress n_0 and the rotor stiffness k_R are varied. In contrast to k_R, an increase of n_0 significantly lowers the contact-force ratio in the lower range of Ω leading to an extension of the range, where the stiction condition is satisfied. Although an increase of the pre-stress n_0 is beneficial for an adhesive contact kinematics, it also leads to a reduction of the region, where self-excited vibrations can be initiated, see section 3.2.

Comparison of steady-state characteristics for different elastic bedding torques

In the previous analysis a modified expression (3.124) was used instead of the coordinates-free description of the bedding torque (3.17). Using this modified torque, the steady-state solution of the nonlinear equations of motion (3.109) was identical to the wobbling motion in the EULER representation (3.91), (3.92). Thereby, the analysis of the steady state was significantly simplified. In case of the non-modified torque the steady-state solution cannot be given

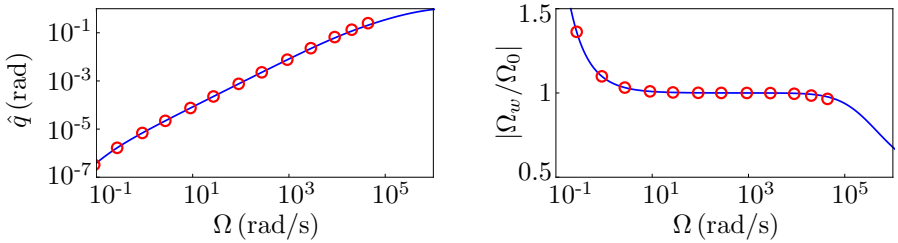

(a) Nutation angle $\hat{q}$ over Ω.

(b) Wobbling frequency Ω_w over Ω.

Figure 3.29: Steady-state characteristics over the rotation frequency Ω: Comparison for modified (solid line) and non-modified bedding torque (circles).

explicitly, but nevertheless corresponds very well to the wobbling motion, except for an additional oscillating term of a relatively small magnitude (about 0.1% of the mean value). However, the steady-state characteristics in both

cases agree with each other very precisely, see Fig. 3.29, where the mean value of the steady state is plotted for the non-modified torque.

Piezoelectric coupling

The aim of this section is to analyze the effect of the piezoceramic structure on the dynamic behavior of the stator-rotor system. To this end, the terms resulting from the deformation of the piezoceramic (3.18) are added to the bedding torque (3.124). Since the displacement of the piezoceramic structure is relatively small, the equations of motion can be linearized around the trivial solution of the piezoceramic ($q_{P_1} = q_{P_2} = 0$). For the sake of clarity, the left-hand side of the equations of motion for the stator (3.125) is summarized as $\mathbf{f}_L$ and the right-hand side as $\mathbf{f}_R$, respectively. By adding the terms resulting from the piezoceramic, the equation of motion is extended to

$$\mathbf{f}_L + d_S\,\mathbf{B}\,\dot{\mathbf{q}}_P + k_S\,\mathbf{B}\,\mathbf{q}_P = \mathbf{f}_R, \quad \text{with} \quad \mathbf{B}^{\mathrm{T}} = \begin{bmatrix} 0 & c_1 & s_1\,s_2 \\ 0 & s_1 & -c_1\,s_2 \end{bmatrix}, \tag{3.139}$$

where the abbreviations s_i and c_i denote $\sin q_{s_i}$ and $\cos q_{S_i}$, respectively. The coordinates of the piezoceramic surface are $\mathbf{q}_P = [q_{P_1}, q_{P_2}]^{\mathrm{T}}$, described in section 3.1.1. Since EULER angles are used as coordinates for the stator motion instead of CARDAN angles, the right-hand side of the equations of motion for the piezoceramic surface (3.57) changes. Thus, for the equations of motion for the piezoceramic follows

$$\mathbf{D}_P\,\dot{\mathbf{q}}_P + \mathbf{K}_P\,\mathbf{q}_P + \mathbf{\Gamma}\,\mathbf{v} = d_S\mathbf{B}^{\mathrm{T}}\dot{\mathbf{q}}_S + k_S\,\mathbf{f}_S, \quad \text{with} \quad \mathbf{f}_S = q_{S_2}[c_1, s_1]^{\mathrm{T}}, \tag{3.140}$$

where the matrices $\mathbf{D}_P, \mathbf{K}_P, \mathbf{\Gamma}$ are equivalent to the matrices (3.58) for $\alpha = 1$. Using the steady state solution for the stator coordinates in Euler description (3.91), (3.92) leads to the right-hand side ($\tan\hat{q} \approx \hat{q}$)

$$d_S\,\mathbf{B}^{\mathrm{T}}\,\dot{\mathbf{q}}_S^* + k_S\,\mathbf{f}_S^* = \mathbf{D}_S\,\dot{\widetilde{\mathbf{q}}}_S + \mathbf{K}_S\,\widetilde{\mathbf{q}}_S, \tag{3.141}$$

where $\widetilde{\mathbf{q}}_S = \hat{q}\,[\cos\Omega_w t, \sin\Omega_w t]^{\mathrm{T}}$. This expression for the right-hand side is identical to the one obtained by using CARDAN angles (3.57). This is not

surprising, since the choice of the generalized coordinates for the stator does not affect the dynamics of the piezoceramic structure. Inserting

$$q^*_{P_1} = P_c \cos\Omega_w t + P_s \sin\Omega_w t, \quad q^*_{P_2} = P_c \sin\Omega_w t - P_s \cos\Omega_w t \tag{3.142}$$

into Eq. (3.140), the steady-state solution for $\mathbf{q}_P$, which is characterized by P_c and P_s, is obtained as function of the wobbling frequency Ω_w and the amplitude $\hat{q}$. Thereby, Eqs. (3.139) simplify to

$$k_t\,\beta\cos\hat{q} = M_R, \tag{3.143}$$

$$\Omega_w^2\cos\hat{q}\sin\hat{q}(\Theta_S+\Theta_3\tan^2\hat{q}) - k_S\,\hat{q} + k_S P_c + d_S\,\Omega_w P_s = r_C^* F_N^*, \tag{3.144}$$

$$-d_S\Omega_w r_C^*\tan\hat{q} - k_S P_s\sin\hat{q} + d_S\Omega_w P_c\sin\hat{q} = M_R h_C^*. \tag{3.145}$$

The influence of the additional terms, resulting from the deformation the piezoceramic structure, on the steady-state characteristics is shown in Fig. 3.30. As expected, the wobbling frequency Ω_w is lowered, as a result of the softened

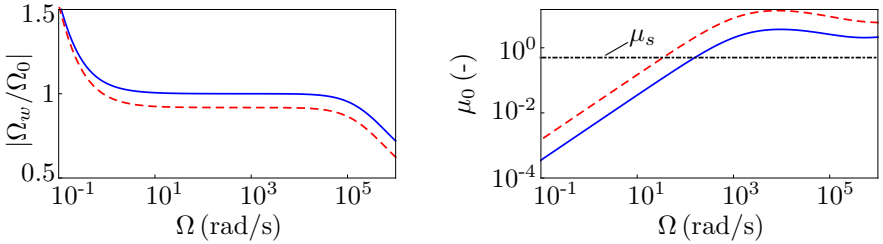

(a) Wobbling frequency Ω_w over Ω.

(b) Contact-force ratio μ_0 over Ω.

Figure 3.30: Steady-state characteristics over the rotation frequency Ω: Comparison for decoupled (solid line) and coupled piezoceramic (dashed line).

clamping of the shaft due to the piezoceramic (Fig. 3.30a). Moreover, the system damping is increased, mainly due to the electric resistances attached to the electrodes. This leads to a lower operation range, depicted in Fig. 3.30b, where, in the case of coupled piezoceramic, the static friction coefficient μ_s is reached for lower rotation speed Ω.

Electric power output

In the following, the steady-state characteristics of the wobbling disk generator is considered with respect to the electric power output. It is shown, how the system parameters have to be optimized in order to maximize the generated electric power.

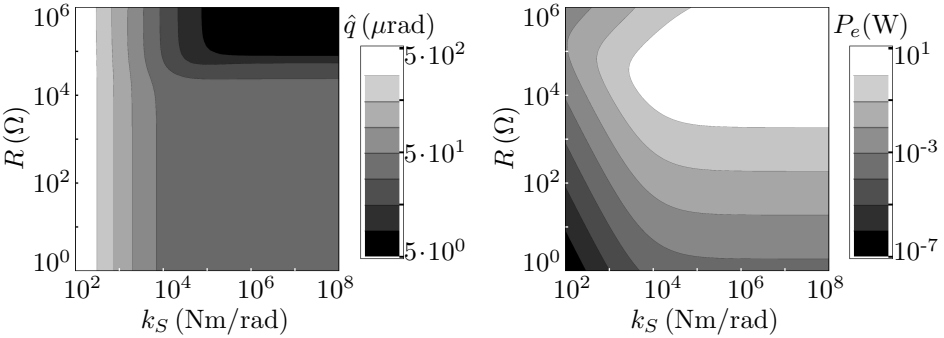

(a) Amplitude $\hat{q}$ over k_S and R.

(b) Power output P_e over k_S and R.

Figure 3.31: Characteristic map for the wobbling disk generator with piezo element attached: Variation of k_S and R (sliding in the contact zone).

Figure 3.31 shows the wobbling amplitude $\hat{q}$ and the electric power output P_e over a variation of the shaft stiffness k_S and the electric resistance R. Increasing k_S leads to a lower $\hat{q}$, but to an increase of P_e. The wobbling amplitude $\hat{q}$ is also significantly reduced for relatively high electric resistances ($R > 10\,\text{k}\Omega$). Regarding the electric power output, there exists always an optimum resistance R^* leading to a maximum. This optimum resistance R^* is shown together with the maximum power $P_e^{\max}$ in Fig. 3.32. The results are compared to the estimates (3.67) and (3.68), which were obtained by neglecting the feedback effect of the piezoceramic on the stator. The qualitative behavior is similar to the steady-state characteristics in the case of sliding in the contact zone, see section 3.3.2: For lower k_S the derived estimates correspond very well to the optimum resistance R^* and the maximum power output $P_e^{\max}$, whereas for larger values ($k_S > 10^5\,\text{Nm/rad}$) the estimation fails, due

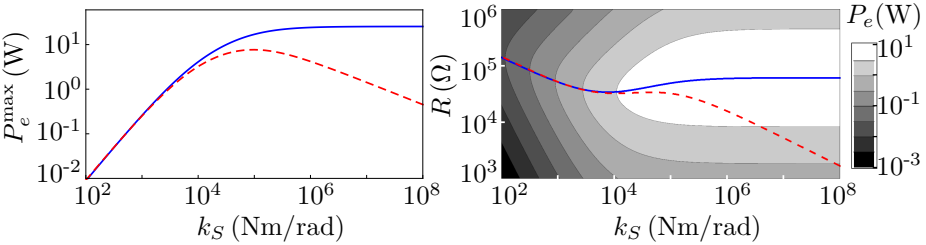

(a) Maximal power output $P_e^{\max}$. **(b)** Optimal resistance R^*.

Figure 3.32: Comparison of the optimal resistance R^* and maximal power output P_e^* without (solid line) and with (dashed line) the feedback effect.

to the non-negligible feedback effect. However, larger k_S leads to no further increase of $P_e^{\max}$, but to a significant decrease of the region, where self-excited vibrations occur, see section 3.2. Therefore, k_S should be optimized in the lower region ($k_S < 10^5\,\mathrm{Nm/rad}$) by considering both, the maximum power output and the effect on the self excitation.

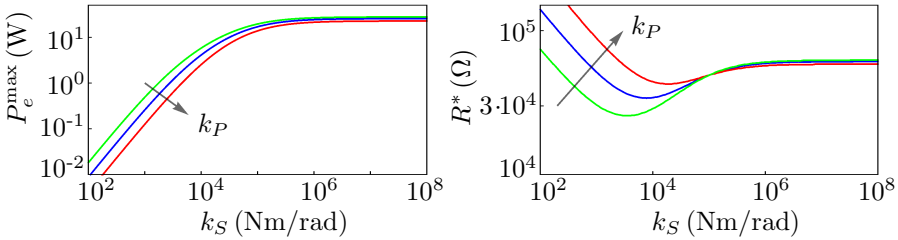

(a) Maximum power output $P_e^{\max}$. **(b)** Optimum resistance R^*.

Figure 3.33: Maximum power output and optimum electric resistance: Variation of the stiffness of the piezoceramic k_P.

The effect of the stiffness of the piezoceramic structure k_P on the maximum electric power output and the corresponding optimum resistance is shown in Fig. 3.33. A higher stiffness of the piezoceramic leads to lower maximum power output and to a larger optimum resistance. This is similar to the results shown in Fig. 3.25 in the case of sliding in the contact zone.

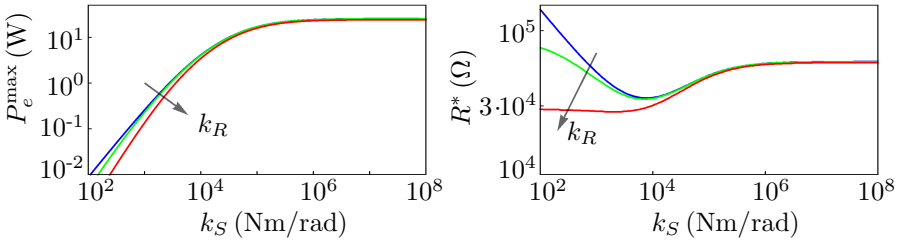

(a) Maximum power output $P_e^{\max}$.

(b) Optimum resistance R^*.

Figure 3.34: Maximum power output and optimum electric resistance: Variation of the stiffness of the rotor k_R.

In addition, Fig. 3.34 shows that a higher stiffness of the rotor k_R reduces the maximum power output and lowers the corresponding optimum resistance. Furthermore, for the calculated steady-state characteristics, it is of utmost importance to verify the kinematic made. Using the contact-force ratio according to Eq. (3.138), the region, where the kinematic assumption is violated, can be described by $\mu_0 > \mu_s$, in which μ_s corresponds to the static friction coefficient. This limit of the kinematic assumption is displayed in Fig. 3.35a,

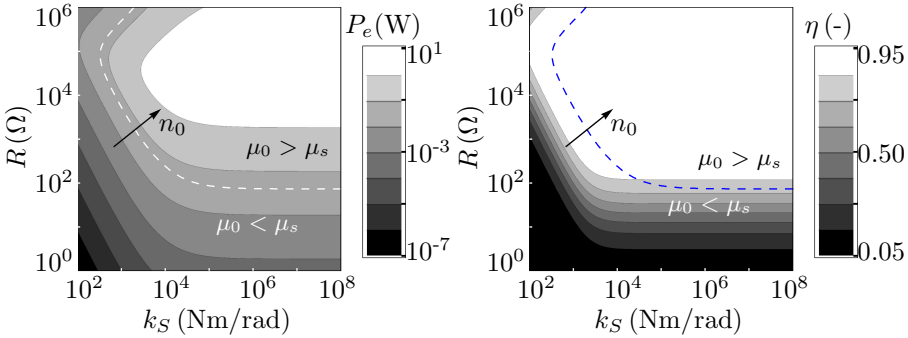

(a) Power output P_e over k_S and R.

(b) Efficiency η over k_S and R.

Figure 3.35: Power output and efficiency characteristics of the wobbling disk generator; dashed line: limit of the kinematic assumptions is given by $\mu_0 = \mu_s$.

where P_e is plotted over k_S and R. It can be observed that the kinematic assumption is violated in the region, where also the highest power output is generated. Clearly, a higher pre-stress n_0 increases the operation range, but has also the drawback of reducing the region, where self-excitation can occur. A similar behavior can be observed in Fig. 3.35b, where the efficiency[12] η is plotted over k_S and R: In the region with the highest efficiency the kinematic assumption is violated. Nevertheless, the calculated efficiency of the analyzed energy harvester is relatively high in a wide range of parameters.

[12]The efficiency is defined as the quotient between the harvested electric power and the mechanical power input through the rotor, $\eta := P_e/P_{\text{in}}$. The power input into the system is described by the rotation frequency and the torque acting on the rotor, $P_{\text{in}} = M_R\,\Omega$.

4 Traveling wave generator

This chapter deals with the modeling and the analysis of the traveling wave generator obtained by inverting the actuation of a plate-type ultrasonic motor. First, the equations of motion for the generator are derived in two different ways. The elastic stator, which is the main part of the generator, is modeled on the one hand, as an elastic ring and on the other hand as a plate. In the case of the elastic ring, the kinematics and the resulting equations of motion are simpler than for the plate and lead to good approximations of the traveling-wave motion of the stator. However, the influence of the rotation speed on the initiation of self-excited vibrations, which can be observed in the experiments (chapter 6), is missing. Therefore, the more detailed plate model is used instead to describe the initiation of self-excited vibrations. These results are then compared to a numerical analysis carried out with finite element methods. Regarding the steady-state characteristics of the generator, estimates are derived based on two different kinematic assumptions, namely sliding friction in the contact zone and adhesive contact.

4.1 Modeling

Figure 4.1 shows a simplified model of a traveling wave generator, which has the same structure as the wobbling disk generator, but with two main differences: The dynamic behavior of the stator is described by vibrations of a continuous system and not by a rigid body motion, as it was the case for the wobbling disk generator. Furthermore, the piezoceramic, which transforms mechanical into electrical energy, is attached directly to the stator in form of a thin layer. The working principle of the traveling wave generator is in general the same as for the wobbling disk generator. The power input into the system is done by the rotation of the rotor, which is pressed against the

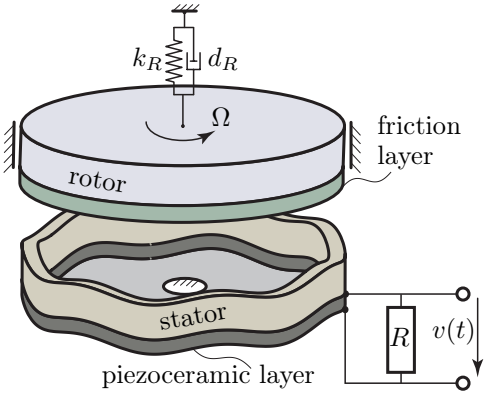

Figure 4.1: Simplified model of a traveling wave generator.

stator. The rotor interacts with the stator through the friction layer leading to self-excited vibrations of the stator. Consequently, it comes to deformation of the piezoceramic layer, which generates electric power. The surface of the piezoceramic layer is divided into several electrode segments, at which electric loads are attached.

The goal of this chapter is to derive simple electromechanical models describing the dynamic behavior of the traveling wave generator. Clearly, it depends on the dynamic property to describe, which model is more appropriate. In case of the traveling wave generator, two main dynamic phenomena have to be analyzed: The first one is the initiation of self-excited vibrations, which basically is reduced to a stability analysis of the linearized system. The second one is the optimization of the resulting steady-state vibrations in order to achieve an efficient power transmission through the generator. Here, the properties of the piezoelectric layer and the corresponding electric parts are of utmost importance.

An obvious modeling approach to describe the dynamics of the stator is to use Euler-Bernoulli beam theory, since this is the simplest theory describing bending vibrations. However, this approach is inadequate for the stability analysis of the linearized system, since the additional damping effect through the friction layer, which is observed in the experiments, is not included in this model. Nevertheless, in the analysis and optimization of the steady-

state behavior this approach is sufficient. In case of the stability analysis, the KIRCHHOFF plate theory is used instead of the EULER-BERNOULLI beam theory, to describe the dynamics of the stator, in order to depict all the main effects observed in the experiments. For this reason, the equations of motion for the stator are derived using both theories.

The derivation of the equations of motion for the traveling wave generator is done in the following using HAMILTON's principle, which reads

$$\delta \int_{t_1}^{t_2} (\mathcal{L} + \mathcal{W}) \, \mathrm{dt} = 0, \qquad \text{with} \quad \mathcal{L} = \mathcal{T} - \mathcal{U}, \tag{4.1}$$

where $\mathcal{L}$ is the LAGRANGEian and $\mathcal{W}$ the work done by external forces. The functionals $\mathcal{T}$ and $\mathcal{U}$ denote the kinetic and potential energy, respectively. This is a common approach for the derivation of the equations of motion for continuous system and is described in detail in [15, 43].

4.1.1 Elastic ring model

In this section the stator, shown in Fig. 4.1, is modeled as an elastic ring using EULER-BERNOULLI beam theory. The coordinate, describing the neutral fiber of the ring, can be chosen in two different ways, as it can be seen for the top view of the ring in Fig. 4.2a: On the one hand the coordinate x can be used, which describes the arc length of the ring. On the other hand the polar coordinate φ can be used. The relation between these two coordinates and the corresponding derivative operators are

$$x = r\,\varphi \qquad \text{and} \qquad \mathrm{dx} = r\,\mathrm{d}\varphi \quad \Longleftrightarrow \quad \frac{\mathrm{d}}{\mathrm{dx}} = \frac{1}{r}\frac{\mathrm{d}}{\mathrm{d}\varphi}\,, \tag{4.2}$$

where r denotes the radius to the neutral fiber. An infinitesimal part of the ring is illustrated in Fig. 4.2b. The lower surface of the elastic stator is bedded on distributed spring-damper elements with the stiffness and damping coefficients k_S and d_S. The friction layer, which is connected to the rotor, also consists of distributed spring-damper elements (k_f, d_f), whose ends are in contact with the upper surface of the stator and are subject to friction

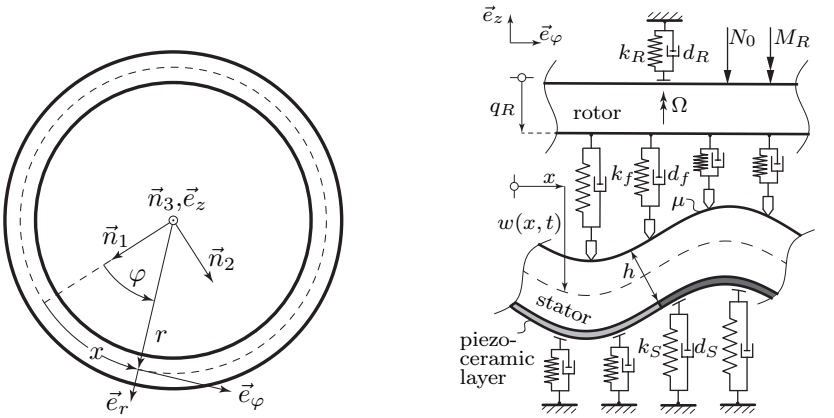

(a) Top view on the elastic ring. **(b)** Simplified mechanical model.

Figure 4.2: Simplified mechanical modeling of the traveling wave generator.

(friction coefficient μ). On the rotor, which is assumed to be rigid, act the pre-stress force N_0 and the torque M_R. The visco-elastic support of the rotor has the stiffness and damping coefficients k_R and d_R. The rotor has two degrees of freedom, namely one translatory and one rotatory, denoted by q_R and Ω, respectively. In case of the stator, the vertical displacement ($\vec{e}_z$-direction) of the neutral fiber is described by $w(x,t)$. The corresponding boundary conditions read

$$\frac{\partial^i}{\partial x^i} w(0,t) = \frac{\partial^i}{\partial x^i} w(\ell,t), \quad \text{for} \quad i = 0, \cdots, 3, \tag{4.3}$$

where the characteristic length of the beam is equivalent to the circumference of the ring, $\ell = 2\pi r$. Applying the identity (4.2), the boundary conditions for φ as coordinate read

$$\frac{\partial^i}{\partial \varphi^i} w(0,t) = \frac{\partial^i}{\partial \varphi^i} w(2\pi,t), \quad \text{for} \quad i = 0, \cdots, 3. \tag{4.4}$$

In the following, the equations of motion are derived using HAMILTON's principle (4.1). To this end, it is necessary to derive the expressions for the kinetic and potential energy as well as for the work done by external forces. According to the EULER-BERNOULLI beam theory [15, 43], the kinetic and potential

energy of the elastic stator are

$$\mathcal{T} = \frac{1}{2}\int_0^\ell \rho A\, \dot{w}^2(x,t)\,\mathrm{dx}\ , \quad \mathcal{U} = \frac{1}{2}\int_0^\ell EI\, w_{,xx}^2(x,t)\,\mathrm{dx}. \tag{4.5}$$

The parameters ρ and A are the mass density and the cross section of the stator. Moreover, E and I are the YOUNG's modulus and the area moment of inertia. The work done by external forces consists of two parts, namely the work done by the visco-elastic bedding $\mathcal{W}_S$ and by the friction layer $\mathcal{W}_f$,

$$\mathcal{W} = \mathcal{W}_S + \mathcal{W}_f. \tag{4.6}$$

The variation of $\mathcal{W}_S$ is

$$\delta\mathcal{W}_S = \int_0^\ell \vec{f}_S \cdot \delta\vec{r}_S\,\mathrm{dx}. \tag{4.7}$$

By using

$$\vec{f}_S = (k_S\, w + d_S\, \dot{w})\,\vec{e}_z \quad \text{and} \quad \delta\vec{r}_S = -\delta w\,\vec{e}_z, \tag{4.8}$$

the variation of $\mathcal{W}_S$ simplifies to

$$\delta\mathcal{W}_S = -\int_0^\ell (k_S\, w + d_S\, \dot{w})\ \delta w\,\mathrm{dx}. \tag{4.9}$$

Similarly, for the variation of $\mathcal{W}_f$ follows

$$\delta\mathcal{W}_f = \int_0^\ell \vec{f}_C \cdot \delta\vec{r}_C\,\mathrm{dx}. \tag{4.10}$$

In order to derive the expression for the distributed contact force $\vec{f}_C$ the contact kinematics have to be stated first.

Contact force and kinematics

The position vector of the point on the neutral fiber S_o and the contact point S_C on the stator (Fig. 4.3a) are

$${}^{\mathcal{N}_o}\vec{p}^{\,S_o} = r\,\vec{e}_r - w\,\vec{e}_z, \qquad {}^{S_o}\vec{p}^{\,S_C} = \frac{h}{2}\,\vec{e}_n. \tag{4.11}$$

The rotation matrix between the direction vectors $\vec{e}_\varphi, \vec{e}_z$ and the normal and tangential vectors of the neutral fiber is defined as

$$\begin{bmatrix} \vec{e}_t \\ \vec{e}_n \end{bmatrix} = \begin{bmatrix} \cos\phi & -\sin\phi \\ \sin\phi & \cos\phi \end{bmatrix} \begin{bmatrix} \vec{e}_\varphi \\ \vec{e}_z \end{bmatrix}, \tag{4.12}$$

where the angle ϕ depends on the gradient $w_{,x}$

$$\tan\phi = w_{,x}\,, \quad \cos\phi = 1/\sqrt{1+w_{,x}^2}\,, \quad \sin\phi = w_{,x}/\sqrt{1+w_{,x}^2}\,. \tag{4.13}$$

Using the relations (4.13), the position vector of the contact point S_C reads

$${}^{\mathcal{N}_o}\vec{p}^{\,S_C} = r\,\vec{e}_r + \frac{h}{2}\sin\phi\,\vec{e}_\varphi + (\frac{h}{2}\cos\phi - w)\,\vec{e}_z. \tag{4.14}$$

The corresponding velocity of the contact point S_C is given by the time-derivative of the position vector

$${}^{S_C}\vec{v}^{\mathcal{N}} = \frac{\mathrm{d}^{\mathcal{N}}}{\mathrm{dt}}\,{}^{\mathcal{N}_o}\vec{p}^{\,S_C} = \frac{h}{2}\,\dot{\phi}\cos\phi\,\vec{e}_\varphi - (\frac{h}{2}\,\dot{\phi}\sin\phi + \dot{w})\,\vec{e}_z, \tag{4.15}$$

with $\dot{\phi} = \dot{w}_{,x}/(1+w_{,x}^2)$. The velocity of the point R_C on the contact pin is

$${}^{R_C}\vec{v}^{\mathcal{N}} = {}^{R}\vec{\omega}^{\mathcal{N}} \times {}^{\mathcal{N}_o}\vec{p}^{\,S_C} + \dot{h}_S\,\vec{e}_z, \tag{4.16}$$

where h_S is the height of S_C in $\vec{e}_z$-direction (Fig. 4.3b) and ${}^{R}\vec{\omega}^{\mathcal{N}}$ the angular velocity of the rotor given by ${}^{R}\vec{\omega}^{\mathcal{N}} = \Omega\,\vec{e}_z$. The height h_S can be calculated from

$$h_S = {}^{\mathcal{N}_o}\vec{p}^{\,S_C}\cdot\vec{e}_z = \frac{h}{2}\cos\phi - w, \qquad \dot{h}_S = -\frac{h}{2}\,\dot{\phi}\sin\phi - \dot{w}. \tag{4.17}$$

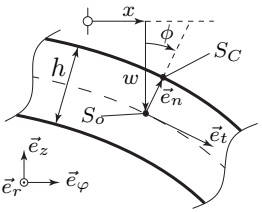

(a) Kinematics of a ring element.

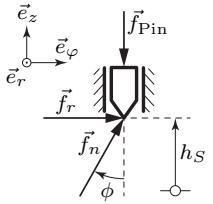

(b) Free-body diagram.

Figure 4.3: Kinematics of the stator surface and forces on a single contact pin.

Thus, the velocity of R_C simplifies to

$$ {}^{R_C}\vec{v}^{\mathcal{N}} = -\Omega\,\frac{h}{2}\sin\phi\,\vec{e}_r + \Omega\,r\,\vec{e}_\varphi - (\frac{h}{2}\,\dot{\phi}\sin\phi + \dot{w})\,\vec{e}_z. \tag{4.18} $$

Using the velocities of the points S_C and R_C for the relative velocity gives

$$ \begin{aligned} &\Delta\vec{v} = {}^{S_C}\vec{v}^{\mathcal{N}} - {}^{R_C}\vec{v}^{\mathcal{N}} = \Delta v_r\,\vec{e}_r + \Delta v_\varphi\,\vec{e}_\varphi, \quad \text{with} \\ &\Delta v_r = \Omega\,\frac{h}{2}\sin\phi, \qquad \Delta v_\varphi = \frac{h}{2}\,\dot{\phi}\cos\phi - \Omega\,r. \end{aligned} \tag{4.19} $$

Coulomb's law of friction for the contact forces acting on the stator surface leads to

$$ \vec{f}_n = -f_n\,\vec{e}_n, \qquad \vec{f}_r = -\mu\,f_n\,\frac{\Delta\vec{v}}{|\Delta\vec{v}|}. \tag{4.20} $$

The force on the contact pin, shown in Fig. 4.3b, is

$$ \vec{f}_{\mathrm{Pin}} = -f_{\mathrm{Pin}}\,\vec{e}_z, \quad \text{with} \quad f_{\mathrm{Pin}} = k_f(q_R + h_S) + d_f(\dot{q}_R + \dot{h}_S). \tag{4.21} $$

Force balance for the contact pin in the $\vec{e}_z$-direction yields

$$ f_n = \frac{f_{\mathrm{Pin}}}{\cos\phi}. \tag{4.22} $$

Thus, the distributed contact force $\vec{f}_C$ acting on the ring surface reads

$$ \vec{f}_C = \vec{f}_n + \vec{f}_r = -f_{\mathrm{Pin}}\left[\frac{\mu}{\cos\phi}\frac{\Delta v_r}{|\Delta\vec{v}|}\vec{e}_r + \left(\tan\phi + \frac{\mu}{\cos\phi}\frac{\Delta v_\varphi}{|\Delta\vec{v}|}\right)\vec{e}_\varphi + \vec{e}_z\right]. \tag{4.23} $$

The variation of the work done by the distributed contact force is

$$ \delta\mathcal{W}_f = \int_0^\ell \vec{f}_C\cdot\delta\vec{r}_C\,\mathrm{dx} = \int_0^\ell \vec{f}_C\cdot\left(\frac{\delta\vec{r}_C}{\delta w}\delta w + \frac{\delta\vec{r}_C}{\delta w_{,x}}\delta w_{,x}\right)\mathrm{dx}\,. \tag{4.24} $$

The position vector of the contact force is $\vec{r}_C = {}^{\mathcal{N}_o}\vec{p}^{\,S_C}$, see Eq. (4.14). Thus, for the partial derivatives of the position vector follows

$$ \frac{\delta\vec{r}_C}{\delta w} = -\vec{e}_z, \qquad \frac{\delta\vec{r}_C}{\delta w_{,x}} = \frac{h}{2}\,\frac{\vec{e}_\varphi - w_{,x}\,\vec{e}_z}{(1 + w_{,x}^2)^{\frac{3}{2}}}. \tag{4.25} $$

Thereby, the variation of $\mathcal{W}_f$ simplifies to

$$ \delta\mathcal{W}_f = \int_0^\ell \left(f_{\mathrm{Pin}}\delta w - \mu f_{\mathrm{Pin}}\frac{h}{2}\cos^2\phi\frac{\Delta v_\varphi}{|\Delta\vec{v}|}\delta w_{,x}\right)\mathrm{dx}\,. \tag{4.26} $$

Ritz discretization

The idea of the Ritz approach is to expand the solution of a partial differential equation into shape functions fulfilling the geometric boundary conditions,

$$w(x,t) = \sum_i W_i(x)\, q_i(t). \tag{4.27}$$

The shape functions are W_i and the modal coordinates are q_i. Inserting this expansion into the energy expressions (4.5) and carrying out the variation with respect to the q_i yields

$$\delta\mathcal{L} = \int_0^\ell \left[\rho A \sum_i W_i\, \dot{q}_i \sum_j W_j\, \delta\dot{q}_j - EI \sum_i W_i''\, q_i \sum_j W_j''\, \delta q_j \right] \mathrm{dx}, \tag{4.28}$$

where $(\cdot)' = \frac{\partial}{\partial x}$. In the same way, Eqs. (4.9) and (4.26) give

$$\delta\mathcal{W}_S = -\int_0^\ell \left[k_S \sum_i W_i\, q_i + d_S \sum_i W_i\, \dot{q}_i \right] \sum_j W_j\, \delta q_j \,\mathrm{dx}, \tag{4.29}$$

$$\delta\mathcal{W}_f = \int_0^\ell \left[f_{\mathrm{Pin}} \sum_j W_j\, \delta q_j - \mu f_{\mathrm{Pin}} \frac{h}{2} \cos^2\phi\, \mathrm{sign}\Delta v \sum_j W_j'\, \delta q_j \right] \mathrm{dx}. \tag{4.30}$$

Further, according to the Hamilton's principle (4.1) one has

$$\begin{aligned} \int_{t_1}^{t_2} \int_0^\ell \Bigg[& \rho A \sum_i \sum_j W_i W_j\, \ddot{q}_i\, \delta q_j + EI \sum_i \sum_j W_i'' W_j''\, q_i\, \delta q_j \\ & + k_S \sum_i \sum_j W_i W_j\, q_i\, \delta q_j + d_S \sum_i \sum_j W_i W_j\, \dot{q}_i\, \delta q_j \\ & - f_{\mathrm{Pin}} \sum_j W_j\, \delta q_j + \mu f_{\mathrm{Pin}} \frac{h}{2} \cos^2\phi\, \frac{\Delta v_\varphi}{|\Delta\vec{v}|} \sum_j W_j'\, \delta q_j \Bigg] \mathrm{dx}\,\mathrm{dt} = 0\,. \end{aligned} \tag{4.31}$$

This expression can be summarized to

$$\int_{t_1}^{t_2} \sum_j H_j\, \delta q_j \,\mathrm{dt} = 0\,, \tag{4.32}$$

where the H_j have to vanish for all times. This leads to a system of ordinary differential equations in the modal coordinates q_i. Linearizing[1] around the trivial solution $q_i = 0$ yields

$$\mathbf{M}\,\ddot{\mathbf{q}} + \mathbf{B}\,\dot{\mathbf{q}} + \mathbf{C}\,\mathbf{q} = \mathbf{f}\,. \tag{4.33}$$

The modal coordinates q_i form the state vector $\mathbf{q}$. The elements of the matrices $\mathbf{M}, \mathbf{B}$ and $\mathbf{C}$ read

$$m_{ij} = \int_0^\ell \rho A\, W_i W_j \,\mathrm{dx}, \tag{4.34}$$

$$b_{ij} = \int_0^\ell \left[(d_S + d_f)\, W_i W_j + \mu \frac{h}{2} d_f \,\mathrm{sign}\,\Omega\, W_i W_j' \right] \mathrm{dx}, \tag{4.35}$$

$$c_{ij} = \int_0^\ell \left[EI\, W_i'' W_j'' + (k_S + k_f) W_i W_j + \mu \frac{h}{2} k_f \,\mathrm{sign}\,\Omega\, W_i W_j' \right] \mathrm{dx}\,. \tag{4.36}$$

The elements of the force vector $\mathbf{f}$ on the right-hand side are

$$f_i = n_0 \int_0^\ell \left(W_i + \mu \frac{h}{2} \,\mathrm{sign}\,\Omega\, W_i' \right) \mathrm{dx}, \tag{4.37}$$

where the pre-stress is denoted by $n_0 = k_f\,(h/2 + q_R)$.

An obvious choice for the shape function W_i, which fulfill the boundary conditions (4.4) is

$$\Big[W_0,\, W_1,\, W_2,\, \cdots \Big] = \Big[1,\, \sin\varphi,\, \cos\varphi,\, \sin 2\varphi,\, \cos 2\varphi,\, \cdots \Big]\,. \tag{4.38}$$

Thereby, the system of ordinary differential equations (4.33) strongly simplifies. For $i = 0$ the decoupled differential equation reads

$$m_0\, \ddot{q}_0(t) + d_0\, \dot{q}_0(t) + k_0\, q_0(t) = f_0, \quad \text{with} \tag{4.39}$$

$$m_0 = 2\pi r \rho A,\;\; d_0 = 2\pi r (d_S + d_f),\;\; k_0 = 2\pi r (k_S + k_f),\;\; f_0 = 2\pi\, r\, n_0. \tag{4.40}$$

For $i > 0$ each pair of modal coordinates with shape function W_i of the same wave number κ is coupled. The differential equations for the κ^{th} mode pair

[1] In this case, the nonlinearity arises due to the kinematics in the friction layer.

are

$$\mathbf{M}_\kappa\,\ddot{\mathbf{q}}_\kappa(t)+(\mathbf{D}_\kappa+\mathbf{G}_\kappa)\,\dot{\mathbf{q}}_\kappa(t)+(\mathbf{K}_\kappa+\mathbf{N}_\kappa)\,\mathbf{q}_\kappa(t)=\mathbf{0}, \tag{4.41}$$

with

$$\begin{gathered}\mathbf{M}_\kappa=\pi r\rho A\,\mathbf{I},\quad \mathbf{D}_\kappa=\pi r(d_S+d_f)\,\mathbf{I},\quad \mathbf{K}_\kappa=\left(\pi r(k_S+k_f)+\pi\kappa^4\frac{EI}{r^3}\right)\mathbf{I},\\ \mathbf{G}_\kappa=\mu\frac{h}{2}\pi\kappa d_f\,\operatorname{sign}\Omega\begin{bmatrix}0&1\\-1&0\end{bmatrix},\quad \mathbf{N}_\kappa=\mu\frac{h}{2}\pi\kappa k_f\,\operatorname{sign}\Omega\begin{bmatrix}0&1\\-1&0\end{bmatrix}.\end{gathered} \tag{4.42}$$

This linearized system is very similar to the one of the wobbling disk generator in Eq. (3.51). As already mentioned, the additional damping effect due to the friction layer is not present in this model. This is due to the fact that the used beam theory does not consider deflection in the radial direction of the ring.

4.1.2 Elastic plate model

In the model derived using Euler-Bernoulli beam theory an essential phenomenon, observed in experiments, is not present. This phenomenon describes the additional damping effect of the system, depending on the pre-stress and rotation speed of the rotor. The dynamics of the stator are therefore refined using Kirchhoff plate theory, described in [15, 23, 43].

The equations of motion are again derived from Hamilton's principle (4.1). Therefore, the energy expressions for the traveling wave generator are required. According to Kirchhoff plate theory, the expressions for the kinetic and potential energy of the stator read

$$\mathcal{T}=\frac{1}{2}\int_{\mathrm{A}}\rho h\dot{w}^2\,\mathrm{dA},\quad \mathcal{U}=\frac{1}{2}\int_{\mathrm{A}}B\left[(\tau_r+\tau_\varphi)^2-2(1-\nu)(\tau_r\tau_\varphi-\tau_{r\varphi}^2)\right]\mathrm{dA}. \tag{4.43}$$

The abbreviations used are

$$\tau_r=w_{,rr},\quad \tau_\varphi=\frac{w_{,r}}{r}+\frac{w_{,\varphi\varphi}}{r^2},\quad \tau_{r\varphi}=\frac{w_{,\varphi r}}{r}-\frac{w_{,\varphi}}{r^2},\quad B=\frac{Eh^3}{12(1-\nu^2)}. \tag{4.44}$$

The variable w describes the deflection of the neutral plane A of the plate and depends on the polar coordinates r and φ. The plate has the thickness h,

YOUNG's modulus E and POISSON ratio ν. Further, the work done by external forces consists of a part resulting from material damping and another from the friction layer,

$$\mathcal{W} = \mathcal{W}_d + \mathcal{W}_f. \tag{4.45}$$

The variation of the work done by material damping is

$$\delta\mathcal{W}_d = -\int_{\mathrm{A}} d_S\, \dot{w}\, \delta w \,\mathrm{dA}. \tag{4.46}$$

The variation of the work done by the friction layer is

$$\delta\mathcal{W}_f = \int_{\mathrm{A_C}} \vec{f}_C \cdot \delta\vec{r}_C \,\mathrm{dA_C}, \tag{4.47}$$

where $\delta\vec{r}_C$ is the position vector to the distributed contact force $\vec{f}_C$ acting on the surface of the stator $\mathrm{A_C}$. In order to describe the contact force acting on the stator, the contact kinematics is required.

Contact force and kinematics

For the neutral plane of the stator one has

$${}^{\mathcal{N}_o}\vec{p}^{\,S_o} = r\,\vec{e}_r - w\,\vec{e}_z. \tag{4.48}$$

The gradient vectors of the neutral plane with respect to r and φ are

$$\vec{g}_r = \frac{\partial}{\partial r}{}^{\mathcal{N}_o}\vec{p}^{\,S_o} = \vec{e}_r - w_{,r}\,\vec{e}_z \quad \text{and} \quad \vec{g}_\varphi = \frac{1}{r}\frac{\partial}{\partial\varphi}{}^{\mathcal{N}_o}\vec{p}^{\,S_o} = \vec{e}_\varphi - \frac{w_{,\varphi}}{r}\,\vec{e}_z. \tag{4.49}$$

The normal vector $\vec{e}_n$ on the neutral plane is orthogonal to $\vec{g}_r$ and $\vec{g}_\varphi$, thus

$$\begin{aligned} &\vec{e}_n = \frac{\vec{g}_r \times \vec{g}_\varphi}{|\vec{g}_r \times \vec{g}_\varphi|} = \epsilon_r\,\vec{e}_r + \epsilon_\varphi\,\vec{e}_\varphi + \epsilon_z\,\vec{e}_z \quad \text{with} \\ &\epsilon_r = w_{,r}\,\epsilon_z, \quad \epsilon_\varphi = \frac{w_{,\varphi}}{r}\,\epsilon_z, \quad \epsilon_z = 1/\sqrt{1 + w_{,r}^2 + \frac{w_{,\varphi}^2}{r^2}}. \end{aligned} \tag{4.50}$$

The position vector to a single contact point is

$$\begin{aligned} {}^{\mathcal{N}_o}\vec{p}^{\,S_C} &= {}^{\mathcal{N}_o}\vec{p}^{\,S_o} + \frac{h}{2}\,\vec{e}_n, \\ {}^{\mathcal{N}_o}\vec{p}^{\,S_C} &= (r + \frac{h}{2}\,\epsilon_r)\,\vec{e}_r + \frac{h}{2}\,\epsilon_\varphi\,\vec{e}_\varphi + (\frac{h}{2}\,\epsilon_z - w)\,\vec{e}_z. \end{aligned} \tag{4.51}$$

The velocity of the contact point on the elastic stator S_C is

$$ {}^{S_C}\vec{v}^{\mathcal{N}} = \frac{\mathrm{d}^{\mathcal{N}}}{\mathrm{d}t}{}^{\mathcal{N}_o}\vec{p}^{\,S_C} = \frac{h}{2}\,\dot{\epsilon}_r\,\vec{e}_r + \frac{h}{2}\,\dot{\epsilon}_\varphi\,\vec{e}_\varphi + (\frac{h}{2}\,\dot{\epsilon}_z - \dot{w})\,\vec{e}_z. \tag{4.52} $$

For the velocity of the point R_C on the contact pin follows

$$ {}^{R_C}\vec{v}^{\mathcal{N}} = {}^{R}\vec{\omega}^{\mathcal{N}} \times {}^{\mathcal{N}_o}\vec{p}^{\,S_C} + \dot{h}_S\vec{e}_z = -\Omega\frac{h}{2}n_\varphi\vec{e}_r + \Omega(r+\frac{h}{2}n_r)\vec{e}_\varphi + \dot{h}_S\vec{e}_z, \tag{4.53} $$

where the angular velocity of the rotor is ${}^{R}\vec{\omega}^{\,\mathcal{N}} = \Omega\,\vec{e}_z$ and the height h_S (Fig. 4.3b) is defined as

$$ h_S = {}^{\mathcal{N}_o}\vec{p}^{\,S_C}\cdot\vec{e}_z = \frac{h}{2}\epsilon_z - w, \qquad \dot{h}_S = \frac{h}{2}\dot{\epsilon}_z - \dot{w}. \tag{4.54} $$

Using the expressions (4.52) and (4.53) for the relative velocity gives

$$ \begin{aligned} &\Delta\vec{v} = {}^{S_C}\vec{v}^{\mathcal{N}} - {}^{R_C}\vec{v}^{\mathcal{N}} = \Delta v_r\,\vec{e}_r + \Delta v_\varphi\,\vec{e}_\varphi, \quad \text{with} \\ &\Delta v_r = \frac{h}{2}\dot{\epsilon}_r + \Omega\frac{h}{2}\epsilon_\varphi, \quad \Delta v_\varphi = \frac{h}{2}\dot{\epsilon}_\varphi - \Omega\left(r + \frac{h}{2}\epsilon_r\right). \end{aligned} \tag{4.55} $$

Since the relative velocity lies in the horizontal plane ($\vec{e}_r$-$\vec{e}_\varphi$-plane), this holds also for the orientation of the friction force $\vec{f}_r$. Applying Coulomb's law of friction yields

$$ \vec{f}_n = -f_n\,\vec{e}_n \quad \text{and} \quad \vec{f}_r = -\mu\,f_n\,\frac{\Delta\vec{v}}{|\Delta\vec{v}|}. \tag{4.56} $$

The force on the contact pin is given by

$$ \vec{f}_{\mathrm{Pin}} = -f_{\mathrm{Pin}}\,\vec{e}_z \quad \text{with} \quad f_{\mathrm{Pin}} = k_f(q_R + h_S) + d_f(\dot{q}_R + \dot{h}_S). \tag{4.57} $$

From the force balance for the contact pin in $\vec{e}_z$-direction (Fig. 4.3b) follows

$$ f_n = \frac{f_{\mathrm{Pin}}}{\epsilon_z}. \tag{4.58} $$

By using this relation the contact force $\vec{f}_C$ can be expressed as

$$ \vec{f}_C = \vec{f}_n + \vec{f}_r = -f_{\mathrm{Pin}}\left[\left(w_{,r}\vec{e}_r + \frac{w_{,\varphi}}{r}\vec{e}_\varphi + \vec{e}_z\right) + \frac{\mu}{\epsilon_z}\left(\frac{\Delta v_r}{|\Delta\vec{v}|}\vec{e}_r + \frac{\Delta v_\varphi}{|\Delta\vec{v}|}\vec{e}_\varphi\right)\right]. \tag{4.59} $$

The variation of the work done by the distributed contact force $\vec{f}_C$ reads

$$\delta\mathcal{W}_f = \int_{\mathrm{A_C}} \vec{f}_C \cdot \delta\vec{r}_C \,\mathrm{dA_C} = \int_{\mathrm{A_C}} \vec{f}_C \cdot \left(\frac{\delta\vec{r}_C}{\delta w}\delta w + \frac{\delta\vec{r}_C}{\delta w_{,r}}\delta w_{,r} + \frac{\delta\vec{r}_C}{\delta w_{,\varphi}}\delta w_{,\varphi} \right) \mathrm{dA_C}, \quad (4.60)$$

where $\vec{r}_C = {}^{\mathcal{N}_o}\vec{p}^{\,S_C}$. Using the expression for the position vector (4.51) yields

$$\begin{aligned} \frac{\delta\vec{r}_C}{\delta w} &= -\vec{e}_z\,, \quad \frac{\delta\vec{r}_C}{\delta w_{,r}} = \frac{h}{2}\epsilon_z^3 \left[(1+\frac{w_{,\varphi}^2}{r^2})\vec{e}_r - \frac{w_{,r}w_{,\varphi}}{r}\vec{e}_\varphi - w_{,r}\vec{e}_z \right], \\ \frac{\delta\vec{r}_C}{\delta w_{,\varphi}} &= -\frac{h}{2}\epsilon_z^3 \left(\frac{w_{,r}w_{,\varphi}}{r}\vec{e}_r - (1+w_{,r}^2)\vec{e}_\varphi + \frac{w_{,\varphi}}{r}\vec{e}_z \right). \end{aligned} \quad (4.61)$$

Thereby, the variation of $\mathcal{W}_f$ results in

$$\begin{aligned} \delta\mathcal{W}_f = \int_{\mathrm{A_C}} f_{\mathrm{Pin}} \Bigg[& \delta w - \frac{h}{2}\mu\epsilon_z^2 \left((1+\frac{w_\varphi^2}{r^2})\frac{\Delta v_r}{|\Delta\vec{v}|} - \frac{w_r w_\varphi}{r}\frac{\Delta v_\varphi}{|\Delta\vec{v}|} \right)\delta w_{,r} \\ & + \mu\frac{h}{2}\epsilon_z^2 \left(\frac{w_{,r}w_{,\varphi}}{r}\frac{\Delta v_r}{|\Delta\vec{v}|} - (1+w_{,r}^2)\frac{\Delta v_\varphi}{|\Delta\vec{v}|} \right)\delta w_{,\varphi} \Bigg] \mathrm{dA_C}\,. \end{aligned} \quad (4.62)$$

Ritz discretization

According to the Ritz approach, the solution of a partial differential equation is expanded using shape functions fulfilling at least the geometric boundary conditions. By applying Hamilton's principle, the variation is carried out with respect to the modal coordinates q_i, in

$$w(r,\varphi,t) = \sum_i W_i(r) Q_i(\varphi)\, q_i(t)\,, \quad (4.63)$$

where W_i and Q_i are shape functions in the radial and circumferential direction, respectively. Inserting into the expression for the kinetic energy (4.43) and carrying out the variation with respect to the q_i yields

$$\delta\mathcal{T} = -\int_{\mathrm{A}} \rho h \sum_i \sum_j W_i Q_i W_j Q_j\, \ddot{q}_i\, \delta q_j \,\mathrm{dA}\,. \quad (4.64)$$

In the same way, for the variation of the potential energy follows

$$\delta\mathcal{U} = \int_{\mathrm{A}} B \Bigg[\sum_i \sum_j \left(W_i'' Q_i + \frac{1}{r} W_i' Q_i + \frac{1}{r^2} W_i Q_i'' \right) \left(W_j'' Q_j + \frac{1}{r} W_j' Q_j + \frac{1}{r^2} W_j Q_j'' \right) q_i \delta q_j$$
$$-2(1-\nu) \Bigg(\sum_i \sum_j W_i'' Q_i \left(\frac{1}{r} W_j' Q_j + \frac{1}{r^2} W_j Q_j'' \right) q_i \delta q_j \tag{4.65}$$
$$- \sum_i \sum_j \left(\frac{1}{r} W_i' - \frac{1}{r^2} W_i \right) \left(\frac{1}{r} W_j' - \frac{1}{r^2} W_j \right) Q_i' Q_j' \, q_i \delta q_j \Bigg) \Bigg] \, \mathrm{dA} \, .$$

Inserting the expansion (4.63) into the expression for work done by material damping (4.46) yields

$$\delta\mathcal{W}_d = -\int_{\mathrm{A}} d_S \sum_i \sum_j W_i Q_i W_j Q_j \, \dot{q}_i \, \delta q_j \, \mathrm{dA} \, . \tag{4.66}$$

Similarly, for the variation of the work done by contact force (4.62) follows

$$\delta\mathcal{W}_f = -\int_{\mathrm{A_C}} \Bigg[\sum_i \sum_j W_i Q_i W_j Q_j (k_f q_i + d_f \dot{q}_i) \delta q_j - n_0 \sum_j W_j Q_j \delta q_j$$
$$+ \left(\frac{h}{2} \right)^2 \frac{\mu \, n_0}{r|\Omega|} \left(\sum_i \sum_j \left(W_i' Q_i \dot{q}_i + \frac{\Omega}{r} W_i Q_i' q_i \right) W_j' Q_j \delta q_j \right) \tag{4.67}$$
$$+ \mu \frac{h}{2} \operatorname{sign} \Omega \left(\sum_i \sum_j W_i Q_i W_j Q_j' (k_f q_i + d_f \dot{q}_i) \delta q_j - n_0 \sum_j W_j Q_j' \delta q_j \right) \Bigg] \mathrm{dA_C} \, ,$$

in which only terms linear in q_i and $\dot{q}_i$ are taken into account. Further, collecting expressions according to Eq. (4.32) leads to a system of ordinary differential equations in the model coordinates q_i

$$\mathbf{M}\,\ddot{\mathbf{q}} + \mathbf{B}\,\dot{\mathbf{q}} + \mathbf{K}\,\mathbf{q} = \mathbf{f}, \tag{4.68}$$

where the elements of the matrices are

$$
\begin{aligned}
m_{ij} &= \int_{\mathrm{A}} \rho h\, W_i Q_i W_j Q_j \,\mathrm{dA},\\
b_{ij} &= \int_{\mathrm{A_C}} \left[d_f W_i Q_i W_j \Big(Q_j + \mu \frac{h}{2} Q_j' \operatorname{sign}\Omega \Big) + \frac{\mu h^2 n_0}{4r|\Omega|} W_i' Q_i W_j' Q_j \right] \mathrm{dA_C}\\
&\quad + \int_{\mathrm{A}} d_S\, W_i Q_i W_j Q_j \,\mathrm{dA}, \qquad (4.69)\\
c_{ij} &= \int_{\mathrm{A}} B \left[\Big(W_i'' Q_i + \frac{1}{r} W_i' Q_i + \frac{1}{r^2} W_i Q_i'' \Big) \Big(W_j'' Q_j + \frac{1}{r} W_j' Q_j + \frac{1}{r^2} W_j Q_j'' \Big) \right.\\
&\quad \left. - \frac{2(1-\nu)}{r^2} \Big(W_i'' Q_i \big(r W_j' Q_j + W_j Q_j'' \big) - (r W_i' - W_i) \big(r W_j' - W_j \big) \frac{Q_i' Q_j'}{r^2} \Big) \right] \mathrm{dA}\\
&\quad + \int_{\mathrm{A_C}} \left[k_f W_i Q_i W_j \Big(Q_j + \mu \frac{h}{2} Q_j' \operatorname{sign}\Omega \Big) + \mu \frac{h^2 n_0}{4r^2} W_i Q_i' W_j' Q_j \operatorname{sign}\Omega \right] \mathrm{dA_C}\,.
\end{aligned}
$$

The elements of the force vector $\mathbf{f}$ on the right-hand side are

$$
f_j = \int_{\mathrm{A_C}} n_0 \Big(W_j Q_j + \mu \frac{h}{2} \operatorname{sign}\Omega\, W_j Q_j' \Big) \mathrm{dA_C}\,, \qquad (4.70)
$$

where the pre-stress is denoted by $n_0 = k_f\,(h/2 + q_R)$.

According to the RITZ method, the shape functions W_i and Q_i have to fulfill the geometric boundary conditions. The stator shown in Fig. 4.1 is fixed at the inner radius r_i and free at the outer radius r_o. Therefore, for the geometric boundary conditions follows

$$
w(r_i, \varphi, t) = 0\,, \qquad w_{,r}(r_i, \varphi, t) = 0. \qquad (4.71)
$$

The natural boundary conditions at the outer radius r_o, given in [23], are

$$
\frac{\partial}{\partial r}(\Delta w) + \frac{1-\nu}{r^3}\,(r w_{,r\varphi\varphi} - w_{,\varphi\varphi}) = 0, \quad r^2 w_{,rr} + \nu\,(r w_{,r} + w_{,\varphi\varphi}) = 0. \qquad (4.72)
$$

where for the LAPLACE operator holds $\Delta = \frac{\partial^2}{\partial r^2} + \frac{1}{r}\frac{\partial}{\partial r} + \frac{1}{r^2}\frac{\partial^2}{\partial \varphi^2}$. Shape functions, which fulfill both boundary conditions (4.71) and (4.72) are

$$
W(r) = A_\kappa\, J_\kappa(\lambda r) + B_\kappa\, Y_\kappa(\lambda r) + C_\kappa\, I_\kappa(\lambda r) + D_\kappa\, K_\kappa(\lambda r), \qquad (4.73)
$$

$$
Q(\varphi) = \cos \kappa\varphi, \qquad \kappa = 0, 1, 2, \cdots\,, \qquad (4.74)
$$

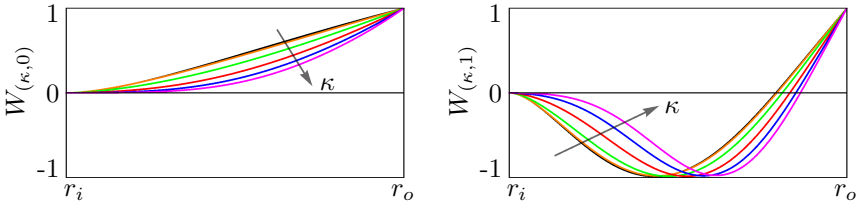

(a) Shape functions $W_{(\kappa,0)}$. **(b)** Shape functions $W_{(\kappa,1)}$.

Figure 4.4: Orthogonal shape functions in the radial direction.

where J_κ and Y_κ are BESSEL's function of 1st and 2nd order and I_κ, K_κ are the modified BESSEL's function of 1st and 2nd order. Inserting the expansion (4.63) into the boundary conditions (4.71), (4.72) leads to a system of linear homogeneous equations in the coefficients $A_\kappa, B_\kappa, C_\kappa$ and D_κ, which has only a non-trivial solution if the determinant of the equation matrix is zero. This leads to a characteristic polynomial which has for each κ an infinite number of roots λ. For each root $\lambda_{(\kappa,l)}$ the shape function is given by $W_{(\kappa,l)}(r)$. Figure 4.4 shows the radial shape functions $W_{(\kappa,0)}$ and $W_{(\kappa,1)}$ for $\kappa = 0, 1, \cdots, 5$. These shape functions are visualized in Fig. 4.5 together with the circumferential shape functions Q_i. Each mode shape is classified through

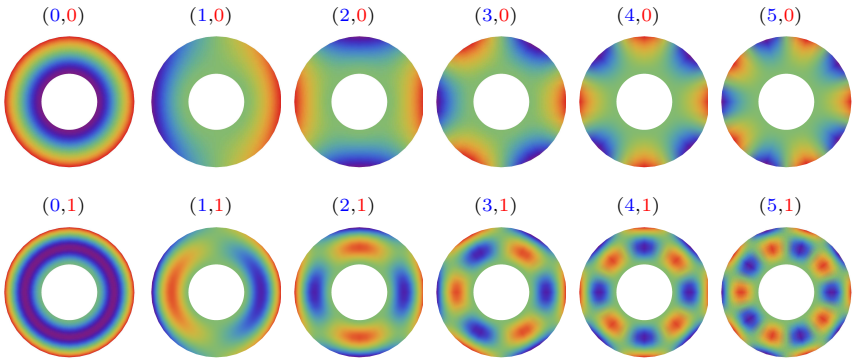

Figure 4.5: Mode shape classification (κ,l).

the wave number in circumferential direction κ and in the radial direction l, respectively. For $\kappa \geq 1$ double eigenfrequencies occur, due to symmetry of the plate. Consequently, to each double eigenfrequency belong two orthogonal mode shapes, which have a phase difference of $\pi/2\kappa$ in circumferential direction. Compared to the beam model, the $(\kappa, 0)$-modes of the plate are similar to the beam modes (4.38). In case of single modes ($\kappa = 0$, $Q_i = Q_j = 1$) the equations of motion are decoupled and have the form

$$
\begin{aligned}
& m_0\,\ddot{q}_0(t) + d_0\,\dot{q}_0(t) + k_0\,q_0(t) = f_0, \qquad \text{with} \\
& m_0 = \int_{\mathrm{A}} \rho h\, W_0^2 \,\mathrm{dA}, \qquad f_0 = \int_{\mathrm{A_C}} n_0 W_0 \,\mathrm{dA_C}, \\
& d_0 = \int_{\mathrm{A_C}} \left[d_f W_0^2 + \frac{\mu h^2 n_0}{4r|\Omega|} W_0'^2 \right] \mathrm{dA_C} + \int_{\mathrm{A}} d_S W_0^2 \,\mathrm{dA}, \\
& k_0 = \int_{\mathrm{A}} B \left[\left(W_0'' + \frac{1}{r} W_0' \right)^2 - \frac{2(1-\nu)}{r} W_0'' W_0' \right] \mathrm{dA} + \int_{\mathrm{A_C}} k_f W_0^2 \,\mathrm{dA_C}.
\end{aligned}
\tag{4.75}
$$

For modes with $\kappa \geq 1$ only mode pairs with the same wave number κ are coupled ($Q_i = \cos\kappa\varphi$, $Q_j = \sin\kappa\varphi$). The equations of motion for each mode pair are

$$
\mathbf{M}_\kappa\,\ddot{\mathbf{q}}_\kappa + (\mathbf{D}_\kappa + \mathbf{G}_\kappa)\,\dot{\mathbf{q}}_\kappa + (\mathbf{K}_\kappa + \mathbf{N}_\kappa)\,\mathbf{q}_\kappa = \mathbf{0}, \quad \text{with}
\tag{4.76}
$$

$$
\begin{aligned}
& \mathbf{M}_\kappa = m_\kappa \mathbf{I}, \quad \mathbf{D}_\kappa = d_\kappa \mathbf{I}, \quad \mathbf{G}_\kappa = g_\kappa \begin{bmatrix} 0 & -1 \\ 1 & 0 \end{bmatrix}, \quad \mathbf{K}_\kappa = k_\kappa \mathbf{I}, \quad \mathbf{N}_\kappa = n_\kappa \begin{bmatrix} 0 & -1 \\ 1 & 0 \end{bmatrix}, \\
& m_\kappa = \int_{r_i}^{r_o} \pi \rho h W_\kappa^2 \, r \,\mathrm{dr}, \\
& d_\kappa = \int_{r_i}^{r_o} \pi d_S W_\kappa^2 \, r \,\mathrm{dr} + \int_{r_m}^{r_o} \pi \left(d_f W_\kappa^2 + \frac{\mu\, h^2\, n_0}{4r\,|\Omega|} W_\kappa'^2 \right) r \,\mathrm{dr}, \\
& g_\kappa = \int_{r_m}^{r_o} \mu \frac{h}{2} \kappa \pi d_f \,\mathrm{sign}\,\Omega W_\kappa^2 \, r \,\mathrm{dr}, \\
& k_\kappa = \int_{r_i}^{r_o} \pi B\, \hat{k}_w r \,\mathrm{dr} + \int_{r_m}^{r_o} \pi k_f W_\kappa^2 \, r \,\mathrm{dr}, \\
& n_\kappa = \int_{r_m}^{r_o} \mu \frac{h}{2} \kappa \pi \,\mathrm{sign}\,\Omega \left(k_f W_\kappa^2 - \frac{h n_0}{2r^2} W_\kappa W_\kappa' \right) r \,\mathrm{dr}.
\end{aligned}
\tag{4.77}
$$

The abbreviation used for the coefficient k_κ is

$$\hat{k}_w = \left(W_\kappa'' + \frac{1}{r}W_\kappa' - \frac{\kappa^2}{r^2}W_\kappa\right)^2 - \frac{2(1-\nu)}{r^2}\left(W_\kappa''\left(rW_\kappa' - \kappa^2 W_\kappa\right) - \frac{\kappa^2}{r^2}\left(rW_\kappa' - W_\kappa\right)^2\right). \quad (4.78)$$

It is assumed that the neutral plane A is bounded by r_i, r_o and the contact area $\mathrm{A_C}$ by r_m, r_o. The structure of the matrices (4.76) is the same as for the beam model (4.41). The main difference in the matrix-element entries is that d_κ consists of an additional damping term due to COULOMB's friction. This effect results from the kinematics of the structure. Compared to the EULER-BERNOULLI beam, the KIRCHHOFF plate takes also into account deformation of the stator in radial direction.

4.1.3 Piezoelectric layer

The effect of the piezoceramic layer, which was neglected in the previous modeling, is considered in the following. To this end, the so-called extended HAMILTON's principle is used, applied by ERTURK and INMAN in [8] or NGUYEN in [36]. A derivation of the extended HAMILTON's principle is done by WOLF in [64]. Compared to the common version of the HAMILTON's principle in Eq. (4.1), the extended version consists of an additional term $\mathcal{W}_e$, which denotes the electric energy of the piezoceramic layer,

$$\delta \int_{t_1}^{t_2} (\mathcal{L} + \mathcal{W})\,\mathrm{dt} = 0\,, \quad \text{with} \quad \mathcal{L} = \mathcal{T} - \mathcal{U} + \mathcal{W}_e\,. \quad (4.79)$$

Basically, the kinetic energy $\mathcal{T}$ in the LAGRANGEian $\mathcal{L}$ consists of the kinetic energy of the stator $\mathcal{T}_S$ and the kinetic energy of the piezoceramic layer $\mathcal{T}_P$. Since the contribution of the thin piezoelectric layer to the inertia of the system is small, the kinetic energy of the piezoceramic layer is neglected ($\mathcal{T}_P = 0$). Besides the potential energy of the stator $\mathcal{U}_S$, the functional $\mathcal{U}$ consists also of the potential energy of the piezoceramic layer, which reads

$$\mathcal{U}_P = \frac{1}{2}\int_{V_P} \boldsymbol{\sigma}^{\mathrm{T}} \boldsymbol{\epsilon}\,\mathrm{dV}. \quad (4.80)$$

The stress tensor of the piezoceramic structure is denoted by $\boldsymbol{\sigma}$ and the strain tensor as $\boldsymbol{\epsilon}$, respectively. The electric energy $\mathcal{W}_e$ of the piezoceramic structure

is

$$\mathcal{W}_e = \frac{1}{2}\int_{V_P} \mathbf{E}^T\,\mathbf{D}\,\mathrm{dV}, \tag{4.81}$$

where $\mathbf{E}$ and $\mathbf{D}$ are the electric field and the electric displacement tensor.

The main deformation of the piezoceramic layer, which is attached at the bottom of the elastic stator, is the lengthening effect in the circumferential direction. Therefore, describing the piezoceramic layer by using Euler-Bernoulli beam theory is an appropriate modeling approach. Thus, the general expression for the potential energy of the piezoceramic reduces to

$$\mathcal{U}_P = \frac{1}{2}\int_{V_P} \sigma_{11}\,\epsilon_{11}\,\mathrm{dV}. \tag{4.82}$$

The 11-direction corresponds to the $\vec{e}_t$-direction in Fig. 4.6a. For the electric energy, only the potential difference of the upper to the lower surface of the piezoceramic layer is taken into account[2]. Therefore, the electric energy simplifies to

$$\mathcal{W}_e = \frac{1}{2}\int_{V_P} E_3\,D_3\,\mathrm{dV}. \tag{4.83}$$

Here, the 3-direction is equivalent to $\vec{e}_n$-direction, see Fig. 4.6a. The piezoelectric behavior of the ceramic structure is described by the constitutive equations, which are reduced to the d_{31}-effect,

$$\begin{bmatrix}\sigma_{11}\\ D_3\end{bmatrix} = \begin{bmatrix}E_P & -\gamma_{31}\\ \gamma_{31} & \nu_{31}\end{bmatrix}\begin{bmatrix}\epsilon_{11}\\ E_3\end{bmatrix}, \quad \nu_{31} = \varepsilon_{33} - d_{31}^2 E_P, \quad \gamma_{31} = d_{31} E_p, \tag{4.84}$$

where d_{31} is the piezoelectric constant, E_P Young's modulus and ε_{33} the permittivity of the piezoceramic. Inserting this expressions into Eqs. (4.82) and (4.83) yields

$$\mathcal{U}_P = \frac{1}{2}\int_{V_P} \left(E_P\,\epsilon_{11}^2 - \gamma_{31}\,E_3\,\epsilon_{11}\right)\mathrm{dV}, \tag{4.85}$$

$$\mathcal{W}_e = \frac{1}{2}\int_{V_P} \left(\nu_{31} E_3^2 + \gamma_{31}\,\epsilon_{11}\,E_3\right)\mathrm{dV}. \tag{4.86}$$

[2] In the literature this is also referred to as the so-called d_{31}-effect.

The relation for ϵ_{11} and E_3 can be derived by taking into account the mechanical as well as the electric boundary conditions of the piezoceramic. Assuming that the thickness of the piezoceramic layer is much smaller than the thickness of the stator ($h_P \ll h$), the strain and the electric field can be approximated by

$$\epsilon_{11} = z\, w''(x,t), \qquad E_3 = \frac{v(x,t)}{h_P}, \tag{4.87}$$

where z is the coordinate in $\vec{e}_n$-direction and v the electric potential at the corresponding electrode output. It should be pointed out that the assumption of constant electric field in the 3-direction does not fulfill the electromechanical boundary conditions. Nevertheless, the resulting error done by this approximation is negligible for $h_P \ll h$, according to MARINKOVIC in [31]. Moreover, this simplification was used by SATTEL in [45], in order to describe the motor characteristics of a similar ultrasonic motor. The experimental results were in good agreement with the simplified model used. However, a detailed modeling of a piezoelectric layer attached to the stator of an traveling wave ultrasonic motor is given by WOLF in [64]. Inserting the simplified relations (4.87) into Eqs. (4.85) and (4.86) and carrying out the variation yields

$$\mathcal{U}_P = \int_0^\ell \left[E_P\, I_P w'' \delta w'' + \frac{1}{2}\gamma_{31}\frac{h}{2} b_P \left(w''\delta v + v\,\delta w'' \right) \right] \mathrm{dx}, \tag{4.88}$$

$$\mathcal{W}_e = \int_0^\ell \left[\nu_{31}\frac{b_P}{h_P} v\,\delta v - \frac{1}{2}\gamma_{31}\frac{h}{2} b_P \left(w''\delta v + v\,\delta w'' \right) \right] \mathrm{dx}. \tag{4.89}$$

The length of the piezoceramic layer in radial direction is b_P and the second moment of area is given by $I_P = (h^2/4) h_P b_P$. According to Fig. 4.6a, the integration boundaries used for the z-direction are $[-h/2 - h_P, -h/2]$. Figure 4.6b shows a detailed cross section of the stator together with the piezoceramic layer. In the modeling, the height of the contact teeth h_t was neglected due to simplicity. Moreover, in the beam model of the stator an averaged radius, defined as $r = (r_o + r_m)/2$, was used.

Using the expansion (4.27) together with the shape functions for the elastic ring (4.38) leads to following extension of the linearized system for each mode

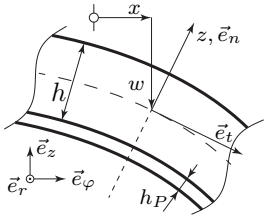

(a) Stator kinematics with piezoceramic layer attached.

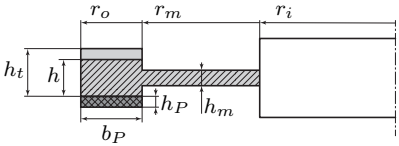

(b) Cross section of the traveling wave generator: stator (right-hatched), piezoceramic layer (cross-hatched).

Figure 4.6: Kinematics and cross section of the stator with piezoceramic layer.

pair (Eq. (4.41)),

$$\mathbf{M}_\kappa\,\ddot{\mathbf{q}}_\kappa(t) + (\mathbf{D}_\kappa + \mathbf{G}_\kappa)\,\dot{\mathbf{q}}_\kappa(t) + \left(\mathbf{K}_\kappa + \mathbf{K}_\kappa^P + \mathbf{N}_\kappa\right)\mathbf{q}_\kappa(t) = \mathbf{f}_v, \tag{4.90}$$

with

$$\mathbf{K}_\kappa^P = \pi\kappa^4 \frac{E_P I_P}{r^3}\,\mathbf{I}, \quad \mathbf{f}_v = \gamma_{31}\kappa^2 \frac{h}{2} b_P r \begin{bmatrix} \sum_\zeta \int_{\varphi_\zeta} v_\zeta(t) \sin\kappa\varphi \,\mathrm{d}\varphi \\ \sum_\zeta \int_{\varphi_\zeta} v_\zeta(t) \cos\kappa\varphi \,\mathrm{d}\varphi \end{bmatrix}. \tag{4.91}$$

Through the additional matrix $\mathbf{K}_\kappa^P$ the stiffness of the stator increases. The terms on the right-hand side ($\mathbf{f}_v$) result from the piezoelectric effect, which depends on the specific electrode configuration. It is assumed that the surface of the piezoceramic layer is divided into ζ electrodes with the electric potential v_ζ and the integration angle φ_ζ. Under consideration of the polarization direction the integrals in $\mathbf{f}_v$ simplify to

$$\int_{\varphi_\zeta} v_\zeta(t) \sin\kappa\varphi \,\mathrm{d}\varphi = \Psi_\zeta^s\, v_\zeta(t), \quad \int_{\varphi_\zeta} v_\zeta(t) \cos\kappa\varphi \,\mathrm{d}\varphi = \Psi_\zeta^c\, v_\zeta(t), \tag{4.92}$$

where Ψ_ζ^s and Ψ_ζ^c describe the coupling, depending on the geometric properties of each electrode. The electric circuit equations for each electrode are

$$C_\zeta\,\dot{v}_\zeta(t) + \frac{1}{R_\zeta} v_\zeta(t) - \gamma_{31}\kappa^2 \frac{h}{2} b_P r \int_{\varphi_\zeta} \sum_i W_i\,\dot{q}_i \,\mathrm{d}\varphi = 0, \tag{4.93}$$

with the electric capacity $C_\zeta = \nu_{31}(b_P/h_P)\varphi_\zeta r$. The influence of the modal coordinate q_i on the electric potential v_ζ depends on the shape function W_i of

the corresponding mode as well as on the configuration of the electrode, such as geometry and polarization direction. Assuming harmonic oscillations of the modal coordinates of the stator q_i in the steady state, allows to use transfer functions to describe the steady state response of the electric coordinates v_ζ. Thereby, the electric resistance R_ζ, maximizing the electric power output, can be determined. For oscillations with the frequency Ω_w and the amplitude $\hat{q}$ for the maximum power output and the corresponding optimum resistance for the electrode ζ follows

$$P_{\mathrm{eff},\zeta}^{\max} = \frac{\hat{q}^2}{2}\frac{\Gamma_\zeta^2 \Omega_w}{2\,C_\zeta}, \quad R_\zeta^* = \frac{1}{\Omega_w C_\zeta}, \quad \text{with} \quad \Gamma_\zeta = \gamma_{31}\kappa^2 \frac{h}{2} b_P r \int_{\varphi_\zeta} W_i \,\mathrm{d}\varphi. \tag{4.94}$$

The optimum resistance R_ζ^* depends only on the oscillation frequency Ω_w and the effective capacity of the piezoceramic. For a constant Ω_w, which is expected in the steady-state of a specific mode, the optimum resistance is independent of any excitation parameters.

4.2 Initiation of self-excited vibrations

The goal of this section is to analyze the stability behavior of the trivial solution of the traveling wave generator in order to make a prediction when self-excited vibrations can occur. For the stability analysis it is assumed that the matrices have constant coefficients, which is the case for a constant rotation speed of the rotor.

4.2.1 Stability behavior of the trivial solution

In the following, the initiation of self-excited vibrations of the traveling wave generator is analyzed based on the linearized equations of motion given in Eq. (4.76) (KIRCHHOFF plate theory). Since each mode pair is decoupled, the stability behavior of the trivial solution can be analyzed separately. According to the ROUTH-HURWITZ stability criterion, the instability condition is

$$\left(d_\kappa^2 + g_\kappa^2\right)\left(d_\kappa^2\, k_\kappa + d_\kappa\, g_\kappa\, n_\kappa - m_\kappa\, n_\kappa^2\right) < 0\,. \tag{4.95}$$

For a negligible gyroscopic effect the instability condition simplifies to

$$d_\kappa^2\,\omega_\kappa^2 - n_\kappa^2 < 0\,, \quad \text{with} \quad \omega_\kappa^2 = \frac{k_\kappa}{m_\kappa}\,. \tag{4.96}$$

By inserting the coefficients (4.77) the critical parameters can be obtained in the same way as in section 3.2. The qualitative influence of the main parameters on the stability behavior is equivalent to the wobbling disk generator studied before. Based on the inequality (4.96) estimates for the stability boundary for each mode can be determined. The stability boundary of different modes of the traveling wave generator is compared in the following.

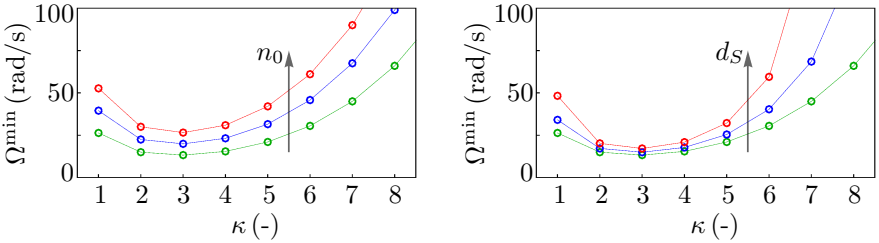

(a) Variation of the pre-stress n_0.

(b) Variation of damping d_S.

Figure 4.7: Minimum rotation speed $\Omega^{\min}$ needed for self-excitation: Comparison for different mode shapes (wave number in circumferential direction is κ).

In Figure 4.7 the minimum rotation speed needed for destabilization of the trivial solution is plotted for different modes. The paramaters used are summarized in Tab. 4.1. One can observe that $\Omega^{\min}$ has the lowest value for the mode with the wave number $\kappa = 3$. For the other modes, self-excited vibrations occur for higher rotation speeds. This phenomena occurs due to the different influence of the non-conservative circulatory terms n_κ on each mode. Increasing the pre-stress n_0 or the material damping d_S has a stabilizing effect, similarly to the results for the wobbling disk generator. The calculation of the characteristic wave number κ^*, for which the stability boundary is minimized, is analytically not possible due to the unavoidable numerical evaluation of the BESSEL functions for the mode shapes W_i. However, using the much simpler

Table 4.1: Parameters of the traveling wave generator.

	parameter	symbol	value	unit
friction-layer	friction coefficient	μ	0.4	–
	stiffness coefficient	k_f	$1{\cdot}10^{10}$	N/m
	damping coefficient	d_f	10^{-6}	Ns/m
stator	mass density	ρ	8500	kg/m^3
	YOUNG's modulus	E	$0.9 \cdot 10^{11}$	N/m^2
	POISSON's ratio	ν	0.37	–
	material damping	d_S	$1 \cdot 10^{-3}$	Ns/m
	height	h	$4 \cdot 10^{-3}$	m
	teeth height	h_t	$5 \cdot 10^{-3}$	m
	inner plate height	h_m	$3 \cdot 10^{-3}$	m
	outer radius	r_o	$2.8 \cdot 10^{-2}$	m
	inner radius	r_i	$1.7 \cdot 10^{-2}$	m
	inner plate radius	r_m	$2 \cdot 10^{-2}$	m
piezoceramic	width	b_P	$1 \cdot 10^{-2}$	m
	height	h_P	$1 \cdot 10^{-3}$	m
	YOUNG's modulus	E_P	$9 \cdot 10^{10}$	N/m^2
	piezoelectric constant	d_{31}	$-1.27{\cdot}10^{-10}$	m/V
	permittivity	ε_{33}	$1{\cdot}10^{-8}$	F/m
	coupling factor	$\gamma_{31} = d_{31}\, E_P$	-11.43	N/Vm
	effective permittivity	$\nu_{31} = \varepsilon_{33} - d_{31}^2 E_P$	$8.55{\cdot}10^{-9}$	F/m

beam model (4.41) an approximation for the characteristic wave number κ^* can be given. To this end, the critical damping of each mode is defined as

$$d_\kappa^{\text{crit}} := \frac{n_\kappa}{\omega_\kappa} = \frac{\mu\pi\frac{h}{2}k_f\kappa\sqrt{r\rho A}}{\sqrt{r(k_S+k_f)+\kappa^4\dfrac{EI}{r^3}}}, \tag{4.97}$$

where the coefficients of the beam model (4.42) were used. The critical damp-

ing d_κ^{crit} reaches its minimum for

$$\kappa^* = r \sqrt[4]{\frac{k_S + k_f}{3EI}}. \tag{4.98}$$

Although this is a rough approximation, it indicates the general dependencies of the system parameters on κ^*.

4.2.2 Finite element analysis

In this section, the stability of the trivial solution of the elastic stator is analyzed using numerical tools. The numerical stability analysis is based on the Complex Eigenvalue Analysis (CEA). A description of this finite element procedure is given in section 3.2.2.

Finite element model

The geometry of the elastic stator is based on the sketch given in Fig. 4.6b, where a simplified mesh is used for vizualization. For simplicity the contact teeth and the piezoceramic layer were neglected, leading to the finite element model shown in Fig. 4.8. In the analysis, the stator is clamped at the inner radius and free at the outer radius. The rotor, which is not shown here, is pressed against the stator and has a constant rotation speed around the vertical axis. Moreover, COULOMB's law of friction is assumed in the contact zone between the stator and the rotor.

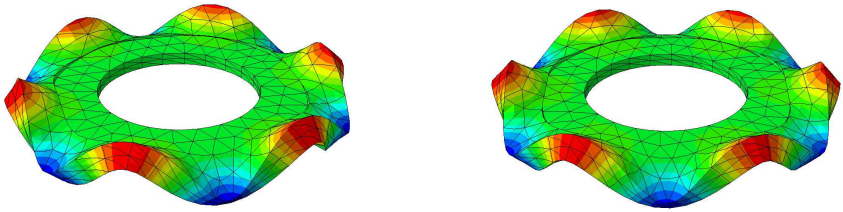

(a) $(6,0)_{\text{s}}$-mode. **(b)** $(6,0)_{\text{c}}$-mode.

Figure 4.8: Numerical solution for the $(6,0)$-mode of the stator.

Stability analysis using ABAQUS

In the following, numerical results obtained from CEA in ABAQUS are discussed with respect to initiation of self-excited vibrations. The parameters used are given in Tab. 4.1. In addition, mass and stiffness proportional damping was assumed (Tab. 4.2). For the calculation $5{\cdot}10^5$ DOF and tetrahedral elements are used. The analyzed steady state of the stator-rotor system is described by the pre-stress displacement s_0 and the rotation speed f_R. Figure 4.9a shows the numerical results for the minimum rotation speed needed to destabilize the specific mode (wave number κ). One observes that $f_R^{\min}$ has the lowest value for the mode with the wave number $\kappa = 6$. This phenomenon is similar to the analytical results shown in Fig. 4.7, where the wave number of this specific mode is lower. Furthermore, increasing the pre-stress through the rotor displacement s_0 has a stabilizing effect, which is in

Table 4.2: Damping parameters of the finite element model.

parameter	symbol	value	unit
mass-proportional damping	α	0	1/s
siffness-proportional damping	β	10^{-7}	s

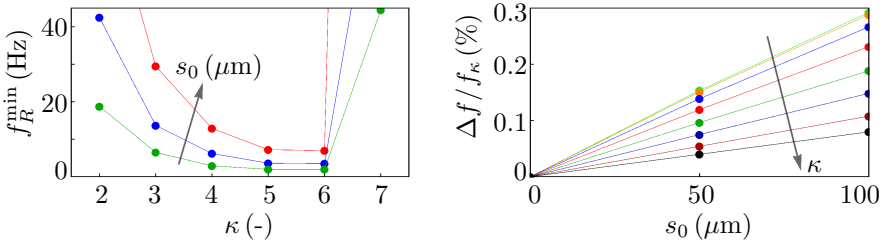

(a) Minimum rotation speed over mode shapes: varying pre-stress.

(b) Perturbation of the natural frequencies due to pre-stress s_0.

Figure 4.9: Results from complex eigenvalue analysis (CEA, Abaqus).

agreement with the analytical results. Figure 4.9b shows the influence of the pre-stress on the natural frequencies of the stator. The perturbation of the natural frequencies is in general negligible ($< 0.3\%$) and decreases for an increasing wave number κ. Basically, the finite element analysis shows that modes $W_{(\kappa,l)}$ with $l = 0$, which lie in the lower frequency range, can be destabilized in the analyzed excitation range. Due to the geometry of the stator ($r_i \approx r_o/2$), mode shapes with $l \geq 1$ have a relatively high natural frequencies and cannot be destabilized in the simulated operation range. Therefore, an order reduction to the modes $W_{(\kappa,0)}$, which are similar to the mode shapes of the elastic ring, is justified in this case.

4.3 Bifurcation and steady-state operation

In the following, the steady-state characteristics of the traveling wave generator is analyzed based on the elastic ring model described in section 4.1.1. Since the exact contact kinematics between the stator and the rotor is very complex and difficult to describe, different assumptions are made for the steady-state motion, in order to derive simplified models. For an ultrasonic traveling wave motor a similar contact problem is studied in detail by Sattel et al. in [46], where stick and slip regions in the contact zone are taken into account. Clearly, the assumption of sliding in the stator-rotor contact is justified in the analysis of the initiation of self-excited vibrations. For a steady-state motion this assumption can be violated due to partially separation of the contact partners and/or due to the occurrence of stiction zones, which are relevant for relatively high amplitudes. Consequently, the analysis is divided into two parts: First, the bifurcation behavior of the generator is studied based on the assumption of sliding friction in the contact zone, which is justified in the vicinity of the trivial solution. The second part deals with the characteristic behavior of the generator for an adhesive contact, which is equivalent to a stiction (or 'rolling') assumption regarding the interaction between the rotor and the highest material points of the stator.

4.3.1 Sliding in the contact zone

In this section, the derived nonlinear equations of motion based on the assumption of sliding friction in the contact zone between the stator and the rotor (Eq. (4.31)) are analyzed numerically. In section 4.2.1, where the initiation of self-excited vibrations is analyzed, a result is that the rotation speed of the rotor (Ω) contributes to the additional system damping caused by friction. For an increasing rotation speed, the additional damping effect vanishes, see Eq. (4.77). Since this effect in not present in the model, where the stator is

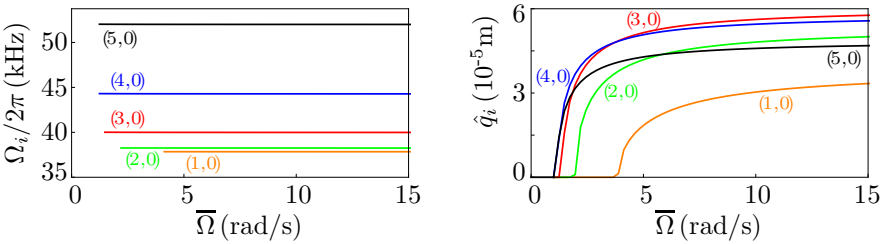

(a) Limit-cycle frequency Ω_i.

(b) Limit-cycle amplitude $\hat{q}_i$.

Figure 4.10: Bifurcation diagram of the traveling wave generator (described by the elastic ring model, Eq. (4.31)).

treated as an elastic ring, an equivalent rotation speed is introduced, which is proportional to the reciprocal of the system damping ($\overline{\Omega} \propto 1/d$). Through this modification the results based on the simple elastic ring model can be qualitatively compared to the experiments discussed in section 6.3. The numerical results for the steady-state solutions of the generator are shown in Fig. 4.10. For the sake of simplicity, only the first five modes are taken into account. It can be observed that after the bifurcation point, self-excited oscillations with a non-zero amplitude occur. Bifurcation occurs for the $(5,0)$-mode at the lowest and for the $(1,0)$-mode at the highest value of Ω. This is equivalent to the results for the minimum necessary rotation speed for self-excitation shown in Fig. 4.7. The frequency of each steady-state oscillation is displayed in Fig. 4.10a. Similarly to the steady-state characteristics of the wobbling disk generator, the frequency of each mode corresponds to the natural frequency

of the stator and is independent of the rotation speed. The amplitude of each limit cycle increases with the rotation speed, see Fig. 4.10b. These results show that in the region, where many modes can become unstable, also many steady-state solutions are possible. In order to determine the circumstances when a specific mode is 'active' a more accurate model is required, taking into account different contact phenomena.

4.3.2 Adhesive contact

The assumption of sliding in the contact zone, used in the previous section, is only valid for steady-state motion with a relatively small amplitude, where no separations occur. Furthermore, analytical investigations of the steady-state motion show that the slip between the rotor and the highest points of the traveling wave approaches zero (Fig. 4.11). This motivates the investigation of the generator characteristics assuming an adhesive contact, which implies that the rotor is only in contact with the highest material points of the stator. The number of contact points depends on the form of the resulting vibrations of the stator. This simplified kinematics are shown in Fig. 4.11 for a single contact point S_{C_j}. For each contact point the velocities of the corresponding material points of the rotor and the stator were derived in section 4.1.1. The relative velocity between these two material points is

$$\begin{aligned} \Delta\vec{v} &= {}^{S_C}\vec{v}^{\mathcal{N}} - {}^{R_C}\vec{v}^{\mathcal{N}} = \Delta v_r\,\vec{e}_r + \Delta v_\varphi\,\vec{e}_\varphi, \quad \text{with} \\ \Delta v_r &= \Omega\frac{h}{2}\frac{w_{,\varphi}}{\sqrt{r^2+w_{,\varphi}^2}}, \qquad \Delta v_\varphi = \frac{h}{2}\frac{r^2\dot{w}_{,\varphi}}{\left(r^2+w_{,\varphi}^2\right)^{\frac{3}{2}}} - \Omega\, r. \end{aligned} \tag{4.99}$$

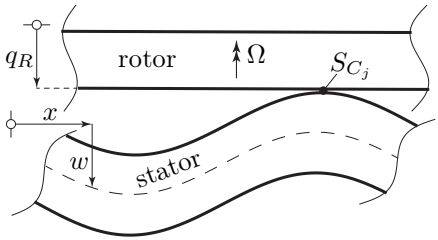

Figure 4.11: Simplified kinematics of the stator-rotor contact (traveling wave generator).

The deflection of the stator can be described in the steady state as a traveling wave

$$w^*(\varphi,t) = \hat{w}\sin\kappa\varphi\cos\Omega_\kappa t - \hat{w}\cos\kappa\varphi\sin\Omega_\kappa t = \hat{w}\sin(\kappa\varphi - \Omega_\kappa t). \tag{4.100}$$

The characteristic parameters of the traveling wave are the amplitude $\hat{w}$, the wave number κ and the frequency Ω_κ. The highest points of the traveling wave (S_{C_j}) have the circumferential coordinate

$$\varphi_j = \frac{\frac{\pi}{2} + (j-1)\pi + \Omega_\kappa t}{\kappa} \quad \text{for} \quad j = 1, 2, \cdots . \tag{4.101}$$

Inserting φ_j into the expression for the traveling wave (4.100) yields

$$w^*(\varphi_j,t) = \hat{w}, \qquad w^*_{,\varphi}(\varphi_j,t) = 0, \qquad \dot{w}^*_{,\varphi}(\varphi_j,t) = \hat{w}\,\kappa\,\Omega_\kappa. \tag{4.102}$$

For the highest points of the stator (S_{C_j}) the adhesive contact kinematics implies that the relative velocity of the contact partners vanishes. Applying this kinematic constraint on the expression for $\Delta\vec{v}$ (4.99) leads to

$$0 = \Omega\frac{h}{2}\frac{w_{,\varphi}}{\sqrt{r^2 + w^2_{,\varphi}}}, \qquad 0 = \frac{h}{2}\frac{r^2\dot{w}_{,\varphi}}{\left(r^2 + w^2_{,\varphi}\right)^{\frac{3}{2}}} - \Omega\, r. \tag{4.103}$$

For the traveling wave, described by the relations in Eq. (4.102), this kinematic constraints are fulfilled for

$$\hat{w} = \frac{r^2}{\frac{h}{2}\kappa}\frac{\Omega}{\Omega_\kappa}. \tag{4.104}$$

Furthermore, assuming an adhesive contact between the stator and the rotor leads in the steady state to the operation-mode frequency

$$\Omega^2_\kappa = \frac{\pi r(k_S + k_f) + \pi\kappa^4\dfrac{EI}{r^3} + 2\pi r k_R}{\pi r\rho A}. \tag{4.105}$$

This relations for the amplitude and the frequency of the traveling wave are identical to the expressions derived for the wobbling disk generator, see Eq. (3.137). In the steady state, the frequency of the traveling wave corresponds to the natural eigenfrequency of the mode and the amplitude of the

motion increases linearly with the rotation speed Ω. The independence of the operation mode frequency on the rotation speed was already observed in case of sliding friction in the contact zone, see Fig. 4.10a. According to the Eq. (4.104), the amplitude of the steady-state motion is lower for a higher natural frequency Ω_κ. It is difficult to compare this characteristics to the case of sliding in the contact zone. In this case, the amplitude characteristics of the different modes strongly depends on the bifurcation point, see Fig. 4.10b. It can be observed for relatively high $\overline{\Omega}$ that the lower the mode the higher the slope. This characteristics corresponds to the one obtained for the adhesive contact. In order to validate the analytically derived characteristics, experiments were carried out for the traveling wave generator, the results of which are discussed in section 6.3.

5 Estimation of stability behavior and basins of attraction

In this chapter, two methods for the analysis of dynamical systems are proposed. First, the stability behavior of time-variant systems is considered. In case of the ultrasonic generators, the stability behavior of different types solutions has to be determined. For the operation as a generator, the trivial solution is to be destabilized and the resulting limit cycle is to be stabilized. The stability is analyzed based on the equations of motion linearized around the considered solution. In general, the linearization around a limt cycle solution leads to a time-variant system. In case of the trivial solution, the analysis method depends on the time behavior of the system coefficients. For constant coefficients, the stability behavior is determined by the eigenvalues of the linearized system. If the parameters, such as the rotation speed or the prestress of the rotor change periodically[1] with time, the stability behavior can be determined using FLOQUET theory, described in [13, 58]. Therefore, the so-called monodromy matrix has to be calculated using numerical methods, which can be very time-consuming. Alternatively, perturbation methods can be used to approximate the stability boundary [13, 34, 35, 58]. For system with non-periodic coefficients, no closed-form stability theory exists. Hence, a semi-analytic approach is introduced, which allows the approximate stability analysis of different types of non-autonomous differential equations. Thereby, the stability of the steady-state motion of the wobbling disk generator, which leads to the analysis of a non-periodic system, can be analyzed.

Besides the stability properties of a steady state solution, also their basins (or domains) of attraction are very important, since they give an estimate

[1] For applications, where the kinetic energy is harvested from structural vibrations, a transformation into angular motion (Fig. 1.3) leads to a periodic change of the rotating direction of the rotor and therefore to a system with periodic coefficients.

about the robustness of a stable solution against different types of perturbations. It is clear that a stable solution with an infinitely small basin of attraction cannot be observed in real life, since it is practically unstable. A useful approach to determine the basin of attraction of a stable trivial solution is LYAPUNOV's direct method [2, 13, 58]. For the construction of the LYAPUNOV function, which is required for the estimation of the basin of attraction, no general theory exists. The complexity of the construction methods proposed in the literature vary a lot and often numerical procedures are required [19, 57, 65]. Here, the CARLEMAN linearization method is used to construct an appropriate LYAPUNOV function. Since this is an analytical procedure, the parameter dependence on the basin of attraction can be studied in an efficient way.

5.1 Stability analysis of time-variant systems

In the following, a method for the stability analysis of time-variant ordinary differential equations is proposed. The procedure is based on the embedding of the non-autonomous ordinary differential equation into an autonomous partial differential equation, allowing the use of the GALERKIN discretization method.

5.1.1 Embedding technique

First, the idea of the embedding technique is introduced based on a system with a single degree of freedom. Afterwards, the extension to a multiple degree of freedom system is given. The obtained results are compared to numerical simulation and if available also to references in the literature.

Single degree of freedom

A non-autonomous ordinary differential equation of the form

$$\ddot{y} + b(t)\dot{y} + a(t)y = 0, \quad \text{with} \quad y = y(t), \tag{5.1}$$

is considered as a subsystem of the autonomous partial differential equation

$$\ddot{y} + 2\,\dot{y}' + y'' + b(x)(\dot{y} + y') + a(x)y = 0, \quad \text{with} \quad y = y(x,t). \tag{5.2}$$

Setting in the partial differential equation (5.2) $x = t$ the partial derivatives with respect to x vanish and the form (5.1) is obtained. Considering this special solution of the generalized partial differential equation significantly reduces the solution space. The advantage of embedding the ordinary differential equation into a partial differential equation is, on the one hand that the time-dependence of the coefficients $b(t)$ and $a(t)$ is transformed into a dependence on the new variable x. Thereby, the partial differential equation is considered as an autonomous system. On the other hand, the analysis methods for partial differential equations can be used, such as the GALERKIN method [14]. According to the GALERKIN procedure the solution of the partial differential equation (5.2) can be expanded into

$$y(x,t) = \sum_{i}^{N} w_i(x)\, q_i(t), \tag{5.3}$$

where $w_i(x)$ and $q_i(t)$ are the shape functions and the modal coordinates. Inserting this expansion into Eq. (5.2) yields

$$\sum_{i}^{N} w_i\, \ddot{q}_i + \sum_{i}^{N} (2w_i' + b\, w_i)\dot{q}_i + \sum_{i}^{N} (w_i'' + b\, w_i' + a\, w_i) q_i = 0. \tag{5.4}$$

Clearly, the expansion (5.3) can be also inserted directly into the ordinary differential equation (5.1) by taking into account the time-dependence of the variable x ($x = t, \dot{x} = 1$). This leads to the same expression as stated in Eq. (5.4). Multiplying Eq. (5.4) with $\sum_j^N w_j(x)$ and integrating over a characteristic interval $[0, T]$ yields

$$\boldsymbol{\mathcal{M}}\, \ddot{\mathbf{q}} + \boldsymbol{\mathcal{B}}\, \dot{\mathbf{q}} + \boldsymbol{\mathcal{C}}\, \mathbf{q} = \mathbf{0}, \qquad \mathbf{q}^{\mathrm{T}} = [q_1(t), q_2(t), \cdots, q_N(t)]\,, \tag{5.5}$$

with the matrix coefficients

$$\begin{aligned} \mathcal{M}_{ij} &= \int_0^T w_i(x) w_j(x)\, \mathrm{dx}, \\ \mathcal{B}_{ij} &= \int_0^T [2w_i'(x) + b(x) w_i(x)]\, w_j(x)\, \mathrm{dx}, \\ \mathcal{C}_{ij} &= \int_0^T [w_i''(x) + b(x) w_i'(x) + a(x) w_i(x)]\, w_j(x)\, \mathrm{dx}. \end{aligned} \tag{5.6}$$

Through the GALERKIN-type projection onto the modal coordinates q_i, the non-autonomous ordinary differential equation (5.1) is transformed into an autonomous odinary differential equation of a much higher order (5.5). The stability of this system is determined by the real parts of the eigenvalues, for the calculation of which different methods are available. For large matrices, which result from a high number of shape functions, an efficient eigenvalue solver algorithm is required. For example the LANCZOS algorithm, which is implemented in the most finite element tools, can be used. Through this embedding and discretization procedure the stability analysis of a non-autonomous ordinary differential equation was reduced to a simple eigenvalue problem of a relatively high order, which depends on the number of *ansatz* functions used.

Periodic and quasi-periodic MATHIEU equation

In order to highlight the main aspects regarding the *embedding technique*, two well-known examples from the literature considering time-variant systems is analyzed in the following. The first system is a periodically excited linear oscillator, with dynamics described by the MATHIEU equation, studied for example in [13, 58]. The stability behavior for such linear time-periodic systems can be determined using FLOQUET theory, described in [13, 58]. The second system considered, is described by the quasi-periodic MATHIEU equation, which compared to the common MATHIEU equation has two incommensurable frequencies. For systems of this type no closed-form stability theory exists and it therefore requires different analysis methods, such as numerical or perturbation methods. In this way, the stability analysis of the quasi-periodic MATHIEU equation was analyzed in detail by RAND et.al. in [1, 41, 42].

The quasi-periodic MATHIEU equation reads

$$\ddot{y}(t) + \epsilon\,\dot{y}(t) + \delta^2\Big(1 + \frac{\eta}{2}\,(\cos t + \cos \alpha t)\Big)\,y(t) = 0, \tag{5.7}$$

where the two incommensurable frequencies are normed to 1 and α. By setting $\alpha = 1$, the periodic form of the MATHIEU equation is obtained,

$$\ddot{y}(t) + \epsilon\,\dot{y}(t) + \delta^2(1 + \eta\cos t)\,y(t) = 0. \tag{5.8}$$

In case of the periodic MATHIEU equation, the coefficients of the partial differential equation (5.2) are

$$b(x) = \epsilon \quad \text{and} \quad a(x) = \delta^2(1 + \eta\cos x)\,, \tag{5.9}$$

and the shape functions $w_i(x)$, which fulfill the periodic boundary conditions

$$y(0,t) = y(T,t), \qquad y'(0,t) = y'(T,t), \quad \text{with} \quad T = 2\pi, \tag{5.10}$$

are

$$\mathbf{w}(x) = \begin{bmatrix} 1 & \sin x & \cos x & \sin 2x & \cos 2x & \cdots \end{bmatrix}^{\mathrm{T}}. \tag{5.11}$$

Using the coefficients (5.9) and the shape functions (5.11), an autonomous system of ordinary differential equations of the form (5.5) is obtained. Since harmonic functions are used as shape functions, the integrals (5.6), required for the generation of the autonomous system (5.5), can be evaluated analytically for an arbitrary characteristic interval T. The stability map obtained by applying this *embedding technique* on the periodic MATHIEU equation (5.8) is displayed in Fig. 5.1. The regions denoted as *stable* and *unstable* correspond

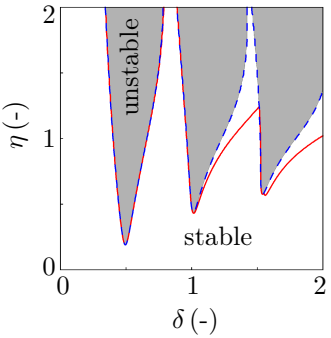

Figure 5.1: Stability map of the MATHIEU equation (5.8) for $\epsilon = 0.05$. Shape functions up to: $\kappa = 3$ (solid, red), $\kappa = 7$ (dashed, blue).

to the exact stability map, determined using FLOQUET theory. The stability boundary is compared to the results by the *embedding technique* with shape functions up to the wave number $\kappa = 3$ and $\kappa = 7$. The latter one leads to an estimate matching precisely the exact stability boundary. For less shape

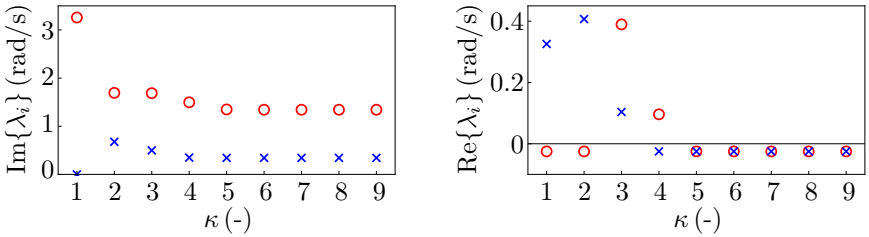

(a) Imaginary part of the eigenvalues. **(b)** Real part of the eigenvalues.

Figure 5.2: Convergency of the critical eigenvalues (λ_1: cross, λ_2: circle) over the wave number κ for $\delta = 1.4, \eta = 1.2$ (shape functions up to κ are considered).

functions, the estimate of the stability boundary deviates for larger δ from the exact boundary. The imaginary and real part of the critical eigenvalue are plotted in Fig. 5.2, showing the convergency behavior of the eigenvalues over the number of shape functions[2]. For the chosen parameters the imaginary and real part of the critical eigenvalues converge for $\kappa = 5$. This is the reason for the difference between the stability boundaries shown in Fig. 5.1. It can be concluded that only the converged eigenvalue of the expanded system of ordinary differential equations (5.5) can be taken into account in order to determine the stability behavior.

In case of the quasi-periodic MATHIEU equation (5.7) for the coefficients of the partial differential equation (5.2) follows

$$b(x) = \epsilon \quad \text{and} \quad a(x) = \delta^2 \left(1 + \frac{\eta}{2} \left(\cos x + \cos \alpha x\right)\right). \tag{5.12}$$

The shape functions $w_i(x)$ have to fulfill the boundary conditions

$$y(0,t) = y(T,t), \qquad y'(0,t) = y'(T,t), \tag{5.13}$$

where the characteristic interval T is infinite, since the system is subject to two incommensurable fundamental frequencies. The corresponding shape

[2] For each wave number $\kappa \geq 1$ two harmonic functions, $\sin \kappa x$ and $\cos \kappa x$, are added to the vector of shape functions $\mathbf{w}$.

functions are

$$\mathbf{w}(x) = \begin{bmatrix} 1 & \cdots & \sin\kappa x & \cos\kappa x & \cdots \end{bmatrix}^{\mathrm{T}}, \tag{5.14}$$

where the wave number κ is defined up to the expansion order N_i, according to Tab. 5.1. Since the FLOQUET theory does not hold for this type of systems,

Table 5.1: Wave number κ of the shape functions (5.14) for the quasi-periodic case.

	N_1	N_2	N_3	$\cdots$
multiple of the fundamental frequencies	1 α	2 2α	3 3α	$\cdots$
combination of the fundamental frequencies		$1+\alpha$ $1-\alpha$	$1+2\alpha$ $1-2\alpha$ $2+\alpha$ $2-\alpha$	$\cdots$

the stability behavior was determined by numerical means by RAND et.al in [42], shown in Fig. 5.3a (colors are modified for better comparison). The stability map therein is used as reference and shows excellent agreement with the stability map in Fig. 5.3b. In addition, RAND examined in [41] the stability behavior using perturbation methods. While, the map in Fig. 5.3a is obtained by time-consuming numerical simulation, our map shown in Fig. 5.3b is based on eigenvalue analysis of an analytically determined matrix. The stability map in Fig. 5.3b corresponds for $\alpha = 1$ to the stability behavior of the periodic MATHIEU equation (5.8). For $\alpha \to 0$ the resolution of the determined stability map (for shape functions up to N_6, according to Tab. 5.1) can become more accurate by taking into account more shape functions. This comes with the drawback that the dimension of the matrices of the expanded system becomes very large, so that efficient algorithms for solving the corresponding eigenvalue problem are required.

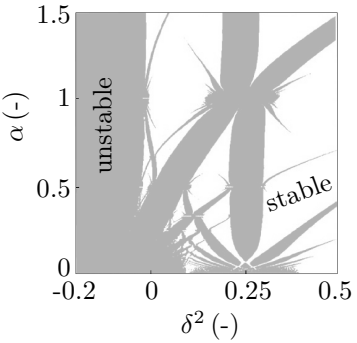

(a) Stability map of the quasi-periodic MATHIEU equation (5.8). Calculated by RAND et al. in [42].

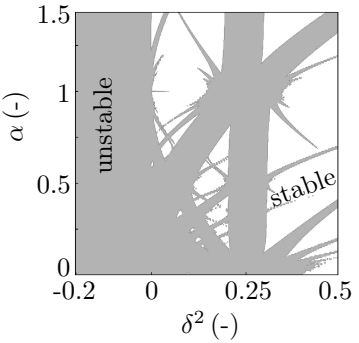

(b) Stability map of the quasi-periodic MATHIEU equation (5.7) with $\eta = 0.2$, $\epsilon = 10^{-3}$, N_6, $T = 10^4\pi$.

Figure 5.3: Stability maps of the periodic and quasi-periodic MATHIEU equation.

Multiple degrees of freedom

A system of linear non-autonomous but homogeneous ordinary differential equations can be written in the general form

$$\mathbf{C}(t)\,\ddot{\mathbf{y}} + \mathbf{B}(t)\,\dot{\mathbf{y}} + \mathbf{A}(t)\,\mathbf{y} = \mathbf{0}, \qquad \mathbf{y} = \mathbf{y}(t). \tag{5.15}$$

In order to motivate the use of discretization mothods for partial differential equations, the non-autonomous system (5.15) is embedded into the autonomous form

$$\mathbf{C}(x)(\ddot{\mathbf{y}}+2\dot{\mathbf{y}}'+\mathbf{y}'')+\mathbf{B}(x)(\dot{\mathbf{y}}+\mathbf{y}')+\mathbf{A}(x)\,\mathbf{y}=\mathbf{0}, \quad \mathbf{y} = \mathbf{y}(x,t), \tag{5.16}$$

which describes a partial differential equation in the independent variables x and t. The identity between the systems (5.15) and (5.16) can be checked by applying the constraint $x = t$. According to the GALERKIN discretization method the solution $\mathbf{y}$ is expanded as

$$\mathbf{y}(x,t)=\mathbf{W}(x)\mathbf{q}(t) \quad \text{with} \quad \mathbf{W}(x)=\mathbf{I}\otimes\mathbf{w}^{\mathrm{T}}(x), \tag{5.17}$$

where the *ansatz* functions are summarized in the vector $\mathbf{w}=[w_1, w_2, \cdots, w_N]^{\mathrm{T}}$ and the modal coordinates in the vector $\mathbf{q}$, respectively. The operator $\otimes$ denote the KRONECKER product[3]. Inserting this expansion into Eq. (5.16) yields

$$\mathbf{C}(x)(\mathbf{W}''\mathbf{q}+2\mathbf{W}'\dot{\mathbf{q}}+\mathbf{W}\ddot{\mathbf{q}})+\mathbf{B}(x)(\mathbf{W}'\mathbf{q}+\mathbf{W}\dot{\mathbf{q}})+\mathbf{A}(x)\mathbf{W}\mathbf{q}=\mathbf{0}. \tag{5.18}$$

The same result is obtained by inserting the expansion (5.17) directly into the non-autonomous system (5.15) and taking into account the constraint $x=t$. Multiplying Eq. (5.18) from the left-hand side with $\mathbf{W}^{\mathrm{T}}$ and integration over a characteristic interval $[0, T]$ leads to a system of ordinary differential equations in the modal coordinates $\mathbf{q}$,

$$\boldsymbol{\mathcal{M}}\,\ddot{\mathbf{q}}+\boldsymbol{\mathcal{B}}\,\dot{\mathbf{q}}+\boldsymbol{\mathcal{C}}\,\mathbf{q}=\mathbf{0}, \qquad \mathbf{q}^{\mathrm{T}}=[q_1(t), q_2(t), \cdots, q_M(t)]\,. \tag{5.19}$$

Considering the expansion (5.17), the matrices reduce to

$$\begin{aligned}
\boldsymbol{\mathcal{M}} &= \int_0^T \mathbf{C}(x)\otimes\mathbf{w}\mathbf{w}^{\mathrm{T}}\,\mathrm{dx},\\
\boldsymbol{\mathcal{B}} &= \int_0^T \left[2\mathbf{C}(x)\otimes\mathbf{w}\mathbf{w}'^{\mathrm{T}}+\mathbf{B}(x)\otimes\mathbf{w}\mathbf{w}^{\mathrm{T}}\right]\mathrm{dx},\\
\boldsymbol{\mathcal{C}} &= \int_0^T \left[\mathbf{C}(x)\otimes\mathbf{w}\mathbf{w}''^{\mathrm{T}}+\mathbf{B}(x)\otimes\mathbf{w}\mathbf{w}'^{\mathrm{T}}+\mathbf{A}(x)\otimes\mathbf{w}\mathbf{w}^{\mathrm{T}}\right]\mathrm{dx}.
\end{aligned} \tag{5.20}$$

The dimension of the new state vector is $\dim\mathbf{q}=\dim\mathbf{w}\dim\mathbf{y}$.

Initiation of self-excited vibrations through periodic excitation

In order to initiate self-excited vibrations the trivial solution has to be destabilized. This was investigated in previous section for constant excitation parameters, such as the pre-stress and rotation speed of the rotor. Depending on the application, also excitation mechanisms are possible, where the rotation speed changes periodically, see for example Fig. 1.3. For this reason, the stability behavior of the wobbling disk generator is analyzed considering a periodic rotation speed of the type

$$\Omega=\widehat{\Omega}\,\mathrm{sign}\,(\cos\widehat{\omega}\,t)\,. \tag{5.21}$$

[3]The KRONECKER product of two matrices is defined as $\mathbf{C}=\mathbf{A}\otimes\mathbf{B}$, with $\mathbf{c}_{ij}=a_{ij}\mathbf{B}$.

The reason for this rectangular form is that $\Omega = 0$ should be avoided, since this leads to an infinite damping coefficient, see Tab. 3.1. The *embedding technique* is applied on the equations of motion of the stator (3.51) using the shape functions (5.11). The resulting stability map in the $\widehat{\omega}$-$\widehat{\Omega}$-plane is shown in Fig. 5.4. The stability boundary for constant rotation speed is denoted

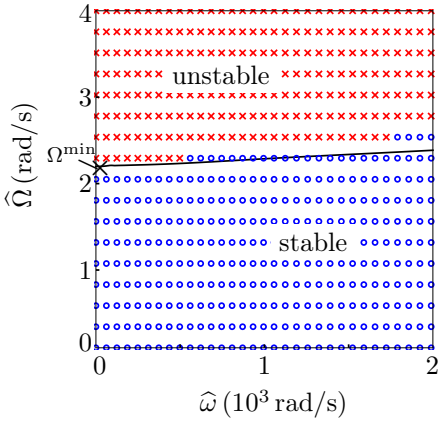

Figure 5.4: Stability map of the system (3.51) for periodic rotation speed Ω: Comparison of the results obtained by FLOQUET theory (crosses and circles) and the *embedding technique* (solid line).

by $\Omega^{\min}$, which corresponds to the stability boundary for $\widehat{\omega} \to 0$. Moreover, by increasing the frequency $\widehat{\omega}$ the stability boundary moves to slightly larger values of $\widehat{\Omega}$. Therefore, the approximation of the stability boundary for periodic excitation can be approximated by the stability boundary for constant rotation speed ($\widehat{\Omega}^{\text{crit}} \approx \Omega^{\min}$) and the dependence on $\widehat{\omega}$ can be neglected. Since the analyzed system (3.51) has the same structure as the linearized system for the traveling wave generator (4.41), the obtained results are also valid for periodic excitation of this type of generator. Furthermore, Fig. 5.4 shows that the results obtained by applying the *embedding technique* are in good agreement with FLOQUET theory (crosses and circles). However, the computation of the monodromy matrix, needed to determine stability behavior according to the FLOQUET theory, is very time-consuming, especially for $\widehat{\omega} \to 0$, where the system becomes very stiff[4]. In case of the *embedding technique*, due to the purely analytical procedure, the computational effort was significantly lower.

[4]This occurs due to the large difference between $\widehat{\omega}$ and the natural frequency of the system.

Simple example of a non-periodic system

In the following, the applicability of the *embedding technique* on non-periodic systems is analyzed. This is relevant for the stability analysis of the steady-state motion of the wobbling disk generator, studied in section 5.1.2. First, a simple example of a linear time-variant system is considered,

$$\dot{\mathbf{y}} = \mathbf{A}(t)\,\mathbf{y}\,, \quad \text{with} \quad \mathbf{A}(t) = \mathbf{A}_0 + t\mathbf{A}_1, \tag{5.22}$$

$$\mathbf{A}_0 = \begin{bmatrix} \lambda_1 & 0 \\ 0 & \lambda_2 \end{bmatrix}, \quad \mathbf{A}_1 = \begin{bmatrix} 0 & \varepsilon_1 \\ \varepsilon_2 & 0 \end{bmatrix}. \tag{5.23}$$

The parameters λ_i are chosen in such a way that the unperturbed system ($\varepsilon_i = 0$) is asymptotically stable ($\lambda_i < 0$). Allowing small perturbations with $\varepsilon_i \neq 0$, the stability analysis becomes a non trivial task, since there exists no closed-form stability theory for time-variant systems. Nevertheless, the results obtained by applying the *embedding technique* can be compared to numerical simulation of the given system.

According to the generalized form in Eq. (5.15) the system matrices are

$$\mathbf{C}(x) = \mathbf{0}\,, \qquad \mathbf{B}(x) = \mathbf{I}\,, \qquad \mathbf{A}(x) = -\mathbf{A}_0 - x\,\mathbf{A}_1, \tag{5.24}$$

where the time variable t is replaced by the new independent variable x. Applying the GALERKIN-type projection an autonomous system of ordinary differential equations in the modal coordinates $\mathbf{q}$ is obtained, see Eq. (5.19). The matrices of this system are given by

$$\boldsymbol{\mathcal{M}} = \mathbf{0}, \qquad \boldsymbol{\mathcal{B}} = \mathbf{I} \otimes \mathbf{W}_0, \qquad \boldsymbol{\mathcal{C}} = \mathbf{I} \otimes \mathbf{W}_1 - \mathbf{A}_0 \otimes \mathbf{W}_0 - \mathbf{A}_1 \otimes \mathbf{W}_x, \tag{5.25}$$

with

$$\mathbf{W}_0 = \int_0^T \mathbf{w}\mathbf{w}^{\mathrm{T}}\mathrm{d}x\,, \qquad \mathbf{W}_1 = \int_0^T \mathbf{w}\mathbf{w}'^{\mathrm{T}}\mathrm{d}x\,, \qquad \mathbf{W}_x = \int_0^T x\mathbf{w}\mathbf{w}^{\mathrm{T}}\mathrm{d}x. \tag{5.26}$$

Thereby, the time-variant system (5.22) is transformed into a time-invariant system of a much higher order in the modal coordinates $\mathbf{q}$,

$$\boldsymbol{\mathcal{B}}\,\dot{\mathbf{q}} + \boldsymbol{\mathcal{C}}\,\mathbf{q} = \mathbf{0}\,, \quad \text{with} \quad \mathbf{y} = \left(\mathbf{I} \otimes \mathbf{w}^{\mathrm{T}}\right)\,\mathbf{q}\,. \tag{5.27}$$

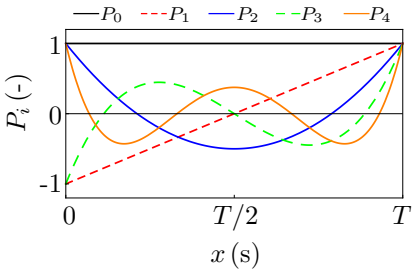

Figure 5.5: LEGENDRE polynomials $P_i(x)$, orthogonal on the interval $[0, T]$.

The LEGENDRE polynomials $P_i(x)$, shown in Fig. 5.5, are chosen as *ansatz* functions $w_i(x)$. Basically, the LEGENDRE polynomials $P_i(\xi)$ are orthogonal on the interval $[-1, 1]$. In order to adjust the polynomials to the interval $[0, T]$ the transformation $\xi = (2/T)\, x - 1$ was used. Using $N = 10$ *ansatz* functions and taking into account only the converged eigenvalues, the stability map shown in Fig. 5.6 is obtained. If the parameters ε_1 and ε_2 have different signs, the system is always asymptotically stable. Otherwise, divergence instability can occur. In order to validate this results, a numerical simulation of the time-variant system (5.22) was performed. To this end, two different

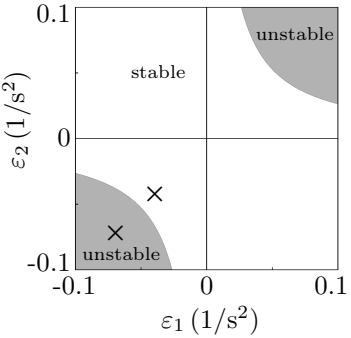

(a) Stability boundary and parameter sets for simulation (cross).

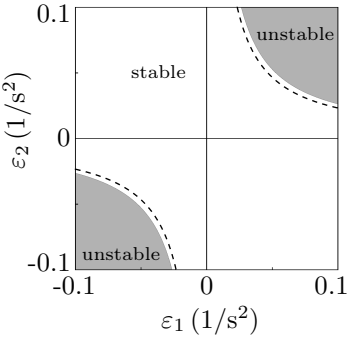

(b) Stability boundary compared to the estimate (5.28) (dashed).

Figure 5.6: Stability map of the system (5.22) with $\lambda_1 = -2\,\mathrm{s}^{-1}$, $\lambda_2 = -1\,\mathrm{s}^{-1}$ and $T = 50\,\mathrm{s}$; (Results are based on the *embedding technique*).

parameter sets are chosen for ε_i, namely one in the stable and one in the unstable region, see Fig. 5.6a. The numerical results are shown in Fig. 5.7 and are in good agreement with the results obtained by applying the *embedding technique*. For the parameters corresponding to the stable region in Fig. 5.6a

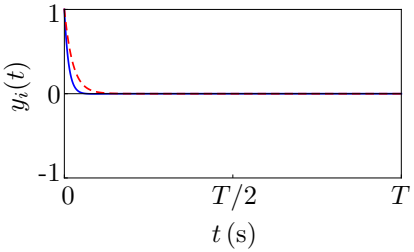

(a) Asymptotically stable solution for $\varepsilon_1 = \varepsilon_2 = -0.04\,\mathrm{s}^{-2}$.

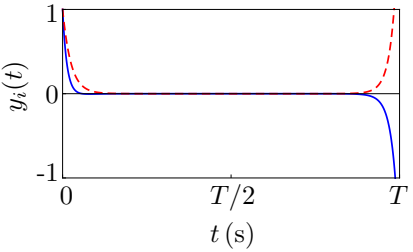

(b) Divergent solution for $\varepsilon_1 = \varepsilon_2 = -0.07\,\mathrm{s}^{-2}$.

Figure 5.7: Numerical solution of the system (5.22) using the parameters shown Fig. 5.6a; solid line: $y_2(t)$, dashed line: $y_1(t)$.

the numerical simulation shows asymptotically stable behavior up to $t^* = T$, (Fig. 5.7a). In the case of parameters from the unstable region, the numerical simulation shows a divergent behavior, see Fig. 5.7b. By applying, for example, the ROUTH-HURWITZ stability criterion to the autonomous system (5.27), approximations of the stability boundary can be calculated. For $N = 2$ and $\lambda_i < 0$ the system (5.27) is stable for

$$\varepsilon_1 \varepsilon_2 < \frac{3\lambda_1 \lambda_2}{T\left(T + \frac{3}{\lambda_1 + \lambda_2}\right)}. \tag{5.28}$$

This estimate for the stability boundary is denoted by a dashed line in Fig. 5.6b and is in good agreement with the calculated results for $N = 10$. According to the estimate (5.28), the stability boundary vanishes in the first and the third quadrant for an increase of the characteristic time T (Fig. 5.6). This is in agreement with the numerical investigations made, namely divergence of the solution for $\varepsilon_1 \varepsilon_2 < 0$. Of course, the *embedding technique* can be applied for $T \to \infty$ in order to determine stability behavior for an infinite time. However,

this would require also an infinite number of *ansatz* functions ($N \to \infty$) to achieve convergency of the eigenvalues of the system (5.27). Nevertheless, the *embedding technique* has the advantage that, due to its analytical form, estimates for the stability boundary can be calculated as functions of the system parameters.

5.1.2 Stability of the wobbling motion

In this section the *embedding technique* is used to determine the stability of the steady-state solution of the wobbling disk generator. To this end, the nonlinear equations of motion (3.125) are linearized around the steady-state solution described by the wobbling motion (3.92). Thereby, a linear time-variant system is obtained, which reads

$$\mathbf{M}\,\Delta\ddot{\mathbf{q}}_S + \mathbf{B}\,\Delta\dot{\mathbf{q}}_S + (\mathbf{C}_0 + t\mathbf{C}_1)\Delta\mathbf{q}_S = \mathbf{0}\,, \quad \Delta\mathbf{q}_S = \mathbf{q}_S - \mathbf{q}_E, \tag{5.29}$$

with

$$\mathbf{M} = \begin{bmatrix} \Theta_S s_{\hat{q}}^2 + \Theta_3 c_{\hat{q}}^2 & 0 & \Theta_3 c_{\hat{q}} \\ 0 & \Theta_S & 0 \\ \Theta_3 c_{\hat{q}} & 0 & \Theta_3 \end{bmatrix}, \quad \mathbf{C}_1 = k_t t_{\hat{q}} \Omega \begin{bmatrix} 0 & 1 & 0 \\ 0 & 0 & 0 \\ 0 & c_{\hat{q}} & 0 \end{bmatrix}, \tag{5.30}$$

$$\mathbf{B} = \begin{bmatrix} d_t & \Omega[\Theta_3 t_{\hat{q}} + 2c_{\hat{q}} s_{\hat{q}}(\Theta_S - \Theta_3)] & d_t c_{\hat{q}} \\ -\Omega[\Theta_3 t_{\hat{q}} + 2c_{\hat{q}} s_{\hat{q}}(\Theta_S - \Theta_3)] & d_S + d_R r_C^{*2} & \Omega\Theta_3 s_{\hat{q}} \\ d_t c_{\hat{q}} & -\Omega\Theta_3 s_{\hat{q}} & d_S s_{\hat{q}}^2 + d_t c_{\hat{q}}^2 \end{bmatrix},$$

$$\mathbf{C}_0 = \begin{bmatrix} k_t & d_t\Omega t_{\hat{q}} - k_t\beta s_{\hat{q}} & k_t c_{\hat{q}} \\ 0 & k_S + k_R r_C^{*2} - \Omega^2[\Theta_3 + (\Theta_S - \Theta_3)c_{2\hat{q}}] - h_C^* F_N^* & 0 \\ k_t c_{\hat{q}} & \Omega s_{\hat{q}}(d_t - 2d_S) - 2k_t c_{\hat{q}}\beta - \dfrac{r h_C^*}{r_C^{*2}} M_R & k_t c_{\hat{q}}^2 \end{bmatrix}.$$

The abbreviation used are $s_{\hat{q}} = \sin\hat{q}$, $c_{\hat{q}} = \cos\hat{q}$, $t_{\hat{q}} = \tan\hat{q}$ and $c_{2\hat{q}} = \cos 2\hat{q}$. The new state vector $\Delta\mathbf{q}_S$ describes the difference between the generalized coordinates of the stator $\mathbf{q}_S$ and the corresponding steady-state solution $\mathbf{q}_E$. Applying GALERKIN-type projection leads to an autonomous system in the

modal coordinates $\mathbf{q}$ of the form (5.19), where the matrices are

$$\boldsymbol{\mathcal{M}} = \mathbf{M} \otimes \mathbf{W}_0, \qquad \boldsymbol{\mathcal{B}} = 2\mathbf{M} \otimes \mathbf{W}_1 + \mathbf{B} \otimes \mathbf{W}_0, \tag{5.31}$$

$$\boldsymbol{\mathcal{C}} = \mathbf{M} \otimes \mathbf{W}_2 + \mathbf{B} \otimes \mathbf{W}_1 - \mathbf{C}_0 \otimes \mathbf{W}_0 - \mathbf{C}_1 \otimes \mathbf{W}_x, \tag{5.32}$$

with

$$\mathbf{W}_0 = \int_0^T \mathbf{w}\mathbf{w}^{\mathrm{T}} \mathrm{d}x, \quad \mathbf{W}_1 = \int_0^T \mathbf{w}\mathbf{w}'^{\mathrm{T}} \mathrm{d}x, \quad \mathbf{W}_2 = \int_0^T \mathbf{w}\mathbf{w}''^{\mathrm{T}} \mathrm{d}x, \quad \mathbf{W}_x = \int_0^T x\mathbf{w}\mathbf{w}^{\mathrm{T}} \mathrm{d}x. \tag{5.33}$$

Thereby, the time-variant system (5.29) is transformed into a time-invariant system of ordinary differential equations in the modal coordinates $\mathbf{q}$ with the dimension $M = 3N$,

$$\boldsymbol{\mathcal{M}}\,\ddot{\mathbf{q}} + \boldsymbol{\mathcal{B}}\,\dot{\mathbf{q}} + \boldsymbol{\mathcal{C}}\,\mathbf{q} = \mathbf{0}\,, \quad \text{with} \quad \Delta\mathbf{q}_S = \left(\mathbf{I} \otimes \mathbf{w}^{\mathrm{T}}\right)\mathbf{q}\,. \tag{5.34}$$

The LEGENDRE polynomials, which are illustrated in Fig. 5.5, are used as *ansatz* functions. By taking into account only the converged eigenvalues, the results displayed in Fig. 5.8 are obtained. In the analysis, the number of *ansatz* functions was $N = 11$ and the characteristic time $T = 10^{-2}$ s. According to the

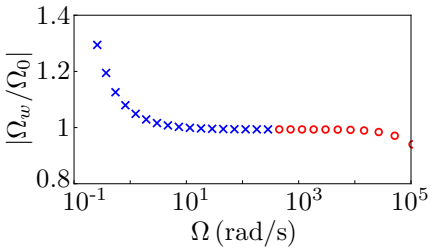

(a) Steady state in the Ω-Ω_w-plane.

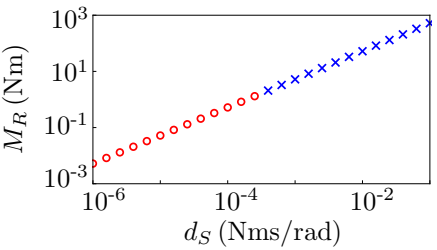

(b) Steady state in the d_S-M_R-plane.

Figure 5.8: Stability of the steady-state solution of the wobbling disk generator; stable (cross), unstable (circle).

embedding technique, the steady-state solution of the wobbling disk generator is asymptotically stable up to a rotation speed of $\Omega \approx 350\,\mathrm{rad/s}$. Above this value the solution becomes unstable. In order to validate these results, a numerical simulation of the equations of motion (3.125) is performed. The

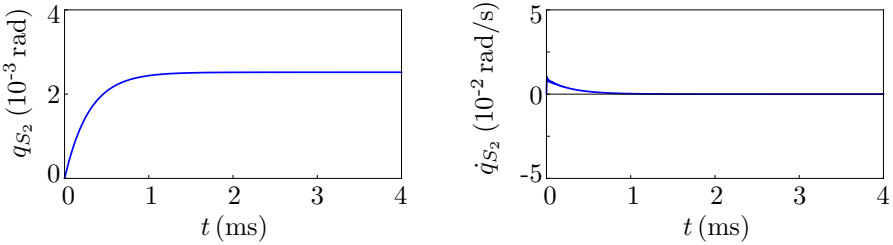

(a) Wobbling amplitude q_{S_2} over t. **(b)** Angular velocity $\dot{q}_{S_2}$ over t.

Figure 5.9: Numerical solution of the steady-state motion of the wobbling disk generator (asymptotically stable solution), $M_R = 0.33\,\text{Nm} \Rightarrow \Omega = 3{\cdot}10^2\,\text{rad/s}$.

numerical solution for the generalized coordinate q_{S_2}, which is equivalent to the wobbling amplitude, is plotted in Fig. 5.9. It can be observed that $q_{S_2}(t)$ increases up to the value for the steady state and remains constant (Fig. 5.9a). Moreover, the corresponding angular velocity $\dot{q}_{S_2}(t)$ approaches zero, which can be seen in Fig. 5.9b. These results confirm the stability statement obtained by applying the *embedding technique* in Fig. 5.8a. Further numerical simulation of a steady state predicted as unstable is displayed in Fig. 5.10. Clearly, the steady-state solution becomes unstable, which fully agrees with the stability behavior determined. In the same way, the stability character-

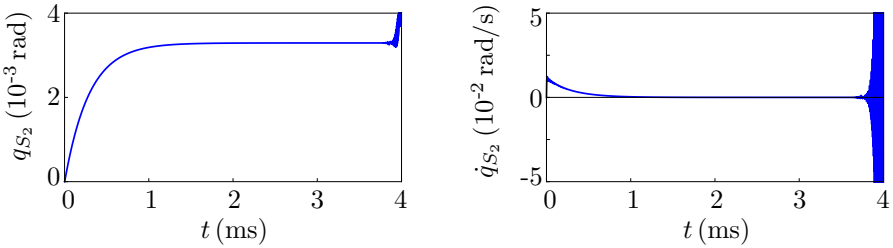

(a) Wobbling amplitude q_{S_2} over t. **(b)** Angular velocity $\dot{q}_{S_2}$ over t.

Figure 5.10: Numerical solution of the steady-state motion of the wobbling disk generator (unstable solution), $M_R = 0.43\,\text{Nm} \Rightarrow \Omega = 4{\cdot}10^2\,\text{rad/s}$.

istics shown in Fig. 5.8b are verified by numerical simulation. This results show that the steady-state solution becomes unstable for vanishing damping of the shaft. Since the shaft has some inherent damping properties, a minimum system damping is always assured. As mentioned before, increasing the characteristic time T leads to the necessity of much more *ansatz* functions N to ensure convergence. However, in real-life applications stability statements are not required up to an infinite time but only up to specific finite time, which justifies the previously performed analysis.

5.2 Basins of attraction

In the following, the construction of LYAPUNOV functions using CARLEMAN linearization is considered. These LYAPUNOV functions can then be used to estimate the basin of attraction of the considered stable solution.

5.2.1 Theoretical background

In the following a brief review of the used methods for the estimation of basins of attraction is given.

LYAPUNOV's direct method

A common approach for the estimation of basins of attraction is LYAPUNOV's direct method, which is described by the following theorem. A good introduction in this topic is given by HAGEDORN in [13], by VERHULST in [58] and ADAMY in [2].

Theorem:
Let $V(\mathbf{x})$ be a LYAPUNOV *function for the time continuous system*

$$\dot{\mathbf{x}} = \mathbf{f}(\mathbf{x}), \quad \mathbf{f}(\mathbf{0}) = \mathbf{0}. \tag{5.35}$$

The domain

$$G = \{\mathbf{x} \in \mathbb{R}^n, 0 < V(\mathbf{x}) < c, \dot{V}(\mathbf{x}) < 0\}, \tag{5.36}$$

where c is a positive real constant, belongs to the basin of attraction of $\mathbf{x} = \mathbf{0}$.

According to this theorem, a LYAPUNOV function $V(\mathbf{x})$ has to be found for the system (5.35) in order to determine the basin of attraction of the trivial solution. However, no general systematic approach exists so far, which describes how to construct an appropriate LYAPUNOV function. In the literature many different construction methods are proposed for different type of systems. For example the ZUBOV method in [65] or a method proposed by VANNELLI and VIDYASAGAR to construct the so-called 'maximum LYAPUNOV function' in [57], or by combining LYAPUNOV's direct method with the center manifold theory proposed by HOCHLENERT in [19] and by SPELSBERG-KORSPETER et al. in [54]. One of the simplest approaches to construct a LYAPUNOV function is to choose a quadratic function in the state variables

$$V(\mathbf{x}) = \mathbf{x}^{\mathrm{T}} \mathbf{R}\, \mathbf{x}, \tag{5.37}$$

where $\mathbf{R}$ satisfies the LYAPUNOV equation

$$\mathbf{A}_1^{\mathrm{T}} \mathbf{R} + \mathbf{R}\, \mathbf{A}_1 = -\mathbf{Q}. \tag{5.38}$$

The matrix $\mathbf{A}_1$ corresponds to the JACOBIAN matrix of the system (5.35) and is also referred to as the system matrix of the linearized form of Eq. (5.35). The matrix $\mathbf{Q}$ can be an arbitrary positive definite matrix. However, this approach often leads to poor estimates of the basins of attraction.

CARLEMAN linearization

In 1932, TORSTEN CARLEMAN, a Swedish mathematician, followed the idea of POINCARÉ and devised the CARLEMAN *embedding technique*, [7], also called CARLEMAN *linearization*. The idea was to embed a nonlinear system of a finite dimension into a linear system with an infinite dimension by considering the nonlinear terms as additional states of the system. Different applications of the CARLEMAN *linearization* are discussed by KOWALSKI and STEEB in [28]. This procedure is explained for the autonomous nonlinear system

$$\dot{\mathbf{x}} = \mathbf{f}(\mathbf{x}), \qquad \mathbf{f}(\mathbf{0}) = \mathbf{0}, \quad \text{with} \quad \mathbf{x} = [x_1, x_2, \cdots, x_n]^{\mathrm{T}}. \tag{5.39}$$

A TAYLOR series expansion of the right-hand side[5] yields

$$\dot{\mathbf{x}} = \mathbf{A}_1\mathbf{x} + \mathbf{A}_2\mathbf{x}^{[2]} + \mathbf{A}_3\mathbf{x}^{[3]} + \cdots + \mathbf{A}_m\mathbf{x}^{[m]} + \mathcal{O}(\mathbf{x}^{[m+1]}), \tag{5.40}$$

where the dimension of the state vector $\mathbf{x}^{[k]}$, which contains monomials of order k, is given by the binomial coefficient[6] $\binom{n+k-1}{k}$. It should be noted that by defining $\mathbf{x}^{[k]} := \mathbf{x} \otimes \mathbf{x} \otimes \cdots \otimes \mathbf{x}$ (k-times), according to [28], some monomials appear twice in the new state vector $\mathbf{x}^{[k]}$. In the further analysis, $\mathbf{x}^{[k]}$ is assumed to contain only single monomials. Treating nonlinearities as additional state variables by defining $\mathbf{y}_i := \mathbf{x}^{[i]}$ yields

$$\dot{\mathbf{y}} = \mathbf{A}\mathbf{y} + \mathbf{g}(\mathbf{y}), \qquad \mathbf{y} = [\mathbf{x}^{\mathrm{T}}, {\mathbf{x}^{[2]}}^{\mathrm{T}}, {\mathbf{x}^{[3]}}^{\mathrm{T}}, \cdots, {\mathbf{x}^{[m]}}^{\mathrm{T}}]^{\mathrm{T}}, \tag{5.41}$$

where the dimension of the new state vector $\mathbf{y}$ is

$$\dim \mathbf{y} = \sum_{k=1}^{m} \binom{n+k-1}{k} = \binom{n+m}{1+m} \frac{m+1}{n} - 1. \tag{5.42}$$

For the expansion order $m \to \infty$, the nonlinear equation (5.39) with the dimension n is embedded into the infinite-dimensional linear system (5.41), ($\mathbf{g}(\mathbf{y}) \to 0$). Then, the solution for $\mathbf{x}(t)$ can be expressed as a sum of the modal solutions of this infinite-dimensional system. Clearly, this procedure fails if the infinite sum does not converge. Therefore, it is essential to check the convergence behavior, which is barely done in the literature. However, the analyzed systems always showed convergence in the neighbourhood of a stable trivial solution. This can be checked analytically by using the minimal example from KOWALSKI and STEEB in [28], see [18].

5.2.2 Construction of LYAPUNOV functions using CARLEMAN linearization

The advantage of the simple approach for a LYAPUNOV function (5.37) is that $V(\mathbf{x})$ is constructed based on the linearized system, but since only linear terms are taken into account, the resulting estimate for the basin of attraction is

[5] The right-hand side is required to be differentiable.
[6] The binomial coefficient is defined as: $\binom{n}{k} = \prod_{i=1}^{k} \frac{n-k+i}{i}$.

very poor. In order to overcome this disadvantage, but maintain the simplicity of the construction method, the CARLEMAN linearization is used. Through this procedure nonlinear terms can be considered in the simple construction approach. The system matrix $\mathbf{A}$ of the expanded system (5.41) is be used to construct $V(\mathbf{x})$ instead of the linearized form of Eq. (5.39),

$$V(\mathbf{x}) = \mathbf{y}^{\mathrm{T}}(\mathbf{x})\mathbf{R}\,\mathbf{y}(\mathbf{x}), \qquad \mathbf{A}^{\mathrm{T}}\mathbf{R} + \mathbf{R}\,\mathbf{A} = -\mathbf{Q}. \tag{5.43}$$

According to the Eq. (5.36), the states inside the basin of attraction have to fulfill $\dot{V}(\mathbf{x}) < 0$, which can be calculated by $\dot{V}(\mathbf{x}) = \mathbf{f}^{\mathrm{T}}(\mathbf{x}) \cdot \boldsymbol{\nabla} V(\mathbf{x})$. The transformation back to the original state variables $\mathbf{x}$ is done by using the relation in Eq. (5.41). It is essential for the solution of the LYAPUNOV equation (5.43) that the matrix $\mathbf{Q}$ has to be positive definite only in the $\mathbf{y}_1$-space, which corresponds to the original state variables $\mathbf{x}$. A similar approach for construction of LYAPUNOV function using CARLEMAN linearization technique, was proposed by BANKS in [3] and by HAMIDI et al. in [16]. However, the author does not discuss the necessary properties of the matrix $\mathbf{Q}$, which should be only positive definite in the original state variables. For example, the trivial choice of $\mathbf{Q}=\mathbf{I}$ leads to poor results for the estimate of the basin of attraction. Furthermore, the authors propose an extended state vector consisting of several monomials twice, which leads to a decrease of the efficiency.

VAN DER POL oscillator

As a simple example the inverted[7] VAN DER POL oscillator is considered. The equation of motion reads

$$\ddot{x} + \epsilon\,\dot{x}(1 - \alpha\,x^2) + \omega^2 x = 0. \tag{5.44}$$

[7] The VAN DER POL oscillator has an unstable trivial solution and a stable limit cycle. By inverting the time scale $\mathrm{d}\tau = -\mathrm{dt}$ the trivial solution becomes stable and the limit cycle unstable.

Applying the CARLEMAN linearization up to the order $m = 3$ yields

$$\dot{\mathbf{y}} = \mathbf{A}\,\mathbf{y} + \mathbf{g}(\mathbf{y}), \quad \text{with} \tag{5.45}$$

$$\mathbf{A} = \begin{bmatrix} 0 & 1 & 0 & 0 & 0 & 0 \\ -\omega^2 & -\epsilon & 0 & \alpha\epsilon & 0 & 0 \\ 0 & 0 & 0 & 3 & 0 & 0 \\ 0 & 0 & -\omega^2 & -\epsilon & 2 & 0 \\ 0 & 0 & 0 & -2\omega^2 & -2\epsilon & 1 \\ 0 & 0 & 0 & 0 & -3\omega^2 & -3\epsilon \end{bmatrix} \quad \text{and} \quad \mathbf{y} = \begin{bmatrix} x \\ \dot{x} \\ x^3 \\ x^2\dot{x} \\ x\dot{x}^2 \\ \dot{x}^3 \end{bmatrix}.$$

The matrix $\mathbf{Q}$ has the form[8]

$$\mathbf{Q} = \begin{bmatrix} \mathbf{Q}^* & \mathbf{0} \\ \mathbf{0} & \mathbf{0} \end{bmatrix}, \qquad \text{with} \quad \mathbf{Q}^* > 0. \tag{5.46}$$

In this case, $\mathbf{Q}^*$ is an arbitrary positive definite 2×2 matrix. Moreover, the monomials in the new state vector $\mathbf{y}$ are of an odd order. This characteristic depends on the structure of the considered system (Eq. (5.44)). Using $\mathbf{A}$ and $\mathbf{Q}$ to solve the LYAPUNOV equation (5.43) for $\mathbf{R}$ leads to $V(\mathbf{x})$. The evaluation of $\dot{V}(\mathbf{x})$ leads to the estimate for basin of attraction, shown in Fig. 5.11. The critical line, which denote $\dot{V}(\mathbf{x}) = 0$, is plotted in Fig. 5.11a with the corresponding basin of attraction $\widetilde{G}$. This estimate is compared in Fig. 5.11b to the exact basin of attraction G, whose limits are identical to the limit cycle of the VAN DER POL oscillator without time inversion. In addition, the estimate $\widetilde{G}_0$, constructed using the linearised form of Eq. (5.44), is shown. Compared to the exact basin of attraction G this estimate is very poor. The estimate obtained using the CARLEMAN linearization ($\widetilde{G}$) approximates much better the exact basin of attraction. This example shows that by combining LYAPUNOV's direct method with the CARLEMAN linearization provides a simple method for the estimation of basins of attraction. Moreover, the expansion order m does not have to be very high in order to achieve good estimates. Due to the restriction in Eq. (5.36) the estimates are always conservative, which means that no overestimation of the basin of attraction can occur. The proposed

[8] A remark on the choice of $\mathbf{Q}^*$: Since the whole space of positive definite matrices is allowed, consequently all corresponding estimates of the basin of attraction can be put together to a superordinate estimate.

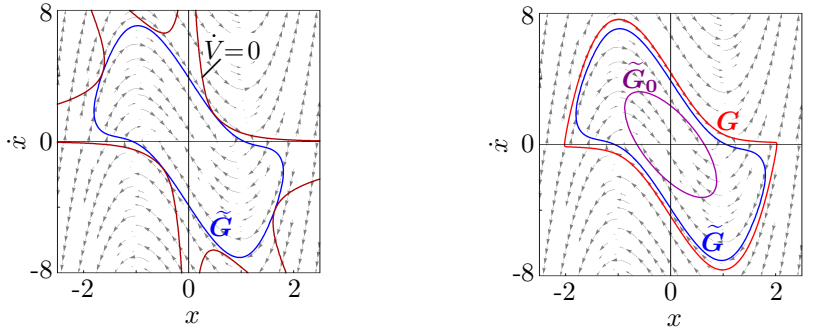

(a) Estimated basin of attraction $\widetilde{G}$.

(b) Comparison of the estimates.

Figure 5.11: Exact (G) and estimates ($\widetilde{G}$ for $m=3$ and $\widetilde{G}_0$ for $m=1$) of the basin of attraction of the inverted VAN DER POL oscillator (5.44) with $\alpha=1, \omega=1, \epsilon=5$.

method has two significant differences compared to the construction methods, which also use CARLEMAN linearization, in [3, 16]. One the one hand, the expanded vector contains only single monomials leading to an increase of efficiency. On the other hand, the matrix $\mathbf{Q}$ required for the solution of the LYAPUNOV equation, is only positive definite in the original state variables. This significantly improves the quality of the obtained estimate for the basin of attraction.

Steady-state characteristics of the traveling wave generator

The applicability of the previously described procedure for the estimation of basins of attraction by combining LYAPUNOV's direct method with the CARLEMAN linearization, on the traveling wave generator, is discussed in the following. Depending on the type of stable solution, of which the basin of attraction is to be determined, the procedure is more or less appropriate. For the traveling wave generator two types of stable solution exist. The first one is the equilibrium state, where no self-excited vibrations can occur. Depending on the excitation parameters, different modes can become self-excited, while other modes remain in their stable equilibrium position. In this case, the LYAPUNOV direct method cannot be used since the linearized system has

eigenvalues with negative real parts. The second type of stable solutions of the traveling wave generator are stable limit-cycle oscillations, resulting from a destabilization of the equilibrium position. The estimation of the basin of attraction of a limit cycle requires on the one hand, the knowledge of the time function describing the steady-state motion and on the other hand, a transformation of the equations of motion onto the known solution. In general, the resulting system is time-variant due to the time-dependence of the limit-cycle solution. The estimation of basins of attraction of time-variant system is much more difficult than for autonomous systems. In future work, the proposed method has to be extended for the estimation of basins of attraction of limit-cycle oscillations by treating not only nonlinear terms but also coefficients depending on time as additional state variables [17], which up to now has not been considered in the literature. This can be very useful for many practical applications, e.g. for the analysis of the steady-state operation of the traveling wave generator in the region, where many different modes can become self-excited. Through the estimation of the basins of attraction of each operation mode it can be predicted, under which circumstances which mode is active, in order to achieve the most efficient performance.

6 Experimental investigations

In the experiments, both the wobbling disk generator as well as the traveling wave generator were investigated with respect to their energy harvesting capabilities. This was done by inverting the actuation of common ultrasonic motors, namely the CANON bar-type ultrasonic motor U400 and the SHINSEI plate-type ultrasonic motor USR-60, shown in Fig. 1.2b and 1.2a. The motor characteristics of the CANON U400 was analyzed by GUTSCHMIDT in [11] and for the SHINSEI USR-60 by SATTEL in [45]. Besides the investigation of the steady-state characteristics also experimental modal analysis was carried out.

6.1 Experimental setup

The principal experimental setup consists of an excitation unit, the generator and the electric load, see Fig. 6.1. The excitation unit is an electric motor driving the rotor and providing an excitation torque M_R. Thereby, the rotor is set in rotation (rotation speed Ω). Once the stator part of the generator is self-excited, the piezoceramic is deformed leading to an alternating electric potential $v(t)$ at the electrodes. After rectification of $v(t)$ through the AC/DC-converter the effective voltage v_{eff} is applied on the electrical load. A common electrical resistance was used as electrical load in the electric circuit of each electrode.

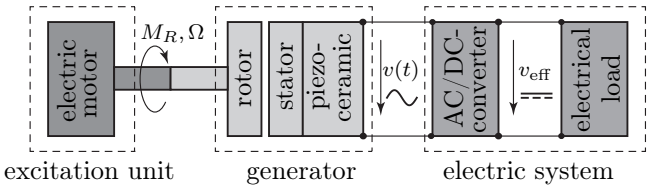

Figure 6.1: Principle schematics of the experimental setup.

6.2 Wobbling disk generator

In the following the experimental results obtained for the wobbling disk generator (inverted CANON bar-type ultrasonic motor U400) is discussed.

6.2.1 Steady-state characteristics

In agreement with the analytical results for the simplified model studied in chapter 3, for an initially given pre-stress a minimum rotation speed of the rotor is needed to initiate self-excitation. For the wobbling disk generator, the experimentally determined minimum rotation speed is $\Omega^{\min} = 2\pi\, 0.7\,\text{Hz}$. Above this critical rotation speed, self-excited oscillations occur leading to an alternating electric potential at the electrode. For $\Omega = 2\pi\, 2.3\,\text{Hz}$ the time signal of the electric voltage $v_i(t)$ is shown for both electrodes in Fig. 6.2a. In agreement with the analytical results (Fig. 3.19) the time signal of the

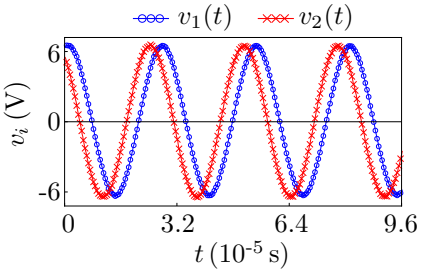

(a) Electric voltage output.

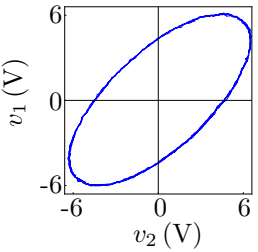

(b) Phase portrait of v_1 and v_2.

Figure 6.2: Electric voltage output of the wobbling disk generator for constant rotation speed ($\Omega = 2\pi\, 2.3\,\text{Hz}$).

steady-state motion has approximately the form of harmonic oscillations with a constant amplitude. Due to geometrical asymmetry, a phase shift between the time signals v_1 and v_2 can be observed, see Fig. 6.2b. The measurements of the amplitude and the frequency of $v_i(t)$ are plotted over the rotation speed Ω in Fig. 6.3. The observed characteristics are equivalent to the analytical results in Fig. 3.26: The wobbling frequency remains constant ($f_w \approx 36.5\,\text{kHz}$)

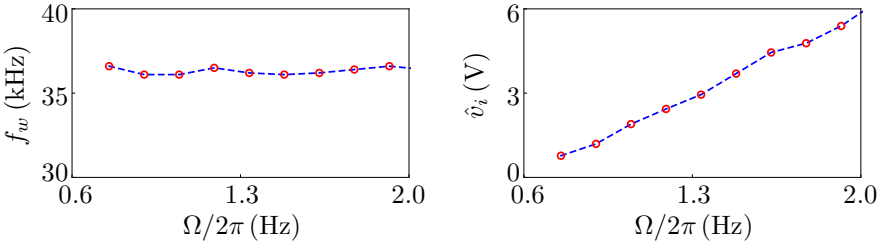

(a) Wobbling frequency over Ω. **(b)** Voltage amplitude $\hat{v}_i$ over Ω.

Figure 6.3: Steady-state transmission characteristics of the wobbling disk generator: Variation of the rotation speed Ω.

and the voltage amplitude increases linearly with the rotation speed. An essential design step of the generator is the adjustment of the optimum resistance, in order to achieve an efficient performance. An estimate for the optimum resistance is derived for the simplified model and is, according to the Eq. (3.67), approximately $R^* \approx 30\,\mathrm{k\Omega}$. Figure 6.4 shows the transfer char-

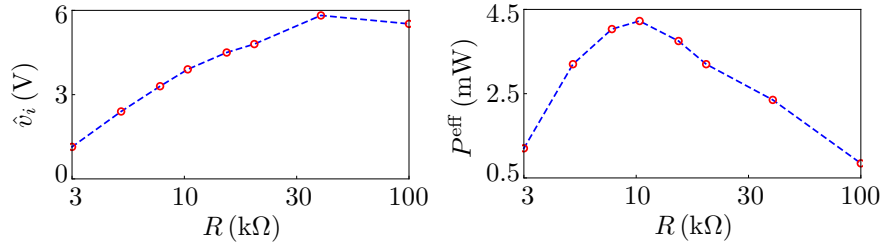

(a) Voltage amplitude $\hat{v}_i$ over R. **(b)** Effective power output P^{eff}.

Figure 6.4: Electric voltage and power output of the wobbling disk generator: Variation of the electric resistance R.

acteristics carried out in the experiments by varying the electric resistance R. The resulting optimum resistance can be read from Fig. 6.4b as $R^* = 10\,\mathrm{k\Omega}$. Obviously, the simplified model overestimates the exact optimum value for the resistance R, but still lies in the relevant kΩ-range. Figure 6.4a shows an approximately linear increase of the voltage amplitude. Moreover, in the an-

alyzed range of the electric resistance, the oscillation frequency f_w remained constant.

6.2.2 Modal analysis

In this section the results of the modal analysis, carried out for the stator part of the wobbling disk generator, are shown. The analysis of the simplified model in chapter 3 shows that the steady-state operation of the generator is predominated by the wobbling motion of the stator, which frequency is approximately the natural frequency of the system. The following results were carried out without the rotor pressed against the stator. As expected,

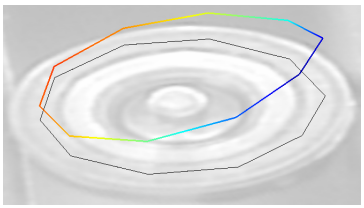

(a) $(1,0)_s$-mode (21.0 kHz).

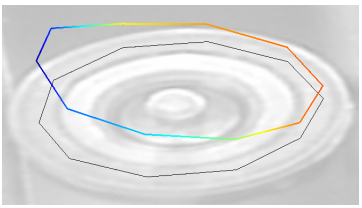

(b) $(1,0)_c$-mode (22.8 kHz).

Figure 6.5: Experimental modal analysis of the stator: $(1,0)$-mode.

the mode pair with the lowest natural frequency corresponds to the wobbling-type motion, shown in Fig. 6.5. The difference between the natural frequencies originates from the asymmetric design of the stator. The natural frequencies

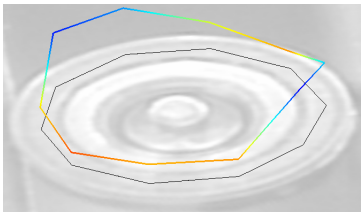

(a) $(2,0)_s$-mode (59.0 kHz).

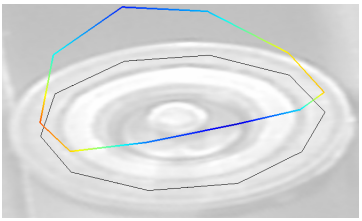

(b) $(2,0)_c$-mode (61.3 kHz).

Figure 6.6: Experimental modal analysis of the stator: $(2,0)$-mode.

of the $(1,0)$-mode are lower compared to the wobbling frequency in the operation mode ($f_w \approx 36.6\,\mathrm{kHz}$). Through the rotor, which is pressed against the stator, the system becomes stiffer and this leads therefore to higher natural frequencies. The next mode pair of the stator is illustrated in Fig. 6.6 and corresponds to the $(2,0)$-mode. Since this mode pair lies in a higher frequency range, the influence on the dynamics of the wobbling motion is negligible. The experimentally obtained results are in good agreement with the numerical modal analysis by using ABAQUS.

6.3 Traveling wave generator

This section deals with the experimental results carried out for the traveling wave generator, which are based on the inversion of the actuation of the SHINSEI plate-type ultrasonic motor. First, the electromechanical transmission characteristics in the steady state is discussed. Then the equivalence between the operation mode frequencies and the natural frequencies of the stator is shown based on the results from the modal analysis. Afterwards, different electrode configurations are discussed with respect to broad-band applicability of the generator.

6.3.1 Steady-state characteristics

The steady-state behavior of the traveling wave generator is similar to the behavior of the wobbling disk generator: For an initially applied pre-stress, a minimum rotation is required to initiate self-excited oscillations. The difference here is that many different modes of the elastic stator can become self-excited. The main goal of the experiments is to investigate in which circumstances which mode is active. First of all, the experiments showed that in the steady-state only one mode is vibrating. Exemplarily, the time signal of the mode with the frequency of 40.2 kHz is shown in Fig. 6.7a. The electric voltage outputs $v_i(t)$ have the form of harmonic signals with a constant amplitude. The phase difference between the signals is nearly $\pi/2$, see Fig. 6.7b. The complete transmission characteristics of the traveling wave ge-

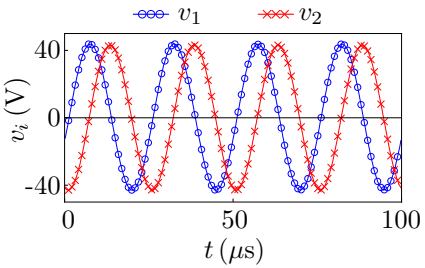

(a) Electric voltage output.

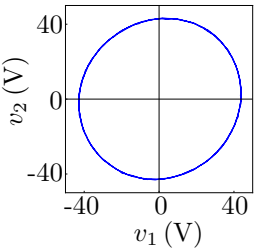

(b) Phase portrait of v_1 and v_2.

Figure 6.7: Electric voltage output of the traveling wave generator for constant pre-stress and rotation speed; $(10, 0)$-mode (40.2 kHz), $R_i = 7\,\mathrm{k\Omega}$.

nerator for the lower range of the rotation speed Ω is summarized in Fig. 6.8. Figure 6.8a shows that depending on the rotation speed different modes are active. Moreover, the frequency of an active mode remains constant unaffected by a change of the rotation speed, similarly to the transmission characteristic

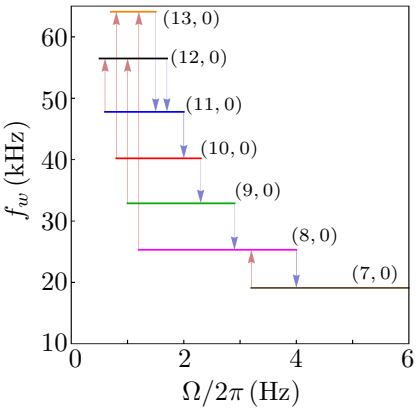

(a) Operation mode frequency f_w.

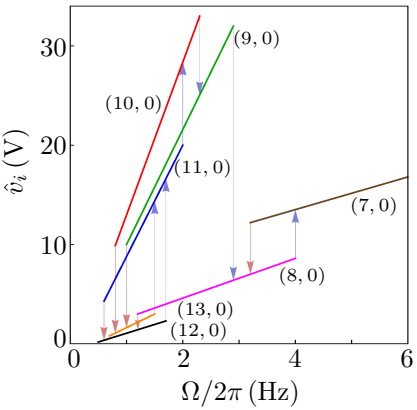

(b) Electric voltage amplitude $\hat{v}_i$.

Figure 6.8: Steady-state characteristics of the traveling wave generator: Variation of the rotation speed Ω for $R_i = 7\,\mathrm{k\Omega}$.

of the wobbling disk generator. As investigated analytically and numerically (section 4.2.1 and 4.2.2), the mode number whit the lowest minimum rotation speed for self-excitation, is non-trivial (here $(12, 0)$-mode with the wave number $\kappa^* = 12$). By varying the rotation speed, a jump phenomenon between the modes can be observed. The jump direction is denoted in Fig. 6.8 by arrows. The behavior for a sweep up of the rotation speed can be described as a jump down, since subsequently the next lower mode becomes active. Analogously, the behavior for a sweep down of the rotation speed can be described as a jump up, but here the jump occurs not necessarily to the next higher mode. The experiments showed that the characteristic rotation speed of a specific mode for which the jump down occurs, is lower than the rotation speed for which the mode becomes initiated. Regarding the voltage amplitude, shown in Fig. 6.8b, an equivalent jump phenomenon is observed. The characteristic behavior for a single mode is that the voltage increases linearly with the rotation speed, similarly to the wobbling disk characteristic. A further observation is that $\hat{v}_i$ of modes with wave number 9, 10 and 11 is significantly higher than for other modes. The reason for this is the electrode configuration of the ultrasonic motor, which is optimized for the motor operation in the $(10, 0)$-mode. A detailed discussion concerning different electrode configurations is given in

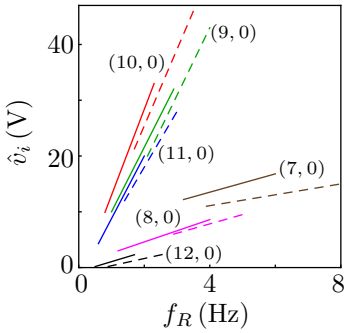

(a) Voltage amplitude $\hat{v}_i$, dashed lines: higher pre-stress.

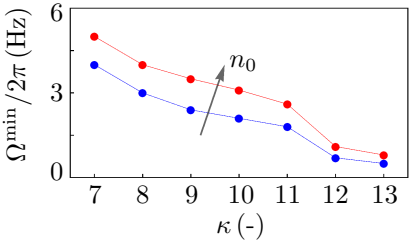

(b) Minimum rotation speed $\Omega^{\min}$ for different modes (wave number κ).

Figure 6.9: Transmission characteristics for a variation of the pre-stress n_0.

section 6.3.3.

Figure 6.9 shows the influence of the pre-stress on the transmission characteristics. As expected, the minimum rotation speed, needed for self-excitation, increases for higher pre-stress (Fig. 6.9b). The phenomenon that $\Omega^{\min}$ is lower for a higher mode, was already observed for the simplified model (Fig. 4.7) as well as for the finite element model (Fig. 4.9a). In the simplified models this characteristic mode is not estimated correctly. Nevertheless, this phenomenon is present in the simplified models allowing the analysis of the influence of the main parameters. The characteristic branches of the modes are shifted to larger rotation speeds, due to the higher pre-stress (Fig. 6.9a). The advantage is that each mode is stable up to a higher Ω leading consequently to a higher maximum amplitude $\hat{v}_i$.

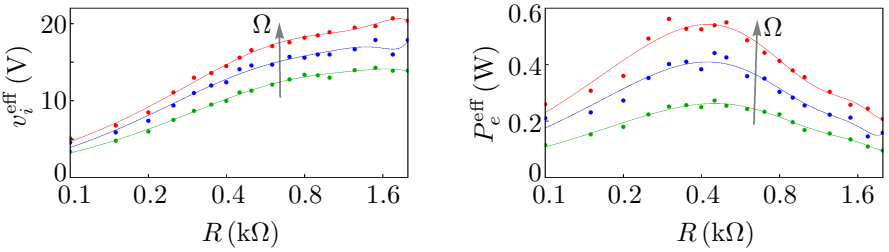

(a) Effective electric voltage.

(b) Effective electric power.

Figure 6.10: Electric voltage and power output of the traveling wave generator for the $(11, 0)$-mode (47.8 kHz): Variation of the rotation speed Ω.

Regarding the electric part of the generator, for each mode an optimum resistance can be found, maximizing the electric power output. To this end, the electric resistance R at the electrode outputs was varied in the experiments. The resulting transmission characteristics for the $(11, 0)$-mode is shown in Fig. 6.10. The other modes show qualitatively the same behavior: The electric voltage increases linearly with R and the electric power is maximum for a specific optimum resistance. This optimum resistance is unaffected by the rotation speed Ω and can be adjusted independently from excitation parameters. Through an increase of the rotation speed, the voltage as well as

the power characteristics are shifted to larger values, see Fig. 6.10. The optimum resistance of different modes is compared in Fig. 6.11a. It can be observed, the higher the natural frequency of the mode, the lower the optimum resistance. This is in agreement with the derived equation for the optimum resistance (4.94) based on the simplified model of the generator. According to this equation, the optimum resistances for the modes showed in Fig. 6.11a are: $R_7 = 1034\,\Omega$, $R_9 = 602\,\Omega$ and $R_{11} = 413\,\Omega$ (parameters used are given in Tab. 4.1). A comparison to the experimentally determined values ($R_7^* = 689\,\Omega$, $R_9^* = 523\,\Omega$, $R_{11}^* = 420\,\Omega$) shows that the optimum resistances are partially overestimated in the simplified model.

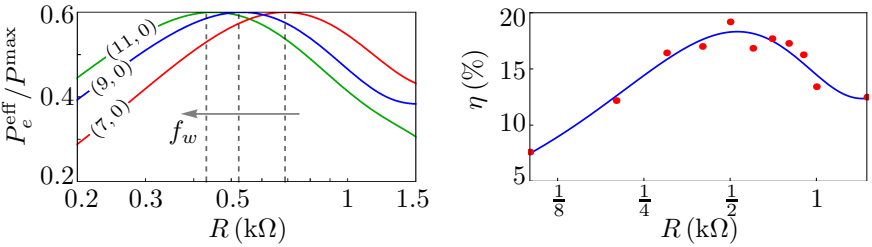

(a) Normed electric power output.

(b) Efficiency η: $(10, 0)$-mode.

Figure 6.11: Efficiency and optimal resistance of the traveling wave generator: characteristics for different modes.

In the experiments, the electric power harvested by the traveling wave generator was in the range up to 1 W (Fig. 6.10b), which is relatively high compared to common energy harvesting systems generating power in the range μW to mW, see [38, 40]. The high power output results from the high magnitude of the input power, which lies in a relatively high range (up to 10 W). Therefore, a more appropriate parameter characterizing the generator, namely the efficiency, is used. The efficiency of the generator is defined as

$$\eta := \frac{P_e^{\text{eff}}}{P_{\text{in}}} = \frac{\frac{1}{2}\sum_\zeta \hat{v}_\zeta^2 / R_\zeta}{\Omega\, M_R}, \tag{6.1}$$

where the output power P_e^{eff} corresponds to the sum of the effective electric power over the resistances R_ζ and the input power P_{in} is given through the

rotation speed and torque on the rotor. The efficiency of the $(10,0)$-mode[1] (40.2 kHz) is plotted in Fig. 6.11b. For the optimum resistance of about $R_{10}^{*} \approx 500\,\Omega$ an efficiency of $\eta = 19.3\,\%$ can be achieved. This efficiency value lies approximately in the range of the ultrasonic motor in motor operation measured by Sattel in [45]. Depending on the torque and the axial pre-load an efficiency of about 20-40 % was achieved.

6.3.2 Modal analysis

In addition to the experimental investigation of the steady-state behavior of the traveling wave generator, also an experimental modal analysis of the elastic stator was performed. The aim was to compare the measured operation mode frequencies to the natural frequencies of the stator. During the measurements, the rotor was disassembled and the vibrations of the stator were measured with a laser vibrometer. The resulting modal spectrum is shown in Fig. 6.12. Many discrete points on the circumference of the stator were

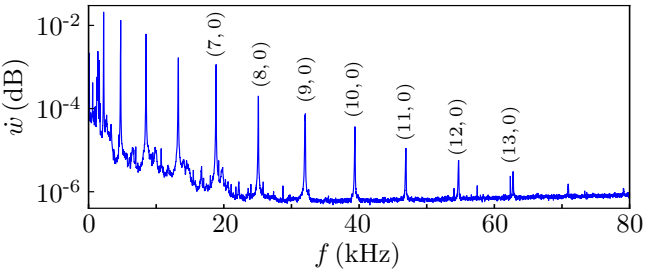

Figure 6.12: Modal spectrum of the elastic stator.

measured, in order to enable an identification of the mode shapes for each natural frequency. As expected, the spectrum is dominated by bending modes of the stator. Exemplarily, the mode shapes of the $(6,0)$-mode and $(8,0)$-mode are illustrated in Fig. 6.13. A further observation from the modal spectrum is that the peak of a single mode is relatively sharp, indicating a relatively small modal damping ratio for this mode. The natural frequencies obtained

[1] The electrode configuration was optimized for this mode, in which the ultrasonic motor was planned to be operated.

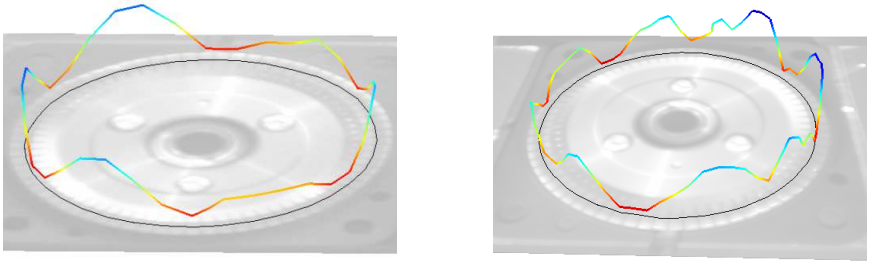

(a) $(6,0)$-mode shape. **(b)** $(8,0)$-mode shape.

Figure 6.13: Mode shapes of the elastic stator of the traveling wave generator.

Table 6.1: Comparison of the natural frequencies of the stator to the operation mode frequencies of the traveling wave generator ($*$ no data available).

mode	natural frequency (kHz)	operation mode (kHz)	deviation (%)
$(3,0)$	2.2	*	-
$(4,0)$	4.8	*	-
$(5,0)$	8.5	*	-
$(6,0)$	13.3	*	-
$(7,0)$	18.9	19.1	1.1
$(8,0)$	25.1	25.3	0.8
$(9,0)$	32.1	32.8	2.1
$(10,0)$	39.4	40.2	2.0
$(11,0)$	46.9	47.8	1.9
$(12,0)$	54.7	56.5	3.2
$(13,0)$	62.8	64.5	2.6
$(14,0)$	70.9	72.5	2.2
$(15,0)$	79.1	*	-

by the modal analysis are summarized together with the measured operation mode frequencies in Tab. 6.1. Despite of a small deviation, the operation

mode frequencies correspond very precisely to the natural frequencies. The explanation for the slightly higher frequencies during the operation is that in the assembled state, the rotor is pressed against the stator leading to a stiffening effect of the system. From this results two main advantages arise. The first one is that the operation mode frequencies are completely independent from the excitation frequency, so that broad-band applicability can be assured. The second one is that these frequencies can be set by designing the natural frequencies of the stator, in order to operate the piezoelectric element in the more efficient high frequency range.

6.3.3 Electrode configuration

Regarding the experimental investigations, an obvious approach is to analyze the convertibility using commonly available ultrasonic motors. However, this comes with the disadvantage that the voltage amplitude has a significant drop if the operation mode is not the mode the electrodes are optimized for, see Fig. 6.8b. Clearly, the highest amplitude can be observed for the $(10, 0)$-mode, for which the electrode configuration is designed for. For other modes cance-

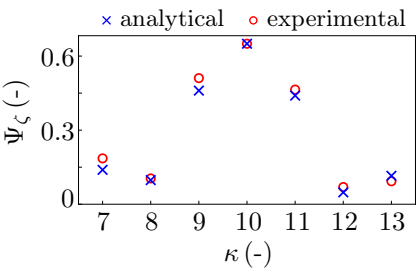

(a) Geometric coupling factor Ψ_ζ.

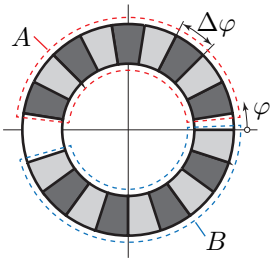

(b) Electrode configuration optimized for the $(10, 0)$-mode.

Figure 6.14: Electrode configuration of the traveling wave generator..

lations of the electric potential occur, leading to a significant efficiency drop. The electrode configuration of the used ultrasonic motor consists of two electrodes denoted as A and B, shown in Fig. 6.14b. The electrodes are divided into several segments, in order to excite the $(10, 0)$-mode in the motor ope-

ration. The angle of a single segment depends on the wave number of the mode to excite ($\Delta\varphi = \pi/\kappa$). According to the electrode configuration shown in Fig. 6.14b, the corresponding geometric coupling factors for each mode can be calculated based on Eq. (4.92). These coupling factors are plotted in Fig. 6.14a together with the experimentally determined factors, according to the voltage amplitudes in Fig. 6.8b. For all measured modes the calculated coupling factors match very precisely the experimental ones. In order to avoid drawbacks resulting from the misarrangement of the electrode, the solution for the operation as a generator is as follows: The architecture of the electrode segments can be kept, but it is necessary that each segment becomes electrically separated from the others, in order to obtain a set of decoupled electrical states. The calculated geometric coupling factor for such separated configuration (E^s_{10}) is displayed in Fig. 6.15a. The coupling factors for the unseparated

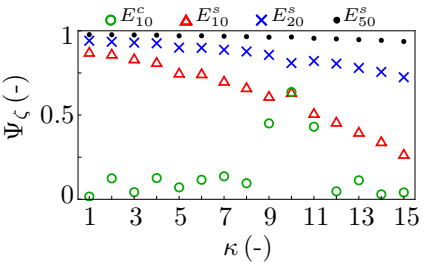

(a) Geometric coupling factor Ψ_ζ.

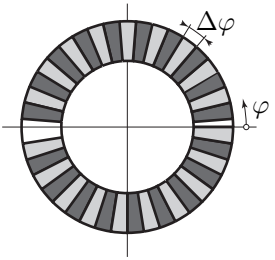

(b) Electrode configuration with $\Delta\varphi = \pi/20$.

Figure 6.15: Geometric coupling factors for different modes: Comparison of different coupled (superscript c) and separated (superscript s) electrode-segments configurations (subscript κ).

(coupled) case are denoted as E^c_{10}. Clearly, separating the segments leads to significantly larger coupling factors, since no cancelations occur. Reducing the size of the uni-potential segments leads to a further increase of the coupling factor, see configurations E^s_{20} ($\kappa = 20$) and E^s_{50} ($\kappa = 50$) in Fig. 6.15a. Exemplarily, the electrode configuration E^s_{20} is shown in Fig. 6.15b. Compared to the configuration in Fig. 6.14b the segments here have only half the size. The separation of the electrode segments as well as the increase of its number

leads to a large number of additional electric states. Consequently, the required electronics for the management of all these electric states becomes more complex. Therefore, the electrode configuration should be optimized considering on the one hand, the number of electric states, which is to be minimized and on the other hand, the coupling factor for the modes occurring during the operation, which is to be maximized. The number of the electric states depends on two parameters, namely the size of each electrode segment and the connection between these segments. Depending on the specific application and the design of the generator, different modes can be self-excited in the generator operation leading to different optimum electrode configuration.

7 Conclusion

In this work, mechanical systems exploiting self-excited friction-induced vibrations are proposed for kinetic energy harvesting applications. The considered systems transform vibrations from a low frequency source ($< 200\,\mathrm{Hz}$) to high frequency vibrations ($> 10\,\mathrm{kHz}$), in order to enhance the performance of piezoceramics used for the electromechanical energy conversion. An obvious approach was to use commonly available ultrasonic motors, which show a very high mechanical frequency transformation in motor operation, namely from high to low frequency. The main objective was to asses the feasibility of inverting the actuation of ultrasonic motors. To this end, analytically as well as experimental studies are carried out for two different types of ultrasonic motors, namely a wobbling disk and a traveling wave ultrasonic motor. Through the inversion of the actuation of ultrasonic motors two main challenges arise: The vibrations of the stator have to be initiated by means of self-excitation and the resulting limit-cycle oscillations have to the optimized regarding high efficiency performance.

Based on the simplified models, derived for the considered generators, conservative approximations are given for the region, where self-excited vibrations occur. These approximations indicate the design criteria for generators exploiting self-excited vibrations. It is shown that the mechanical properties of the frictional contact layer play an essential role in the initiation of self-excited vibrations. However, the analysis showed that the attachment of the frictional contact layer has a negligible effect on the dynamics of the system. For the wobbling disk generator the influence of the main parameters on the initiation of self-excited vibrations is verified numerically by finite element analysis as well as by experimental investigations. In addition, the influence of different forms of the excitation signal on the initiation of self-excited vibrations, is analyzed considering constant as well as periodic rotation speed of

the rotor. For excitation frequencies much lower than the natural frequency of the system, which lies in the kHz-range, the stability boundary is identical to the one obtained for a constant rotation speed. In case of the traveling wave generator, where different modes can be self-excited, it is shown analytically and numerically that a higher bending mode is initiated first. However, this specific mode is underestimated by the simplified models. This implies the necessity of a more detailed model, considering for example the contact teeth of the elastic stator.

The analyzed steady-state characteristics of the generators shows that the frequency of the operation mode is independent from the excitation frequency. This leads to a broad-band applicability of the generators, which is utmost important in order to assure high efficiency in a wide range of excitation frequencies. Moreover, the frequencies measured during the operation are identical to the natural frequencies of the system. This is confirmed on the one hand, by the derived simplified models and on the other hand, by experimental modal analysis of the stator. Consequently, the operation mode frequencies can be adjusted by designing the natural frequencies of the generator. Regarding the amplitude of the steady-state oscillation, the experiments as well as the analytical investigations show an almost linear dependence on the rotation speed. The electric power output measured at the electric loads was maximized by optimizing the corresponding electric resistance. Based on the simplified model, the optimal resistances are estimated as functions of the system parameters and the operation mode frequency. Since the operation mode frequency corresponds to the natural frequency of the system, for each mode the optimum resistance can be adjusted independently of any excitation parameter. While for the wobbling disk generator only one mode could be self-excited in the experiments, in case of the traveling wave generator, depending on the rotation speed, different modes are initiated. For an increasing rotation speed, subsequently the next lower mode become active. In order to determine, when a specific mode is active, it is necessary to analyze its basin of attraction. To this end, a method is proposed, which allows the estimation of basins of attraction for an autonomous system in an analytical way. This approach is successfully applied on different examples from the lite-

rature. However, the application on the steady-state motion of the traveling wave generator requires further development of this approach. In future work, the approach has to be extended on the estimation of basins of attraction for non-autonomous systems.

The electrode configuration of the traveling wave generator is designed for the motor operation in one specific mode. If in the generator operation another mode is active, cancellations of the electric potential occur, leading to a significant loss of efficiency. The solution proposed, is to separate the electrode segments, in order to avoid electric potential cancelations. A further increase of the efficiency can be achieved by reducing the size of each segment. However, also the number of additional electric states increases. Therefore, it is necessary to optimize the electrode configuration considering the number of the electrical states and the efficiency of the whole system. It is an objective of future work to manufacture and investigate in experiments different electrode configurations, in order to verify the analytical results.

For the studied generators different types of solutions are analyzed with respect to the stability behavior. Depending on the type of the linearized system, different analysis methods are required. Since no general theory exists for the stability analysis of time-variant systems, an analytical approach is developed, which allows the estimation of the stability boundary of non-autonomous systems. The so-called *embedding technique*, which embeds a non-autonomous ordinary equation of motion into an autonomous one of a much higher order, is successfully applied on well-known examples from the literature. Furthermore, the stability of the steady-state motion of the wobbling disk generator, which leads to the analysis of a non-periodic system, is analyzed by using the *embedding technique*. The results are confirmed by numerical simulation of the equations of motion.

The ultrasonic generators studied in this thesis operate in a frequency, which is independent of the excitation frequency and are therefore suitable for a broad-band energy harvesting application. The experiments carried out agree with the analytically derived estimates for the dynamic behavior. Moreover, the experiments show that the energy conversion through the generators is reproducible and that an acceptable efficiency can be achieved.

Bibliography

[1] Abouhazim, N.; Rand, R.; Belhaq, M.: The Damped Nonlinear Quasi-periodic Mathieu Equation Near 2:2:1 Resonance, *Nonlinear Dynamics*, 45:237–247, 2006.

[2] Adamy, J.: *Nichtlineare Regelungen*, Springer-Verlag, Dordrecht, Heidelberg, London, New York, 2009.

[3] Banks, S.P.: Generalization of the Lyapunov equation to non-linear systems, *International Journal of Systems Science*, 19(4):629–636, 1988.

[4] Beeby, S.; White, N. (Editors): *Energy Harvesting for Autonomous Systems*, Artech House, 2010.

[5] Brommundt, E.: Ein Reibschwinger mit Selbsterregung ohne fallende Reibkennlinie, *ZAMM*, 75 (11):811–820, 1995.

[6] Brommundt, E.: A simple model for friction induced high-frequency self-excitation of paper calenders, *Machine Dynamics Problems*, 31:25–45, 2007.

[7] Carleman, T.: Application de la théories des équations intégrales linéaires aux systèmes d'équations différentielles non linéaires., *Acta. Math*, 59:63–87, 1932.

[8] Erturk, A.; Inman, D.J.: *Piezoelectric Energy Harvesting*, John Wiley & Sons, Ltd, 2011.

[9] Fidlin, A.: *Nonlinear Oscillations in Mechanical Engineering*, Springer-Verlag, Berlin, Heidelberg, 2006.

[10] Gu, L.; Livermore, C.: Impact-driven, frequency up-converting coupled vibration energy harvesting device for low frequency operation, *Smart Materials and Structures*, 20:045004, 2011.

[11] Gutschmidt, S.: *Mathematical-Mechanical Modeling of Wobbling Disk Ultrasonic Motors*, Dissertation, Technische Universität Darmstadt, 2005.

[12] Hagedorn, P.; Hochlenert, D.: *Technische Schwingungslehre. Schwingungen linearer diskreter mechanischer Systeme*, Wissenschaftlicher Verlag Harri Deutsch, Frankfurt am Main, 2012.

[13] Hagedorn, P.: *Non-Linear Oscillations*, Oxford University Press, New York, 1988.

[14] Hagedorn, P.: *Technische Schwingungslehre, Band 2, Lineare Schwingungen kontinuierlicher mechanischer Systeme*, Springer-Verlag, Berlin, Heidelberg, New York, London, Paris, Tokyo, 1989.

[15] Hagedorn, P.; DasGupta, A.: *Vibrations and Waves in Continuous Mechanical Systems*, John Wiley & Sons Ltd, England, 2007.

[16] Hamidi, F.; Abdelkrim, M.N.; Jerbi, H.: Searching Candidate Lyapunov Function with Threshold Accepting Algorithm, *Computational Intelligence, Communication Systems and Networks*, pp. 26–31, 2011.

[17] Heffel, E.; Hagedorn, P.: Liapunov Functions and Carleman Linearization, *83rd annual Meeting of the GAMM, Darmstadt, Germany, 26th - 30th March*, 2012.

[18] Heffel, E.; Spelsberg-Korspeter, G.: Analysis of technical systems using Carleman linearization, *International Conference on Structural Nonlinear Dynamics and Diagnosis, Marrakech, Morocco, 30th April - 2nd May*, 2012.

[19] Hochlenert, D.: *Normalformen und Einzugsbereiche nichtlinearer dynamischer Systeme. Beispiele und technische Anwendungen.*, Habilitationsschrift, Technische Universität Berlin, 2012.

[20] Hochlenert, D.; Spelsberg-Korspeter, G.; Hagedorn, P.: Friction Induced Vibrations in Moving Continua and Their Application to Brake Squeal, *Journal of Applied Mechanics*, 74(3):542–549, 2006.

[21] Hoffmann, N.; Fischer, M.; Allgaier, R.; Gaul, L.: A Minimal Model for Studying properties of the Mode-Coupling Type Instability in Friction Induced Oscillations, *Mechanics Research Communications*, 29:197–205, 2002.

[22] Ikeda, T.: *Fundamentals of Piezoelectricity*, Oxford University Press, Oxford, New York, Tokyo, 1990.

[23] Irretier, H.: *Grundlagen der Schwingungstechnik 2*, Friedr. Vieweg & Sohn Verlagsgesellschaft mbH, Braunschweig, Wiesbaden, 2001.

[24] Kane, T.R.; Levinson, D.A.: *Dynamics: Theory and Applications*, McGraw-Hill, New York, 1985.

[25] Kazmierski, T.J.; Beeby, S. (Editors): *Energy Harvesting Systems, Principles, Modeling and Applications*, Springer, New York, Dordrecht, Heidelberg, London, 2011.

[26] Kim, H.S.; Kim, J.H.; Kim, J.: A Review of Piezoelectric Energy Harvesting Based on Vibration, *International Journal of Precision Engineering and Manufacturing*, 12(6):1129–1141, 2011.

[27] Kinkaid, N.; O'Reilly, O.; Papadopoulos, P.: Automotive disc brake squeal, *Journal of Sound and Vibration*, 267:105–166, 2003.

[28] Kowalski, K.; Steeb, W.H.: *Nonlinear Dynamical Systems and Carleman Linearization*, World Scientific Publishing Co. Pte. Ltd., Singapore, New Jersey, London, Hong Kong, 1991.

[29] Ludyk, G.: *Theoretische Regelungstechnik 1: Grundlagen, Synthese linearer Regelungssysteme*, Springer-Verlag, Berlin Heidelberg New York, 1995.

[30] Lunze, J.: *Regelungstechnik 1: Systemtheoretische Grundlagen, Analyse und Entwurf einschleifiger Regelungen*, Springer-Verlag, Berlin Heidelberg, 2006.

[31] Marinkovic, D.; Koppe, H.; Gabbert, U.: Accurate Modeling of the Electric Field within Piezoelectric Layers for Active Composite Structures, *Journal of Intelligent Material Systems and Structures*, 18:503–513, 2007.

[32] Matsumoto, N.: Simple Proof of the Routh Stability Criterion Based on Order Reduction of Polynomials and Principle of Argument, *Proceedings, IEEE, International Symposium on Circuits and Systems*, 1:699–702, 2001.

[33] Standards Committee of the IEEE Ultrasonics, Ferroelectrics, and Frequency Control Society: IEEE Standard on Piezoelectricity, *IEEE, New York*, 1987.

[34] Nayfeh, A.H.: *Perturbations Methods*, John Wiley & Sons, Ltd., 1973.

[35] Nayfeh, A.H.; Mook, D.T.: *Nonlinear Oscillations*, WILEY-VCH Verlag GmbH & Co. KGaA, 1995.

[36] Nguyen, H.T.: *Nonlinear Quasi-static and Dynamic Behavior of Piezoceramics at Moderate Strains*, Dissertation, Technische Universität Berlin, 2011.

[37] Parks, P.; Hahn, V.: *Stability Theory*, Prentice Hall, 1992.

[38] Penella-López, M.T.; Gasulla-Forner, M.: *Powering Autonomous Sensors, An Integral Approach with Focus on Solar and RF Energy Harvesting*, Springer, Dordrecht, Heidelberg, London, New York, 2011.

[39] Priya, S.: Modeling of Electric Energy Harvesting Using Piezoelectric Windmill, *Applied Physics Letters*, 87:184101, 2005.

[40] Priya, S.; Inman, D.J.: *Energy Harvesting Technologies*, Springer Science+Business Media, LLC, 2009.

[41] Rand, R.; Guennoun, K.; Belhaq, M.: 2:2:1 Resonance in the Quasiperiodic Mathieu Equation, *Nonlinear Dynamics*, 31:367–374, 2003.

[42] Rand, R.; Morrison, T.: 2:1:1 Resonance in the Quasi-Periodic Mathieu Equation, *Nonlinear Dynamics*, 40:195–203, 2005.

[43] Rao, S.S.: *Vibration of Continous Systems*, John Wiley & Sons, Inc., Hoboken, New Jersey, 2007.

[44] Roundy, S.; Wright, P.; Rabaey, J.: A study of low level vibrations as a power source for wireless sensor nodes, *Computer Communications*, 26:1131–1144, 2003.

[45] Sattel, T.: *Dynamics of Ultrasonic Motors*, Dissertation, Technische Universität Darmstadt, 2002.

[46] Sattel, T.; Hagedorn, P.; Schmidt, J.: The Contact Problem in Ultrasonic Traveling-Wave Motors, *Journal of Applied Mechanics*, 77(3):031014, 2010.

[47] Schmidt, J.: *Ein mechanisches Modell des Stator-Rotor-Kontaktes beim Ultraschall-Wanderwellenmotor*, Dissertation, Technische Universität Darmstadt, 2000.

[48] Schönecker, M.: *Traveling Wave Ultrasonic Motors Based on the Piezoelectric Shear Effect*, Dissertation, Technische Universität Darmstadt, 2009.

[49] Spelsberg-Korspeter, G.: Structural optimization for the avoidance of self-excited vibrations based on analytical models, *Journal of Sound and Vibration*, 329:4829–4840, 2010.

[50] Spelsberg-Korspeter, G.: Eigenvalue optimization against brake squeal: Symmetry, mathematical background and experiments, *Journal of Sound and Vibration*, 331(19):4259–4268, 2012.

[51] Spelsberg-Korspeter, G.: *Robust Structural Design against Self-Excited Vibrations*, Springer Netherlands, 2013.

[52] Spelsberg-Korspeter, G.; Hagedorn, P.: Complex Eigenvalue Analysis and Brake Squeal: Traps, Shortcomings and their Removal, *SAE Int. J. Passeng. Cars - Mech. Syst.*, 5(4):1211–1216, 2012.

[53] Spelsberg-Korspeter, G.; Hochlenert, D.; Hagedorn, P.: Self-excitation mechanisms in paper calenders formulated as a stability problem, *Technische Mechanik*, 31(1):15–24, 2011.

[54] Spelsberg-Korspeter, G.; Hochlenert, D.; Heffel, E.; Wagner, A.; Hagedorn, P.; Sampaio, R.: Construction of Lyapunov functions for the estimation of basins of attraction, *Journal of the Brazilian Society of Mechanical Sciences and Engineering*, 34(2):633–639, 2012.

[55] Tang, L.; Yang, Y.; Soh, C.K.: Toward Broadband Vibration-based Energy Harvesting, *Journal of Intelligent Material Systems and Structures*, 21:1867, 2010.

[56] Unbehauen, H.: *Regelungstechnik I: Klassische Verfahren zur Analyse und Synthese linearer kontinuierlicher Regelsysteme, Fuzzy-Regelsysteme*, Vieweg Teubner Verlag, Wiesbaden, 2008.

[57] Vannelli, A.; Vidyasagar, M.: Maximal Lyapunov Functions and Domains of Attraction for Autonomous Nonlinear Systems, *Automatica*, 21(1):69–80, 1985.

[58] Verhulst, F.: *Nonlinear Differential Equations and Dynamical Systems*, Springer-Verlag, Berlin, Heidelberg, 1996.

[59] von Wagner, U.: *Nichtlineare Effekte bei Piezokeramiken unter schwachem elektrischem Feld: Experimentelle Untersuchung und Modellbildung*, Habilitationsschrift, Technische Universität Darmstadt, 2003.

[60] von Wagner, U.; Hochlenert, D.; Hagedorn, P.: Minimal models for disk brake squeal, *Journal of Sound and Vibration*, 302:527–539, 2007.

[61] Wagner, A.: *Avoidance of brake squeal by a separation of the brake disc's eigenfrequencies: A structural optimization problem*, Dissertation, Technische Universität Darmstadt, 2013.

[62] Wiendl, S.: *Modellierung von Schwingungsphänomenen in Papierkalandern*, Dissertation, Technische Universität Darmstadt, 2011.

[63] Wittenburg, J.: *Dynamics of Multibody Systems*, Springer, Berlin, Heidelberg, New York, 2008.

[64] Wolf, K.D.: *Electromechanical Energy Conversion in Asymmetric Piezoelectric Bending Actuators*, Dissertation, Technische Universität Darmstadt, 2000.

[65] Zubov, V.: *Methods of A.M. Lyapunov and their applications*, Nordhoff, Groningen, 1964.

Bisher sind in dieser Reihe erschienen

Band 1
Zur mikrorissinduzierten Schädigung spröder Materialien
B. Lauterbach, Dissertation 2001, ISBN 3-935868-01-4

Band 2
3D-Simulation der Mikrostrukturentwicklung in Zwei-Phasen-Materialien
R. Müller, Dissertation 2001, ISBN 3-935868-02-2

Band 3
Zur numerischen Simulation von Morphologieänderungen in mikroheterogenen Materialien
S. Kolling, Dissertation 2001, ISBN 3-935868-03-0

Band 4
Theoretische und numerische Untersuchung von Versagensmechanismen in Metall-Keramik-Verbundwerkstoffen
T. Emmel, Dissertation 2002, ISBN 3-935868-04-9

Band 5
On microcrack dominated problems in dynamics and statics of brittle fracture: a numerical study by boundary element techniques
S. Rafiee, Dissertation 2002, ISBN 3-935868-05-7

Band 6
Kontinuumsmechanik anisotroper Festkörper und Fluide
H. Ehrentraut, Habilitationsschrift 2002, ISBN 3-935868-06-5

Band 7
Plane unsteady inviscid incompressible hydrodynamics of a thin elastic profile
N. Blinkova, Dissertation 2002, ISBN 3-935868-07-3

Band 8
Anmerkungen zur Simulation von entfestigendem Materialverhalten
H. Baaser, Habilitationsschrift 2004, ISBN 3-935868-08-1

Band 9
Orts- und zeitadaptive DAE-Methoden zur Beschreibung elastisch-plastischen Materialverhaltens innerhalb der FEM
S. Eckert, Dissertation 2005, ISBN 3-935868-09-X

Band 10
Simulations of the Flow of the Ross Ice Shelf, Antarctica: Parameter Sensitivity Tests and Temperature-Dependent Rate Factor
A. Humbert, Dissertation 2005, ISBN 3-935868-10-3

Band 11
A Thermo-mechanical Continuum Theory with Internal Length of Cohesionless Granular Materials
Chung Fang, Dissertation 2006, ISBN 3-935868-11-1

Band 12
Modeling Dry Granular Avalanches past Different Obstructions: Numerical Simulation and Laboratory Analyses
Chiou Min-Ching, Dissertation 2006, ISBN 3-935868-12-X

Band 13
Configurational forces in defect mechanics and in computational methods
R. Müller, Habilitationsschrift 2005, ISBN 3-935868-13-8

Band 14
Hyperelastic dynamics in physical and material space
S. Kolling, Habilitationsschrift 2007, ISBN 978-3-935868-14-3

Band 15
Phenomenological modeling of ferroelectric material behavior
V. Mehling, Dissertation 2007, ISBN 978-3-935868-15-0

Band 16
Ein mischungsbasiertes Materialmodell zum Knochenumbau
R.-R. Kühn, Dissertation 2006, ISBN 978-3-935868-16-7

Band 17
Einige Erweiterungen der Rand-Finite-Elemente-Methode und deren Anwendung auf Randeffekte in ebenen Laminaten
J. Artel, Dissertation 2007, ISBN 978-3-935868-17-4

Band 18
Spannungskonzentrations-Effekte an Verstärkungspflaster-Ecken
H. Wigger, Dissertation 2008, ISBN 978-3-935868-18-1

Band 19
Rotationseffekte in der Kristallplastizität
C. Bröse, Dissertation 2007, ISBN 978-3-935868-19-8

Band 20
Finite-Element-Modelle zur Simulation von Delaminationen dünner Filme auf Substraten
V. D. Pham, Dissertation 2010, ISBN 978-3-935868-20-4

Band 21
Asymptotische Nahfeldanalysen ebener Multi-Materialverbindungsstellen mit der Methode komplexer Potentiale
C. Sator, Dissertation 2010, ISBN 978-3-935868-21-1

Band 22
Modellierung spröder Rissbildung an Spannungskonzentrationen mit der Bruchmechanik finiter Risse
J. Hebel, Dissertation 2010, ISBN 978-3-935868-22-8

Band 23
Some Contributions to the Homogenization of Macroscopically Isotropic Composites
V. Salit, Dissertation 2011, ISBN 978-3-935868-23-5

Band 24
Asymptotic Analysis of the Load Transfer on Double-Lap Bolted Joints
J. Kratochvíl, Dissertation 2012, ISBN 978-3-935868-24-2

Band 25
Spannungssingularitätsordnungen in linear-elastischen und piezoelektrischen Multimaterialkonfigurationen mit der Rand-Finite-Elemente-Methode
W. Mayland, Dissertation 2012, ISBN 978-3-935868-25-9

Band 26
Plastizität und Skaleneffekte sowie Deformations- und Versagensmodellierung dünner metallischer Schichten bei Nanoindentation
A. Trondl, Dissertation 2012, ISBN 978-3-935868-26-6

Band 27
Theoretical modeling and parallel programming of a nonlinear composite finite shell element based on a mixed global-local variational principle
M. Schürg, Dissertation 2012, ISBN 978-3-935868-27-3

Band 28
Strukturmechanische Modellierung und Analyse des Tragverhaltens von dünnwandigen hochbelasteten Composite-Biege- und Querkraftträgern
A. M. Kroker, Dissertation 2012, ISBN 978-3-935868-28-0

Band 29
Über die Entstehung von Raum und Zeit
P. Altstadt, Forschungsbereicht 2013, ISBN 978-3-935868-29-7

Band 30
Der Laminatrandeffekt und seine Analyse, insbesondere mit der Rand-Finite-Elemente-Methode
J. Lindemann, Dissertation 2013, ISBN 978-3-935868-30-3

Band 31
Avoidance of brake squeal by a separation of the brake disc's eigenfrequencies: A structural optimization problem
A. Wagner, Dissertation 2013, ISBN 978-3-935868-31-0

The main objective in the field of vibration-based energy harvesting is to convert the kinetic energy from an ambient energy source into an useable electrical form in the most efficient way. The intention is to provide power for low-powered electronic devices, such as intelligent sensors for structural health monitoring, in order to make an external power source or periodic battery replacement redundant and thus lower the costs. One of the main challenges in the area of vibration-based energy harvesting is to design an energy harvesting device generating a significant amount of electrical power across varying vibration inputs. In this thesis, a new concept of piezoelectric generators is studied in detail with respect to its applicability for energy harvesting systems. To this end, electromechanical models of two different ultrasonic motors are derived in order to study their convertibility of the operating direction. Based on the analytical models, the influence of the main parameters on the dynamic behavior as well as the characteristic steady-state operation are determined. Experiments are carried out to validate this concept.

ISBN 978-3-935868-32-7